Title
Analytical and Numerical Techniques in Static and Driven Topological Matter

Author
Reiss, Dominic Seth

Publication Date
2020

Peer reviewed|Thesis/dissertation

UNIVERSITY OF CALIFORNIA

Los Angeles

Analytical and Numerical Techniques in Static and Driven Topological Matter

A dissertation submitted in partial satisfaction

of the requirements for the degree

Doctor of Philosophy in Physics

by

Dominic Seth Reiss

2020

ABSTRACT OF THE DISSERTATION

Analytical and Numerical Techniques in Static and Driven Topological Matter

by

Dominic Seth Reiss
Doctor of Philosophy in Physics
University of California, Los Angeles, 2020
Professor Rahul Roy, Chair

This dissertation comprises two parts, each of which details an investigation within topological matter.

In the first part, we investigate the real space localization properties of static topological insulators in two dimensions. We develop three numerical procedures each of which removes an extensive fraction of the local degrees of freedom. We probe the real space properties of the residual projection operator, showing that the maximally localized length scale ξ supported in the residual Hilbert space diverges as the fraction of states remaining approaches 0. The power-law exponent $\nu \simeq 1/2$ characterizing the singular behavior of ξ appears universal across class A insulators with non-zero Chern number.

In the second part, we explore a class of Floquet topological phases in three dimensions. These phases have translational invariance but no other symmetry, and exhibit anomalous transport at a boundary surface. We show that the boundary behavior of such phases falls into equivalence classes up to local 2D unitary evolution. This provides a classification of the 3D bulk, which we conjecture to be complete. We demonstrate that such phases may be generated by exactly solvable "exchange drives" in the bulk. The edge behavior of a general exchange drive in two or three dimensions is shown to derive from the geometric properties of its action in the bulk, a form of bulk-boundary correspondence.

The dissertation of Dominic Seth Reiss is approved.

Stuart Brown

Robijn Bruinsma

Michael Gutperle

Rahul Roy, Committee Chair

University of California, Los Angeles

2020

To my mother and father who cultivated my interest in mathematical problem solving.

TABLE OF CONTENTS

LIST OF FIGURES

LIST OF TABLES

ACKNOWLEDGMENTS

Many thanks to Rahul Roy, my research mentor and committee chair, through whom my approach to research has become more concise, precise, and inspired. During my doctoral studies at UCLA, Rahul taught me that research is mostly about asking the right questions; after the inquiry has been refined, the solution may simply reveal itself.

I owe much thanks to our former post-doctoral scholar Fenner Harper. Fenner spent many hours helping me understand smaller details within our specialization of topological condensed matter physics. Fenner also spent many hours working through my notes and drafts with me. He helped me develop a style of scientific writing which is both mathematically precise and easy to read.

I extend my gratitude to those (current and former) fellow students within our research group: David Bauer, Albert Brown, Xu Liu, Pratik Sathe, and Spenser Talkington. They all have been great friends and always welcomed my inquiries or requests for discussion.

I am indebted to my partner Jun Gao has been a pillar of support for the past six years. Whenever my spirit had faded, Jun has been there to talk through my problems and help me decompress. Without her unwavering encouragement, I would surely have enjoyed this experience much less.

I express appreciation to my committee for donating their time and guidance to the review of this document and its defense.

The research appearing in this thesis was performed collaboratively with Fenner Harper and Rahul Roy. Portions of this thesis are adapted near verbatim from published material co-authored by Fenner Harper and Rahul Roy with their permission.

VITA

2013	BSc. (Physics with Theoretical Physics), Imperial College London
2014	MASt. (Applied Mathematics and Theoretical Physics), University of Cambridge
2014–present	Teaching Assistant, Department of Physics and Astronomy, University of California, Los Angeles

PUBLICATIONS AND PRESENTATIONS

Reiss, D., Harper, F., and Roy, R. *Topological edge and dislocation modes in 3D Floquet systems.* APS March Meeting, New Orleans (2017).

Reiss, D. and Roy, R. *Edge invariant for 3D interacting Floquet systems with translation symmetry.* APS March Meeting, Los Angeles (2018).

Reiss, D., Harper, F., and Roy, R. *Interacting Floquet topological phases in three dimensions.* Physical Review B **98**, 045127 (2018).

Reiss, D., Harper, F., and Roy, R. *Numerical localization signatures of topology in two dimensional insulators.* (In preparation, 2020).

CHAPTER 1

Introduction

In this chapter we provide a broad overview of several aspects of topological matter, a field which has received a considerable amount of recent attention. We do not attempt to review each of these aspects in depth, but rather provide those details which are important to later chapters of the thesis and touch on others to offer context. Within each section we point the reader to technical and pedagogical references to give more depth if desired.

This thesis comprises investigations within two distinct subfields: the first subfield involves static (or time-independent) systems, while the second subfield involves Floquet (or time-periodic) systems. Although static topological systems may technically be viewed a subset of Floquet systems, their study predates Floquet systems by several decades. The perspective, techniques, and goals appearing in much of the literature differ quite significantly between these fields, so we therefore elect to keep the discussion of static and Floquet systems largely separate.

1.1 Static topological phases

The study of topological matter within the last 50 years has developed into one of the most active and exciting fields within condensed matter physics. Occupying an interesting space within physics, the study of topological matter has continuously introduced novel mathematical techniques while remaining experimentally accessible. The range of novel phenomena encountered is not only surprising, but also promises useful to future applications. Here we briefly introduce static topological systems, beginning with the prototypical example of the integer quantum Hall effect, before revisiting them in Chapters 2 and 3.

1.1.1 Landau levels in the integer quantum Hall effect

The integer quantum Hall effect, whose discovery is often attributed to von Klitzing in 1980 [1] for which he was awarded the Nobel prize in 1985, is a term used to describe the quantization of the Hall conductance σ_H in some effectively 2D materials (most often semiconductor heterostructures) when a large perpendicular magnetic field is applied. That is, in terms of fundamental constants

$$\sigma_H = \nu \frac{e^2}{h},$$

where e is the fundamental electric charge, h is Plank's constant, and the filling factor ν is an integer. These remarkable observations sparked investigation providing insight into the interplay between the space of electron wave functions and the magnetic field. Eventually this field broadened into the study of topological phases. We give a brief overview of aspects of the theory of the integer quantum Hall effect which is used in this thesis. As more extensive references we refer the reader to the books by Prange and Girvin [2] and more recently by Yoshioka [3], and the excellent lecture notes by Tong [4].

This effect, while unexpected, can be explained in a noninteracting setting. In this section, we describe aspects of the algebraic and real-space structure of the Hilbert space in the IQHE, collectively known as Landau levels. In Section 1.1.2 we will briefly outline the topological nature of this noninteracting model. We follow with a combination of the treatments in References 3 and 4.

We consider a 2D free electron in a perpendicular magnetic field B. It is sufficient to analyze the orbital part of the noninteracting Hamiltonian given by

$$H = \frac{1}{2m_e}(\mathbf{p} - e\mathbf{A})^2, \tag{1.1}$$

where m_e is the mass of the electron, e is the electron's charge, $\mathbf{p}$ is the linear momentum operator, and $\mathbf{A}$ is the vector potential. The vector potential exhibits the gauge symmetry generated by adding gradients of smooth real scalar functions χ, that is the transformation

$$\mathbf{A}'(\mathbf{r}) = \mathbf{A}(\mathbf{r}) + \nabla\chi(\mathbf{r})$$

leaves the magnetic field and any observable associated with the theory invariant. The underlying magnetic field is constant and therefore manifestly translationally and rotationally symmetric, however due to the gauge freedom $\mathbf{A}$ need not possess the same symmetry.

There are two commonly adopted gauge choices when working in the IQHE: the Landau gauge and the symmetric gauge. The Landau gauge is the choice

$$\mathbf{A} = xB\hat{\mathbf{y}}$$

which enjoys translation symmetry in the y direction (however breaks translation symmetry in the x direction and rotational symmetry) and is often used in calculations involving systems of strip geometry. The symmetric gauge is the choice

$$\mathbf{A} = -\frac{yB}{2}\hat{\mathbf{x}} + \frac{xB}{2}\hat{\mathbf{y}}$$

which breaks translation symmetry in both directions, but retains the rotational symmetry. The symmetric gauge is often used in calculations involving systems of infinite planar geometry, and will be the gauge we adopt throughout this thesis (unless otherwise stated). One of the benefits of choosing this gauge is that angular momentum is a good quantum number.

We introduce the dynamical momentum operator $\boldsymbol{\pi} = (\mathbf{p} - e\mathbf{A})$ whose components follow the scaled cannonical commutation relation

$$[\pi_x, \pi_y] = -i\frac{\hbar^2}{l^2}, \tag{1.2}$$

where $l = \sqrt{\hbar/|e|B}$ is an emergent length scale often referred to as the magnetic length. Rewriting Equation (1.1) using the components of dynamical momentum results in

$$H = \frac{1}{2m_e}\left(\pi_x^2 + \pi_y^2\right). \tag{1.3}$$

This simple quadratic form of the Hamiltonian combined with the fact that π_x and π_y are canonically conjugate operators (from Equation (1.2)) suggests the system shares its algebraic structure with the one dimensional quantum harmonic oscillator. Indeed defining

ladder operators

$$a = \frac{l}{\sqrt{2}\hbar}(\pi_x - i\pi_y),$$
$$a^\dagger = \frac{l}{\sqrt{2}\hbar}(\pi_x + i\pi_y),$$

which satisfy $[a\ , a^\dagger] = 1$, allows us to rewrite Equation (1.3) in the form

$$H = \hbar\omega_c \left(a^\dagger a\ + \frac{1}{2}\right), \tag{1.4}$$

where $\omega_c = |e|B/m_e$ is the cyclotron frequency. It is now obvious (for example by comparison with the harmonic oscillator) that the eigenvalues of H are partitioned into discrete levels

$$E_n = \hbar\omega_c \left(n + \frac{1}{2}\right), \tag{1.5}$$

for non-negative integers n. The states associated with each n are said to belong to a *Landau level*, with $n = 0$ commonly refered to as the lowest Landau level or LLL. Unlike the harmonic oscillator where each energy level hosts a single state, each Landau level hosts an extensively degenerate set of states. To see this, define the *center coordinate* operators

$$X = x - \frac{l^2}{\hbar}\pi_y,$$
$$Y = y + \frac{l^2}{\hbar}\pi_x,$$

which respect the canonical commutation relation $[X, Y] = il^2$ and which may be shown to commute with the Hamiltonian and cause each energy level to be degenerate. As mentioned earlier when working in the symmetric gauge the angular momentum commutes with the Hamiltonian. Its eigenvalues are therefore good quantum numbers. The angular momentum operator can be written as

$$L_z = -\frac{\hbar}{2l^2}(X^2 + Y^2) + \frac{l^2}{2\hbar}(\pi_x^2 + \pi_y^2). \tag{1.6}$$

Note that the second half of Equation 1.6 is proportional to the Hamiltonian, and the first half again has the algebraic structure of a harmonic oscillator. We further introduce another pair of ladder operators

$$b = \frac{1}{\sqrt{2}l}(X + iY),$$
$$b^\dagger = \frac{1}{\sqrt{2}l}(X - iY),$$

which again satisfy $[b\ , b^\dagger] = 1$. This allows us to rewrite the angular momentum in Equation (1.1) as

$$L_z = \hbar \left(a^\dagger a \ - b^\dagger b \ \right). \tag{1.7}$$

We can now enumerate an orthogonal basis of eigenstates for the Hamiltonian of Equation (1.4). The states $\{|n, m\rangle\}$ are uniquely labeled by two positive integers ($n \geq 0$, $m \geq 0$), which are the eigenvalues of the number operators $a^\dagger a$ and $b^\dagger b$ respectively, that is

$$a^\dagger a \ |n, m\rangle = n \, |n, m\rangle \, ,$$
$$b^\dagger b \ |n, m\rangle = m \, |n, m\rangle \, .$$

In this way each Landau level can be enumerated by fixing n and allowing m to vary.

By expressing the ladder operators in terms of the original Cartesian coordinate operators x and y and the momenta $-i\partial_x$ and $-i\partial_y$, one can determine the following plane polar coordinate representations of the functions

$$\langle \mathbf{r}|n, m\rangle = C_{n,m} \exp\left(i(n-m)\theta - \frac{r^2}{4l^2} \right) \left(\frac{r}{l} \right)^{|m-n|} L^{|m-n|}_{(n+m-|m-n|)/2} \left(\frac{r^2}{2l^2} \right), \tag{1.8}$$

where $C_{n,m}$ are the appropriate normalization constants and $L^i_j(x)$ are the associated Laguerre polynomials.

In this thesis we will often restrict our view to the space spanned by a single Landau level, often the LLL (where n = 0). We adopt the convention for complex coordinates $z = (x - iy)/l$ (following Reference 3). Within the LLL the functional form of the eigenstates in Equation (1.8) reduces to

$$\langle \mathbf{r}|0, m\rangle = \frac{1}{\sqrt{2\pi 2^m m! l}} z^m \exp\left(-\frac{|z|^2}{4} \right). \tag{1.9}$$

These functions are spatially concentrated on an annulus centered on the origin of radius $\sqrt{2ml}$ and exponentially decay away from this annular region. The angular momentum eigenstates are also eigenstates of the $\mathbf{r}^2$ operator

$$\mathbf{r}^2 \, |0, m\rangle = \sqrt{2(m+1)l^2} \, |0, m\rangle \, . \tag{1.10}$$

In Chapter 3 we perform numerical calculations in the LLL using the above basis of angular momentum states $\{|0,m\rangle\}$. We choose to work on a finite circular disc centered about the origin of radius R. We note that although the above algebraic structure and therefore the wavefunctions in Equations (1.8) and (1.9) are no longer exact, they are sufficient for numerical analysis if restricted to the appropriate region. In particular, on a circular disc of radius R we should only consider the finite basis spanned by states $\{|0,m\rangle\}$ where $2ml^2 \leq R^2$ [3].

We also note that due to the perpendicular magnetic field the coordinate momentum operator is no longer the generator of translations. The dynamical momentum $\boldsymbol{\pi}$ also does not generate translations in the symmetric gauge as it is not translation invariant. In fact the momentum $\mathbf{K}$, often refered to as the *pseudomomentum*, which generates translation is

$$\mathbf{K} = \boldsymbol{\pi} + e\mathbf{B} \times \mathbf{r}, \tag{1.11}$$

and the corresponding translation operator $t(\mathbf{d})$ corresponding to a displacement $\mathbf{d}$ is given by

$$t(\mathbf{d}) = \exp\left(-i\frac{\mathbf{d}\cdot\mathbf{K}}{\hbar}\right). \tag{1.12}$$

Importantly the translation operators in the IQHE do not commute, but rather

$$t(\mathbf{a})t(\mathbf{b}) = t(\mathbf{b})t(\mathbf{a})\exp\left(-i\frac{(\mathbf{a}\times\mathbf{b})_z}{l^2}\right), \tag{1.13}$$

indicative of the Aharonov-Bohm phase acquired by electronic states when translated [3].

1.1.2 Hall conductance and topological invariants

In Section 1.1.1 we reviewed essential algebraic aspects of the Landau level Hilbert space and the real space structure of the angular momentum basis. In this section we provide a superficial overview of some of the topological aspects of the IQHE. We defer the important discussion of disorder and other aspects of real space localization in the IQHE to Chapter 2.

The standard calculation resulting in the Hall conductance is a linear response calculation which results in the Kubo formula. We omit the mechanics of this linear response calculation

as it is not essential to this thesis. For a more detailed overview of linear response theory we refer the reader to the relevant chapters in the books by Chaikin and Lubensky [5] and Altland and Simons [6], as well as the lecture notes on kinetic theory by Tong [7].

After performing the linear response calculation with a perturbation ΔH due to an AC spatially-uniform electric field with frequency ω, the Kubo formula in the DC limit ($\omega \to 0$) gives the Hall conductance σ_H for the lowest Landau level as

$$\sigma_H = i\hbar A \sum_{n \neq 0} \frac{\langle \Psi_0 | J_y | \Psi_n \rangle \langle \Psi_n | J_x | \Psi_0 \rangle - \langle \Psi_0 | J_x | \Psi_n \rangle \langle \Psi_n | J_y | \Psi_0 \rangle}{(E_n - E_0)^2} \tag{1.14}$$

where A is the area of the occupied states, $|\Psi_n\rangle$ is the many-body state corresponding to the occupation of the n-th unperturbed Landau level by noninteracting particles, and $J_a = \frac{ie}{\hbar}[H, r_a]$ are the components of the current operator [4].

In Reference 8 Laughlin conducts a thought experiment which argues for the integer quantization of the Hall conductance, and makes the connection between the Kubo formula in Equation (1.14) and the underlying topological nature of the Hilbert space of an occupied Landau level. This argument is extended by Halperin to weakly disordered systems in Reference 9. We omit the details of this thought experiment, referring the reader to the pedagogical treatment of Reference 3 and the relevant sections of Reference 10. The essence of the argument begins by considering the Hall effect in a geometry with periodic boundary condition, and adiabaticly threading flux through the handles of this geometry while enforcing gauge equivalence of the wave function at the periodic boundaries. By establishing equivalence of the system with zero flux and after the threading of one flux quantum $\phi_0 = h/e$, one can establish the quantization of the Hall conductance.

Thouless, Kohmoto, Nightingale, and den Nijs (TKNN) provided a direct connection between the Hall conductance and a topological invariant for Hall type systems in a periodic potential in Reference 11. In particular they showed the Hall conductance could be computed from energy eigenstates (independent from the spectrum) $|\psi_{\mathbf{k}}\rangle$. The wavefunctions corresponding to a completely filled band of electrons define a geometric quantity $\boldsymbol{\mathcal{A}}$ known

as the Berry connection defined as

$$\boldsymbol{\mathcal{A}} = -i \left\langle \psi_{\mathbf{k}} \right| \nabla_{\mathbf{k}} \left| \psi_{\mathbf{k}} \right\rangle .$$

Since the wavefunctions $|\psi_{\mathbf{k}}\rangle$ exhibit gauge freedom corresponding to the smooth choice of their phase as a function of $\mathbf{k}$, the Berry connection is gauge dependent and transforms in the same way as the vector potential. The curvature associated with the Berry connection

$$\mathcal{F}_{xy} = (\nabla \times \boldsymbol{\mathcal{A}})_z = i \left(\left\langle \frac{\partial \psi_{\mathbf{k}}}{\partial k_x} \middle| \frac{\partial \psi_{\mathbf{k}}}{\partial k_y} \right\rangle - \left\langle \frac{\partial \psi_{\mathbf{k}}}{\partial k_y} \middle| \frac{\partial \psi_{\mathbf{k}}}{\partial k_x} \right\rangle \right) \tag{1.15}$$

is known as the Berry curvature and is gauge invariant. The TKNN invariant relates the Kubo formula for the Hall conductance in Equation 1.14 with the integral of the Berry curvature over the Brillouin zone, that is

$$\sigma_H = \frac{e^2}{h} \int \frac{\mathrm{d}^2 \mathbf{k}}{(2\pi)^2} \mathcal{F}_{xy} \tag{1.16}$$

where we have assumed the periodicity of the external potential is of unit length in both dimensions. This approach was further refined in References 12, 13, and 14.

The integral of the Berry curvature appearing on the right hand side of Equation (1.16) is known as the *first Chern number* C,

$$C = \int \frac{\mathrm{d}^2 \mathbf{k}}{(2\pi)^2} \mathcal{F}_{xy},$$

and is an integer for any connection $\mathcal{A}_i$ defined on the torus. The Berry connection $\mathcal{A}_i$ associated with any fully occupied Landau level has Chern number $C = 1$. Therefore if the first $\nu \in \mathbb{Z}$ bands are occupied the Hall conductance is

$$\sigma_H = \nu \frac{e^2}{h},$$

as expected. The expressions for the Berry curvature and the Chern number we reviewed above for single bands can be extended to the cases in which the electronic bands may cross or are degenerate.

In this context the first Chern number C is a topological invariant which distinguishes topologically distinct vector bundles on the torus $\mathbb{T}^2$. Although somewhat abstract, the

presence of a topological invariant has many physical consequences. Experimentally the most significant of these is that small perturbations to the Hamiltonian, that is perturbations which do not cause the spectral gap between the occupied and unoccupied states to collapse, do not change the value of the Hall conductance σ_H. In addition, 2D systems with Chern number enjoy a *bulk-boundary correspondence*: the Chern number calculated using Equation (1.16) of a spatially extended system with no boundary is equal to the number of propagating chiral edge modes at the boundary of a corresponding finite system [15].

1.1.3 Lattice models and Chern insulators

In Section 1.1.1 we described the Hilbert space structure of noninteracting electrons in two dimensions when a constant perpendicular magnetic field is applied. The IQHE and systems with similar properties can also be realized by noninteracting tight binding models on a lattice. Lattice models can be particularly useful for computational exploration; one can explore the phase space of various properties by tuning parameters of a single model. Additionally, as we will see in this section, toy models for novel phenomena are often easily presented in the tight binding formalism. We will assume the reader has familiarity with the formalism of tight binding lattice models.

1.1.3.1 Hofstadter model

We first briefly describe the direct lattice analog of the 2D free electrons subject to a perpendicular magnetic field and strong periodic potential, introduced by Hofstadter in Reference 16. For a single particle moving on a square lattice of unit spacing, the Hamiltonian is given as

$$H = -J \sum_{m,n} \left(e^{i\phi^x_{m,n}} c^\dagger_{m+1,n} c_{m,n} + e^{i\phi^y_{m,n}} c^\dagger_{m,n+1} c_{m,n} + h.c. \right)$$

where J is the nearest-neighbor coupling strength, and $\phi^a_{m,n}$ are the gauge-dependent Peierls phases acquired when an electron at lattice site (m, n) hops to its nearest neighbor in the r_a direction. For convenience, one often chooses the Landau gauge for the underlying vector

potential

The flux ϕ piercing each square plaquette varies with the strength of the magnetic field. The behavior of the spectrum of the Hofstadter model as one varies ϕ is quite surprising and results in the famous Hofstadter butterfly, depicted in Figure 1.1, which exhibits a fractal structure [16]. At rational flux ϕ the spectrum decomposes into gapped bands, each of which may independently have non-zero Chern number (computed using Equation (1.16)). Interestingly one finds that Chern numbers $|C| > 1$ may be found at various rational values of ϕ, which cannot be obtained by studying individual Landau levels in the continuum. On the other hand, at irrational values of ϕ, the spectrum takes the structure of a Cantor set. The range of novel phenomena exhibited by the Hofstadter model make it an attractive candidate for both numerical and analytic studies. For an in-depth pedagogical review of the Hofstatder model we refer the reader to the thesis by Harper [17].

1.1.3.2 Haldane honeycomb model

Besides the Hofstadter model there are many lattice models which host bands of non-zero Chern number, also called Chern insulators. In Reference 18 Haldane introduced such a two-band model which we will refer to as the Haldane honeycomb model. The Haldane honeycomb model is the first example of a non-trivial Chern insulator with zero net magnetic flux ϕ per plaquette. The presence of non-zero Chern number in zero external magnetic field is sometimes referred to as the quantum *anomolous* Hall effect. In this section we briefly outline this model and describe its phase diagram. In Chapter 3, this model will be used as a numerical setting for an investigation into the localization properties of Chern insulators.

The Haldane honeycomb model is defined on a honeycomb lattice. The honeycomb lattice is a bipartite lattice, and we will refer to sites of the two sublattices as A or B sites. The spacing between nearest neighbors is taken to be equal to one. The displacements between

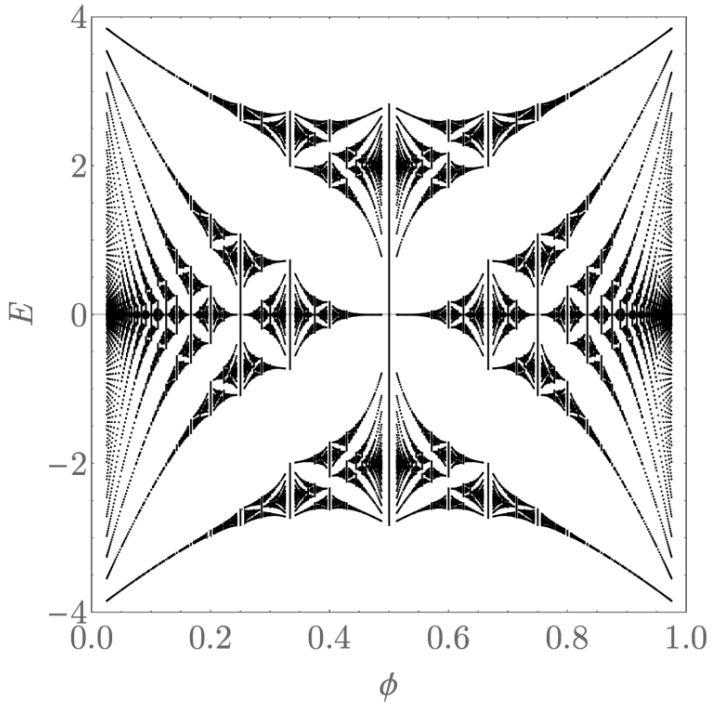

Figure 1.1: A depiction of the energy spectrum E of the Hofstadter model as a function of the flux ϕ piercing each plaquette, commonly referred to as the Hofstadter butterfly. (Figure adapted from Reference 17 with permission from the author.)

nearest neighbors are

$$\begin{aligned}\mathbf{a}_1 &= -\frac{\sqrt{3}}{2}\hat{\mathbf{x}} + \frac{1}{2}\hat{\mathbf{y}},\\ \mathbf{a}_2 &= \frac{\sqrt{3}}{2}\hat{\mathbf{x}} + \frac{1}{2}\hat{\mathbf{y}},\\ \mathbf{a}_3 &= -\hat{\mathbf{y}},\end{aligned}$$

and the displacements between next-nearest neighbors are

$$\begin{aligned}\mathbf{b}_1 &= -\sqrt{3}\hat{\mathbf{x}},\\ \mathbf{b}_2 &= \frac{\sqrt{3}}{2}\hat{\mathbf{x}} + \frac{3}{2}\hat{\mathbf{y}},\\ \mathbf{b}_3 &= \frac{\sqrt{3}}{2}\hat{\mathbf{x}} - \frac{3}{2}\hat{\mathbf{y}}.\end{aligned}$$

The noninteracting tight binding Hamiltonian is given in real space as

$$H = t_1 \sum_{\langle \mathbf{r}\mathbf{r}' \rangle} \left(c^\dagger_{\mathbf{r}'} c_{\mathbf{r}} + h.c. \right) + t_2 \sum_{\langle\langle \mathbf{r}\mathbf{r}' \rangle\rangle} \left(c^\dagger_{\mathbf{r}'} c_{\mathbf{r}} e^{i\phi_{\mathbf{r}\mathbf{r}'}} + h.c. \right) + \sum_{\mathbf{r}} M_{\mathbf{r}} c^\dagger_{\mathbf{r}} c_{\mathbf{r}} \tag{1.17}$$

where $\langle \mathbf{r}\mathbf{r}' \rangle$ represents pairs of nearest neighboring sites and $\langle\langle \mathbf{r}\mathbf{r}' \rangle\rangle$ represents pairs of next nearest neighboring sites. The hopping strengths for nearest neighbors and next-nearest neighbors are t_1 and t_2 respectively. $M_{\mathbf{r}} = \pm M$ represents the on-site potential, where the potential is positive on the A sites and negative on the B sites. The phase $\phi_{\mathbf{r}\mathbf{r}'} = \pm\phi$ is the phase of the next-nearest neighbor interaction, where the phase is positive for anti-clockwise terms or negative for clockwise terms [18]. The lattice structure and hopping terms are depicted in Figure 1.2.

As the system exhibits translation symmetry, we can block diagonalize the Hamiltonian in $\mathbf{k}$-space

$$H = \sum_{\mathbf{k}} \begin{pmatrix} c^\dagger_{\mathbf{k},A} & c^\dagger_{\mathbf{k},B} \end{pmatrix} H(\mathbf{k}) \begin{pmatrix} c_{\mathbf{k},A} \\ c_{\mathbf{k},B} \end{pmatrix},$$

where the 2×2 block Hamiltonian $H(\mathbf{k})$ is given by

$$H(\mathbf{k}) = 2t_2 \cos\phi \left(\sum_i \cos\left(\mathbf{k} \cdot \mathbf{b}_i\right) \right) \mathbb{I}_2 + t_1 \left(\sum_i \cos\left(\mathbf{k} \cdot \mathbf{a}_i\right) \boldsymbol{\sigma}_1 + \sin\left(\mathbf{k} \cdot \mathbf{a}_i\right) \boldsymbol{\sigma}_2 \right) + \left(M - 2t_2 \sin\phi \sum_i \sin\left(\mathbf{k} \cdot \mathbf{b}_i\right) \right) \boldsymbol{\sigma}_3,$$

and where $\boldsymbol{\sigma}_i$ are the normal Pauli matrices [18]. Grouping the coefficients of each Pauli matrix

$$H(\mathbf{k}) = H_0(\mathbf{k})\mathbb{I} + \sum_i H_i(\mathbf{k})\boldsymbol{\sigma}_i,$$

one determines the spectrum to be

$$E_\pm(\mathbf{k}) = H_0(\mathbf{k}) \pm \sqrt{\left(H_1(\mathbf{k})\right)^2 + \left(H_2(\mathbf{k})\right)^2 + \left(H_3(\mathbf{k})\right)^2}, \tag{1.18}$$

where E_+ and E_- refers to the spectrum of the upper and lower bands respectively. Interestingly although we can find the spectrum at each $\mathbf{k}$ analytically, it is not necessarily possible to determine the eigenvectors $|\psi_\pm(\mathbf{k})\rangle$ smoothly for all $\mathbf{k}$. The obstruction to doing this is indicated by the non-zero Chern number of the band.

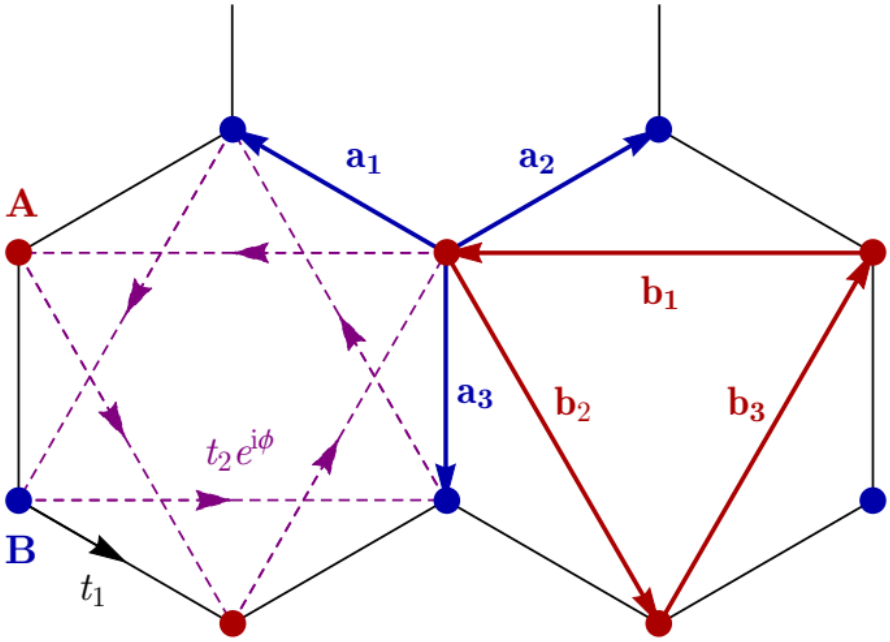

Figure 1.2: Illustration of the lattice structure and hopping elements for the Haldane honeycomb model. Sites belonging to the A and B sublattices are colored *red* and *blue* respectively. Sites separated by the blue vectors $\mathbf{a}_i$ are nearest neighbors, and sites separated by the red vectors $\mathbf{b}_i$ are the next-nearest neighbors. The purple arrows indicate the anti-clockwise orientation of the next-nearest hopping terms, which have a phase ϕ. Next-nearest neighbor hopping terms in the other direction have a phase $-\phi$. (Figure adapted from Reference 17 with permission from the author.)

Constraining the choice of parameters $|t_2| < |t_1|/3$ ensures the spectra of the bands will not overlap. From Equation (1.18) it is clear that the bands only touch if there is some $\mathbf{k}$ for which all three H_i vanish, which can only occur if $M = \pm 3\sqrt{3}t_2 \sin(\phi)$ [18]. These curves within the parameter space, with t_1 constant, define phase boundaries between different topological phases. Each phase can be characterized by the first Chern number C_1 of the lower band. The topological phase diagram for the Haldane model is depicted in Figure 1.3.

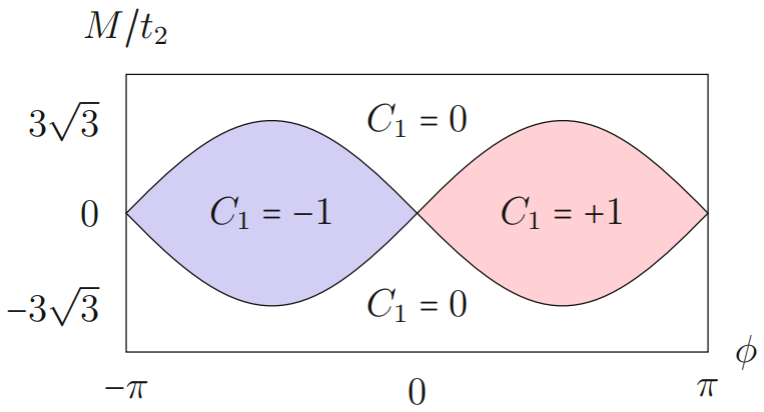

Figure 1.3: An illustration of topological phase diagram as a function of the ratio M/t_2 and the phase ϕ, as one keeps the parameter t_1 fixed. The blue and red regions indicate topological phases in which the lower band has first Chern number $C_1 = -1$ and $+1$ respectively. The white regions are trivial phases where the lower band has first Chern number $C_1 = 0$. The phase boundaries are the curves $M/t_2 = \pm 3\sqrt{3}\sin(\phi)$. At these phase boundaries the band gap vanishes. (Figure adapted from Reference 19 with permission from *Springer International Publishing*.)

1.1.4 Periodic table for topological insulators

Noninteracting topological insulators can be collectively thought of as systems of completely filled energy bands equipped with a quantity, known as a topological invariant, which is invariant to a class of perturbations which preserve the energy gap. The models we have described thus far are topologically protected against any gap preserving perturbation. However, by restricting the set of perturbations, one finds novel topological phases in many other dimensions.

The most common restrictions to the systems and perturbations correspond to the global symmetries of time-reversal Θ, particle-hole (charge conjugation) P, chiral symmetry C, and combinations thereof. These enumerate 10 symmetry classes, known as the Atland-Zirnbauer classes (originally defined in the context of random matrix theory) [20]. These symmetries are commonly described by their action on the $\mathbf{k}$-space Hamiltonian $H(\mathbf{k})$ (for translationally

invariant systems), which may be chosen to have the actions

$$\Theta H(\mathbf{k})\Theta^{-1} = H^*(-\mathbf{k}),$$
$$PH(\mathbf{k})P^{-1} = -H^*(-\mathbf{k}),$$
$$CH(\mathbf{k})C^{-1} = -H(\mathbf{k}).$$

Additionally the operators Θ and P are anti-unitary and may square to $+1$ or -1, which enumerate distinct classes. These operators are not independent, and one may show that symmetry under any two of the operators implies symmetry under the third.

The complete classification of systems within these symmetry classes in any dimension was performed by Kitaev in Reference 21, and we have reproduced this classification in Table 1.1. This classification relies on mathematical machinery known as the K-theory of vector bundles, which is beyond the scope of this thesis; we refer the reader to Reference 22 for details on topological K-theory. The techniques rely on relations between stable homotopy groups of vector bundles on tori of various symmetry class and dimension.

class	Θ	P	C	d = 0	1	2	3	4	5	6	7
A				$\mathbb{Z}$	$\emptyset$	$\mathbb{Z}$	$\emptyset$	$\mathbb{Z}$	$\emptyset$	$\mathbb{Z}$	$\emptyset$
AIII			1	$\emptyset$	$\mathbb{Z}$	$\emptyset$	$\mathbb{Z}$	$\emptyset$	$\mathbb{Z}$	$\emptyset$	$\mathbb{Z}$
AI	+1			$\mathbb{Z}$	$\emptyset$	$\emptyset$	$\emptyset$	$\mathbb{Z}$	$\emptyset$	$\mathbb{Z}_2$	$\mathbb{Z}_2$
BDI	+1	+1	1	$\mathbb{Z}_2$	$\mathbb{Z}$	$\emptyset$	$\emptyset$	$\emptyset$	$\mathbb{Z}$	$\emptyset$	$\mathbb{Z}_2$
D		+1		$\mathbb{Z}_2$	$\mathbb{Z}_2$	$\mathbb{Z}$	$\emptyset$	$\emptyset$	$\emptyset$	$\mathbb{Z}$	$\emptyset$
DIII	-1	+1	1	$\emptyset$	$\mathbb{Z}_2$	$\mathbb{Z}_2$	$\mathbb{Z}$	$\emptyset$	$\emptyset$	$\emptyset$	$\mathbb{Z}$
AII	-1			$\mathbb{Z}$	$\emptyset$	$\mathbb{Z}_2$	$\mathbb{Z}_2$	$\mathbb{Z}$	$\emptyset$	$\emptyset$	$\emptyset$
CII	-1	-1	1	$\emptyset$	$\mathbb{Z}$	$\emptyset$	$\mathbb{Z}_2$	$\mathbb{Z}_2$	$\mathbb{Z}$	$\emptyset$	$\emptyset$
C		-1		$\emptyset$	$\emptyset$	$\mathbb{Z}$	$\emptyset$	$\mathbb{Z}_2$	$\mathbb{Z}_2$	$\mathbb{Z}$	$\emptyset$
CI	+1	-1	1	$\emptyset$	$\emptyset$	$\emptyset$	$\mathbb{Z}$	$\emptyset$	$\mathbb{Z}_2$	$\mathbb{Z}_2$	$\mathbb{Z}$

Table 1.1: The periodic table of topological insulators in $d \leq 7$, first determined for all symmetry classes and dimensions using a K-theoretic approach in Reference 21. Each symmetry class is labeled by ± 1 for each symmetry it obeys, where the sign indicates the square of the operator. Each entry of the table indicates the possible values of the topological invariant distinguishing topologically distinct systems. The classification is 8-periodic in d, a K-theoretic result stemming from Bott periodicity [23].

Each entry of Table 1.1 corresponds to the range of topological invariants taken by various systems in the symmetry class and dimension. At the boundary of such a system the values of these invariants correspond to the number of protected gapless modes. We note that the IQHE belongs to class A and $d = 2$ in Table 1.1, and the classification $\mathbb{Z}$ corresponds to possible Chern numbers. By considering filling ν Landau levels, and by considering systems with the opposite magnetic field, we can achieve all topological invariants in this class.

We note that although the complete classification for all classes and dimensions was performed in Reference 21, many specific cases had already been investigated in detail. For example for class D in $d = 1$ [24] and $d = 2$ [25, 26] or for class AII in $d = 2$ [27–29] and $d = 3$ [30–32].

1.2 Floquet topological phases

Systems driven periodically in time, commonly called Floquet systems, can generate behavior with an intrinsically dynamical character. In this rapidly evolving field of Floquet systems, recent advances include the prediction of phases that exhibit an analog of symmetry breaking in the time domain, known as discrete time crystals or π-spin glasses [33–37], as well as a host of novel topological phases that lie beyond any static characterization [38–55]. These theoretical works have been complemented by significant experimental advances, with analogs of Floquet topological phases being realized in a variety of different settings [56–60]. Here we briefly introduce Floquet systems, before revisiting them in Chapters 4 and 5.

1.2.1 Overview of Floquet systems

We begin by reviewing some elementary definitions regarding Floquet systems which will be of use to us. These definitions are reproduced in a number of articles. We recommend the excellent review article Reference 61 regarding Floquet systems, especially in context of topological phases, should the reader desire a more in-depth introduction to these systems.

As opposed to static systems whose Hamiltonians are time-independent, driven systems

are characterized by Hamiltonians $H(t)$ which are explicitly time-dependent. The behavior of such systems is captured by the unitary time-evolution operator $U(t, t_0)$, defined by

$$U(t, t_0) = \mathcal{T} \exp\left[-i \int_{t_0}^{t} H(t')\mathrm{d}t'\right],$$

where $\mathcal{T}$ denotes the time-ordering operator. Formally expanding the time-evolution operator, one has

$$U(t, t_0) = \mathbb{I} + \sum_{n=0}^{\infty} \frac{1}{n!} (-i)^n \int_{t_0}^{t} \mathrm{d}t_1 \int_{t_0}^{t} \mathrm{d}t_2 \cdots \int_{t_0}^{t} \mathrm{d}t_n \mathcal{T}\left[H(t_1)H(t_2)\cdots H(t_n)\right].$$

The operator $U(t, t_0)$ dictates the unitary time-evolution of the system between times t_0 and t. We will often use the more compact notation $U(t)$ which is shorthand for $U(t, t_0 = 0)$.

In this thesis, we are primarily interested in a subset of driven systems known as Floquet systems. Floquet systems are characterized by those driven systems whose Hamiltonians are periodic in time,

$$H(t + T) = H(t)$$

where T denotes the time period. Although the Hamiltonian is time-periodic of period T, the unitary operator $U(t)$ is not guaranteed to be periodic. The eigenstates of the unitary time-evolution by one period $U(T)$ are given by $|\phi_\alpha\rangle$ satisfying

$$U(T)\,|\phi_\alpha\rangle = \exp\left(-i\epsilon_\alpha T\right)|\phi_\alpha\rangle$$

where the eigenvalues $\lambda_\alpha = \exp\left(-i\epsilon_\alpha T\right)$ are pure phases (as the operator was unitary), and are written in terms of the *quasienergies* ϵ_α, which are defined modulo $\frac{2\pi}{T}$.

The time-evolution operator $U(t)$ can be written

$$U(t) = \Phi(t) \exp\{-itH_F\} \tag{1.19}$$

where $\Phi(t)$ is a unitary operator of the same periodicity as the underlying Hamiltonian $\Phi(t + T) = \Phi(t)$, and H_F is a time-independent Hermitian operator, often called the Floquet Hamiltonian [61]. The Floquet Hamiltonian H_F may be written

$$H_F = \frac{i}{T} \log\left(U(T)\right) \tag{1.20}$$

and is not unique, but rather defined up to the choice of branch cut for the complex logarithm. Equation 1.19 is a rephrasing of Floquet's theorem [62], an analog of Bloch's theorem for systems with discrete time-translation symmetry.

The unitary operator will be periodic with the same period T, that is $U(t+T) = U(T)$, if and only if

$$U(T) = \mathbb{I}, \tag{1.21}$$

in which case we will refer to the driven system as being a *loop drive*. Loop drives, although not generic, will be a useful construction within the context of the classification of Floquet systems which we will revisit in Section 4.1.

1.2.2 A relevant example: Rudner model

In this section we describe the prototypical model of a Floquet topological phase, originally described by Rudner et al. in Reference 40. We will refer to this model as the Rudner model, and will see that it is a single particle analog of the interacting swap models described in Chapters 4 and 5.

Consider a bipartite lattice in two dimensions with geometry such that the two orbitals at each unit cell, denoted orbital A and orbital B, form a checkerboard arrangement. We denote the sublattice of the A/B orbitals as $\mathcal{L}_{A/B}$. The Hamiltonian is then given by

$$H(t) = \sum_{\mathbf{k}} \left(c^\dagger_{\mathbf{k},A} \; c^\dagger_{\mathbf{k},B} \right) H(\mathbf{k}, t) \begin{pmatrix} c_{\mathbf{k},A} \\ c_{\mathbf{k},B} \end{pmatrix}$$

where $c_{\mathbf{k},(A/B)}$ is an annihilation operator for a particle with crystal momentum $\mathbf{k}$ completely on sublattice (A/B) and $c^\dagger_{\mathbf{k},(A/B)}$ is the corresponding creation operator. The time-dependent $\mathbf{k}$-space Hamiltonian is given by

$$H(\mathbf{k}, t) = -\sum_{n=1}^{4} J_n(t) \left(\exp\left(i\mathbf{b}_n \cdot \mathbf{k}\right) \sigma^+ + \exp\left(-i\mathbf{b}_n \cdot \mathbf{k}\right) \sigma^- \right) \tag{1.22}$$

where the linear combinations of Pauli matrices

$$\sigma^+ = \frac{\sigma_x + i\sigma_y}{2},$$
$$\sigma^- = \frac{\sigma_x - i\sigma_y}{2},$$

act on the orbital space. The strengths $J_n(t)$ are chosen such that the Hamiltonian is piecewise constant,

$$J_n(t) = \begin{cases} 1 & \text{if } \frac{(n-1)\pi}{2} \leq t < \frac{n\pi}{2} \\ 0 & \text{otherwise} \end{cases},$$

and the real-space vectors $\mathbf{b}_n$ are chosen to be $\mathbf{b}_1 = (a, 0)$, $\mathbf{b}_2 = (0, a)$, $\mathbf{b}_3 = (-a, 0)$, and $\mathbf{b}_4 = (0, -a)$ [40]. We will without loss of generality choose the lattice spacing $a = 1$.

The time-dependence of the Hamiltonian can be viewed as follows: During each step A and B orbitals are disjointly paired off, as depicted in Figure 1.4, with the pairing depending on $\mathbf{b}_n$. During the course of each step n, a state which is completely localized at a particular A/B orbital will transition to be localized at the paired B/A orbital. Formally, we may write the action of each complete step n as a unitary operator

$$U_n = \sum_{\mathbf{r} \in \mathcal{L}_\mathbf{A}} c^\dagger_{\mathbf{r}+\mathbf{b}_n, A} c_{\mathbf{r}, B} + c^\dagger_{\mathbf{r}, B} c_{\mathbf{r}+\mathbf{b}_n, A}.$$

It is therefore easy to verify the action of one complete driving period in the bulk is the identity. A state $|\mathbf{r}, A\rangle$, initially prepared to be completely localized at an A orbital, follows the trajectory

$$\begin{aligned} U(0)\,|\mathbf{r}, A\rangle &= \mathbb{I}\,|\mathbf{r}, A\rangle = |\mathbf{r}, A\rangle\,, \\ U(\pi/2)\,|\mathbf{r}, A\rangle &= U_1\,|\mathbf{r}, A\rangle = |\mathbf{r} + (-1, 0), B\rangle\,, \\ U(\pi)\,|\mathbf{r}, A\rangle &= U_2 \cdot U_1\,|\mathbf{r}, A\rangle = |\mathbf{r} + (-1, 1), A\rangle\,, \\ U(3\pi/2)\,|\mathbf{r}, A\rangle &= U_3 \cdot U_2 \cdot U_1\,|\mathbf{r}, A\rangle = |\mathbf{r} + (0, 1), B\rangle\,, \\ U(2\pi)\,|\mathbf{r}, A\rangle &= U_4 \cdot U_3 \cdot U_2 \cdot U_1\,|\mathbf{r}, A\rangle = |\mathbf{r}, A\rangle\,, \end{aligned}$$

i.e., follows a counter-clockwise trajectory encircling one plaquette to its upper left, as depicted in Figure 1.5. Similarly, a state initially localized at a B orbital in the bulk follows

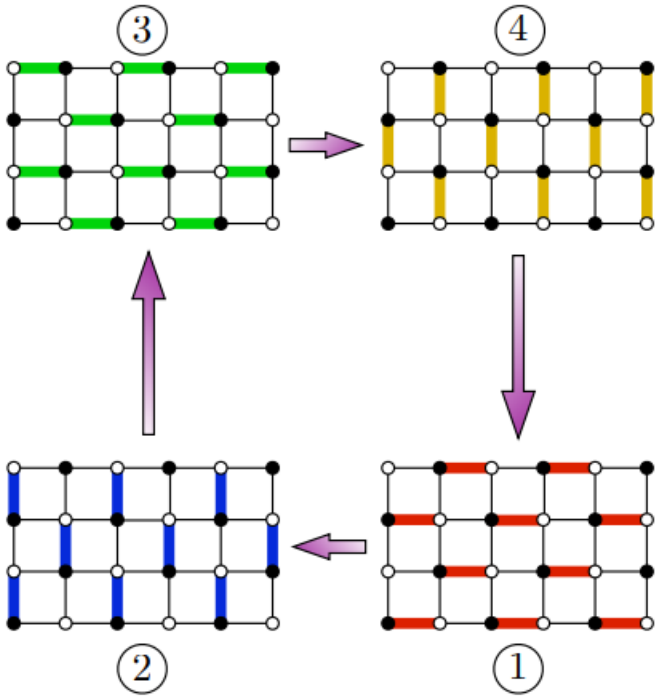

Figure 1.4: Depiction of the four step Rudner model described in Section 1.2.2. Here the A orbitals are depicted in white and the B orbitals are depicted in black. During each step a hopping strength of $J = 1$ is applied along each set of highlighted hoppings for a time $\Delta t = \pi/2$, for a total cycle period of $T = 2\pi$. Each set of paired orbitals is identical to a two level system undergoing Rabi oscillations. During the duration of each step a particle initially localized at an A orbital will undergo a transition to a completely localized particle at the paired B orbital, and vice-versa. (Figure adapted from Reference 61 with permission from *Annual Reviews of Condensed Matter Physics*.)

a counter-clockwise trajectory encircling one plaquette to its lower right. In particular, this drive satisfies the loop condition Equation (1.21). As a result the Floquet Hamiltonian H_F, defined in Equation (1.20), is identically zero in the bulk. We will see that despite this fact, this system exhibits nontrivial anomalous boundary behavior.

Although the action of the unitary time-evolution operator corresponding to a complete cycle of a Floquet drive may act as the identity operator on states supported in the bulk, this property does not necessarily extend to the boundary of the system. There are many ways one can introduce boundary conditions to the system, however physical boundary conditions all generate the same equivalence class of local unitary operators, which we detail in Chapter 4. This equivalence of boundary conditions will be essential to the classification of topological Floquet systems.

In this section, for simplicity, we limit ourselves to the investigation of the boundary conditions which simply remove terms in the real-space representation of the Hamiltonian if they include creation or annihilation operators for any sites beyond the boundary. The effect of this on the unitary time-evolution may be analyzed by simply considering the action of this operator on states initially localized at orbitals near the boundary.

We consider a strip geometry, extended with periodic boundary conditions along one dimension of the underlying lattice, and open boundary conditions in the other dimension. The action of the unitary operator on states initially localized at orbitals in the vicinity of the boundary is depicted in Figure 1.5.

For example, we consider the action of the unitary time-evolution operator on a state initially completely localized at an A orbital along the upper open boundary. The action of the first quarter of the drive U_1 is unmodified for this orbital and drives a transition to the B orbital to its left. The action of the second quarter of the drive U_2 now acts as the identity operator, as the paired site is outside of the boundary, and the state remains localized at the same B orbital. The action of the third quarter of the drive U_3 remains unmodified for this orbital and drives a transition to the A orbital to its left. Finally, the action of the fourth quarter of the drive U_4 is modified to the identity as well. So the net action of one driving

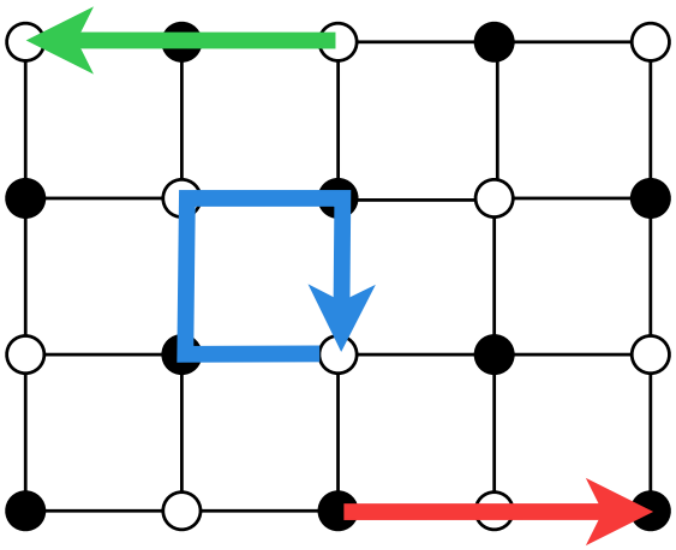

Figure 1.5: A depiction of the action of the time-evolution operator $U(t)$ for the Rudner model on states initially localized at single orbitals, in a system with a strip geometry and the boundary conditions described in Section 1.2.2. States localized in the bulk follow a sequence of four transitions to complete a counterclockwise circuit around a plaquette to their upper left. States localized at a A orbital on the upper boundary/B orbitals on a lower boundary are effectively translated to the left/right as shown by the green/red arrow. (Figure adapted from Reference 61 with permission from *Annual Reviews of Condensed Matter Physics*.)

period $U(T)$ is to translate along the upper boundary an A orbital to the A orbital on its left.

One can also perform a similar analysis for other states initially localized on the boundary. We omit the step-by-step analysis, but briefly note the results. The action of the time-evoltuion operator on states initially localized at B orbitals on the lower boundary is modified in a similar way to the A orbitals on the upper boundary. Two of the driving steps (U_2 and U_4) are effectively the identity on these states. The action of the entire driving period on these states is modified to be a translation to the right to the adjacent B orbital. The action of the time-evolution operator on A orbitals on the lower boundary or B orbitals on the upper boundary remains unchanged as the identity. This is expected as the bulk action of the unitary is to circulate A orbitals around a plaquette to their upper left and B orbitals around a plaquette to their lower right, and so the introduction of the boundary does not

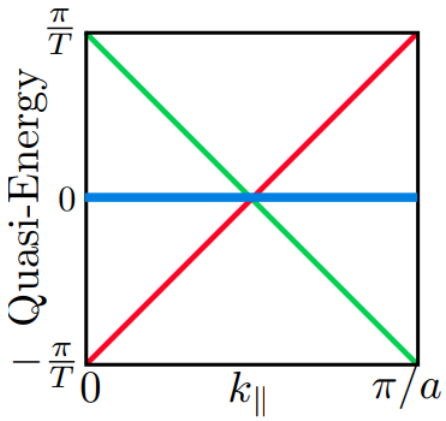

Figure 1.6: The quasi-energy spectrum (as a function of crystal momentum parallel to the boundary $k_{||}$) of the unitary time-evolution operator $U(T)$ for the Rudner model with a strip geometry, as defined in Section 1.2.2. In the bulk the action of the unitary time-evolution operator is the identity, and so states in the bulk form a degenerate band of quasi-energy zero. The action of the unitary time-evolution operator on the upper/lower boundaries is translation to the left/right. The left/right moving chiral edge modes are shown in green/red and wind around the quasi-energy space. These left/right moving modes cannot be deformed to the identity by any locally generated perturbations. (Figure adapted from Reference 61 with permission from *Annual Reviews of Condensed Matter Physics*.)

change any of the terms involving these orbitals.

We note that the model originally presented by Rudner et al. in Reference 40 was substantially more generic than the one reproduced here. In particular the hopping strengths $J_n(t)$ were not fine-tuned to be 1, and there was an additional fifth step in which orbitals in each unit-cell were mixed. We choose not to present those details here as they do not impact the topological properties of this model. In Chapters 4 and 5 we will see that the specific parameters chosen above capture a model whose essentially dynamical topological nature has been isolated. We will also introduce a generalization of this drive which retains its simplicity, but exhausts the topological classification of 2D drives without symmetry.

1.2.3 Topological invariants and edge modes

The Rudner model described in Section 1.2.2 is the prototypical example of a Floquet topological insulator. We saw that although the action of the time-evolution operator was the identity in the bulk, the restriction of the system to a boundary resulted in a non-trivial operator which acted as a chiral translation operator. In particular, the quasi-energy spectrum of the unitary operator restricted to a boundary contained a band which wound around the unit-circle, as depicted in Figure 1.6.

There are other unitary operators, of course, which behave trivially in the bulk as well as at the boundary. In addition, there are numerous ways to implement physical boundary conditions for an open system, which may lead to more complicated edge spectra. In this section we introduce tools, in particular topological invariants, from the literature to characterize topologically distinct Floquet systems. We will limit our discussion to single particle systems in this section, however in Chapter 4 we will extend this to the many-body case.

As we discussed in Section 1.1.2, single particle static systems with nontrivial topology exhibit bulk-boundary correspondence connecting some topological invariant, associated with the bulk Hamiltonian, with edge modes protected against classes of perturbations.

There is a large class of topological behavior in single particle Floquet systems which is of the same character as that already included in the classification of static systems. Applying the existing static classification to the Floquet Hamiltonian H_F associated with the bulk time-evolution operator of a Floquet drive directly leads to a partial classification of the topological behavior of Floquet systems. This portion of the classification does not realize any novel topological properties not present in static systems. For example, a static system whose Hamiltonian is equal to, or topologically equivalent to, the Floquet Hamiltonian of a driven system will share the same static classification. The reproduction of the static classification will therefore not be the focus of our discussion. However, it is useful to note that while reproducing the same physics as their static counterparts, systems with specific static invariants may be more experimentally accessible in the driven setting than the static

setting [38, 58, 63–66].

On the other hand, there is topological behavior present in some driven systems which is not equivalent to that present in any static system. Indeed the Rudner model described above has Floquet Hamiltonian identically zero $H_F = 0$, and therefore not topological by any static characterization, but still admits chiral edge modes which we will see are topologically protected. The Rudner model, as presented in Section 1.2.2, satisfies the loop condition Equation (1.21). The bulk time-evolution operator $U(t, k_x, k_y)$, as noted in Reference 40, is a periodic function of not only k_x and k_y but also t. Based on mathematical considerations alone, Reference 40 suggests a topological index introduced in Reference 23 as a possible candidate topological invariant. The suggested index $W[U]$ classifies maps from $S_1 \times S_1 \times S_1 \to U(N)$ [23], and is given to be

$$W[U] = \frac{1}{8\pi^2} \int \mathrm{d}t \; \mathrm{d}k_x \; \mathrm{d}k_y \times \mathrm{Tr}\Big\{U^{-1}\partial_t U[U^{-1}\partial_{k_x} U, U^{-1}\partial_{k_y} U]\Big\}. \tag{1.23}$$

Rudner et al. also show that the number of chiral edge modes n_{edge} which propagate across the quasi-energy spectrum at any boundary is equal to $W[U]$; we do not discuss the mathematical derivation of this correspondence here and suggest the reader refer to Appendix A of Reference 40 for details. In Section 4.2 of this thesis, we review portions of Reference 67 which shows that simple edge behavior of this type exhausts the topological edge classification of single particle Floquet systems with no symmetry in two dimensions.

The bulk topological invariant introduced in Equation 1.23 is only valid for systems satisfying the loop condition $U(t + T) = U(t)$, and therefore may not be applied to general Floquet systems without modification. In Chapter 4 we formalize the ideas of equivalence of Floquet drives and introduce a procedure for deforming any Floquet drive to a loop drive which shares its topological characterization. Furthermore we will introduce edge invariants for interacting systems and establish equivalence between effective edge behaviors.

1.2.4 Periodic table for Floquet topological insulators

The Rudner model described in Section 1.2.2 is an example of a Floquet system with topologically protected chiral edge modes. These modes cannot be created or removed from the system through any locally generated perturbation confined to the edge of the system. In particular, the underlying and perturbing Hamiltonian in this example does not have to meet any additional symmetry requirements and belong to class A of the Altland-Zirnbauer class. The classification of class A loop drives should be enumerated by the image of the invariant in Equation (1.23), i.e. $\mathbb{Z}$ [40]. By running the Rudner model of Section 1.2.2 (or its inverse) n times in succession, one can achieve any element of this classification.

Similar to the classification of static systems discussed in Section 1.1.4, Floquet systems of different symmetry classes and dimensions have different topological classifications. Although our work in Chapters 4 and 5 is concerned with systems not confined by additional symmetry (i.e., class A and its many-body analog), we briefly review the complete classification of noninteracting systems for completeness.

The Altland-Zirnbauer classes representing different discrete symmetries are characterized by combinations of time-reversal Θ, particle-hole (charge conjugation) P, and chiral symmetry C. The classes are identical to those described in Section 1.1.4. However, the time-dependence of the Hamiltonian in Floquet systems gives the action of these symmetry operators a more complex form, derived in Appendix A of Reference 49, in terms of the unitary time-evolution operator by

$$\begin{aligned} PU(\mathbf{k},t)P^{-1} &= U^*(-\mathbf{k},t), \\ \Theta U(\mathbf{k},t)\Theta^{-1} &= U^*(-\mathbf{k},T-t)U^{\dagger *}(-\mathbf{k},T), \\ CU(\mathbf{k},t)C^{-1} &= U(\mathbf{k},T-t)U^{\dagger}(\mathbf{k},T). \end{aligned}$$

The classification of noninteracting Floquet systems was performed by Roy and Harper in Reference 49 using K-theoretic methods similar to those used by Kitaev for static systems in Reference 21. The classification again amounts to a periodic table, reproduced in Table 1.2, which bears resemblance to the one found for static systems in Reference 21. In particular

we notice that each entry of Table 1.2 is either $\emptyset$, indicating that no topological phases are hosted in that dimension and symmetry, or the product of two identical factors. The general approach used in Reference 49 is to modify a general drive by continuously deforming it into a loop drive followed by a drive generated by a static Hamiltonian. The two factors in each entry of the classification can be attributed to one of these two unitary components. It is also shown in Reference 49 that this bulk classification is related to the number of edge modes occurring at a system's boundary.

class	Θ	P	C	d = 0	1	2	3	4	5	6	7
A				$\mathbb{Z}\times\mathbb{Z}$	$\emptyset$	$\mathbb{Z}\times\mathbb{Z}$	$\emptyset$	$\mathbb{Z}\times\mathbb{Z}$	$\emptyset$	$\mathbb{Z}\times\mathbb{Z}$	$\emptyset$
AIII			1	$\emptyset$	$\mathbb{Z}\times\mathbb{Z}$	$\emptyset$	$\mathbb{Z}\times\mathbb{Z}$	$\emptyset$	$\mathbb{Z}\times\mathbb{Z}$	$\emptyset$	$\mathbb{Z}\times\mathbb{Z}$
AI	+1			$\mathbb{Z}\times\mathbb{Z}$	$\emptyset$	$\emptyset$	$\emptyset$	$\mathbb{Z}\times\mathbb{Z}$	$\emptyset$	$\mathbb{Z}_2\times\mathbb{Z}_2$	$\mathbb{Z}_2\times\mathbb{Z}_2$
BDI	+1	+1	1	$\mathbb{Z}_2\times\mathbb{Z}_2$	$\mathbb{Z}\times\mathbb{Z}$	$\emptyset$	$\emptyset$	$\emptyset$	$\mathbb{Z}\times\mathbb{Z}$	$\emptyset$	$\mathbb{Z}_2\times\mathbb{Z}_2$
D		+1		$\mathbb{Z}_2\times\mathbb{Z}_2$	$\mathbb{Z}_2\times\mathbb{Z}_2$	$\mathbb{Z}\times\mathbb{Z}$	$\emptyset$	$\emptyset$	$\emptyset$	$\mathbb{Z}\times\mathbb{Z}$	$\emptyset$
DIII	-1	+1	1	$\emptyset$	$\mathbb{Z}_2\times\mathbb{Z}_2$	$\mathbb{Z}_2\times\mathbb{Z}_2$	$\mathbb{Z}\times\mathbb{Z}$	$\emptyset$	$\emptyset$	$\emptyset$	$\mathbb{Z}\times\mathbb{Z}$
AII	-1			$\mathbb{Z}\times\mathbb{Z}$	$\emptyset$	$\mathbb{Z}_2\times\mathbb{Z}_2$	$\mathbb{Z}_2\times\mathbb{Z}_2$	$\mathbb{Z}\times\mathbb{Z}$	$\emptyset$	$\emptyset$	$\emptyset$
CII	-1	-1	1	$\emptyset$	$\mathbb{Z}\times\mathbb{Z}$	$\emptyset$	$\mathbb{Z}_2\times\mathbb{Z}_2$	$\mathbb{Z}_2\times\mathbb{Z}_2$	$\mathbb{Z}\times\mathbb{Z}$	$\emptyset$	$\emptyset$
C		-1		$\emptyset$	$\emptyset$	$\mathbb{Z}\times\mathbb{Z}$	$\emptyset$	$\mathbb{Z}_2\times\mathbb{Z}_2$	$\mathbb{Z}_2\times\mathbb{Z}_2$	$\mathbb{Z}\times\mathbb{Z}$	$\emptyset$
CI	+1	-1	1	$\emptyset$	$\emptyset$	$\emptyset$	$\mathbb{Z}\times\mathbb{Z}$	$\emptyset$	$\mathbb{Z}_2\times\mathbb{Z}_2$	$\mathbb{Z}_2\times\mathbb{Z}_2$	$\mathbb{Z}\times\mathbb{Z}$

Table 1.2: The periodic table for Floquet topological insulators for dimensions $d \leq 7$ was first determined for all symmetry classes using a K-theoretic approach in Reference 49. Each entry is either $\emptyset$ or the product of two factors; the first and second factor in the classification accounts for the static component and dynamical component (of the associated loop drive) respectively. Each entry of this classification may be associated with the value of a topological invariant associated with a quasi-energy gap in the unitary time-evolution operator. The classification is 8-periodic in d, a K-theoretic result stemming from Bott periodicity [68]. (Table adapted from Reference 49 with permission from the *American Physical Society*.)

In the latter half of this thesis we explore interacting Floquet systems without additional symmetry and their topological classification. In Chapter 4 we review the loop decomposition of drives, introduced in Reference 49, which isolates the dynamical nature of the drive and can be extended to some interacting systems. Our goal in Chapter 5 is the classification of the many-body analogs of noninteracting class A systems in dimension $d = 3$.

1.3 Outline of this thesis

The remainder of this thesis consists of two parts. The first part, comprising Chapters 2 and 3, details our numerical investigation of localization measures in static 2D systems.

In Chapter 2, we discuss aspects of localization of static class A systems in $d = 2$. We review various constructions for Wannier functions in these systems, as well as the results limiting the degree of localization possibly attained for such Wannier functions. We continue to discuss the construction of coherent states in the lowest Landau level, followed by results regarding minimal complete sets of such coherent states and the symmetric orthogonalization of these minimal sets. We then provide an overview of the plateaux transition and disorder in the IQHE. We conclude the chapter by reviewing aspects of the theory and implementation of finite size scaling for the determination of critical exponents.

In Chapter 3, we introduce methods to numerically study the obstruction to localization in topological class A systems in $d = 2$. We develop a number of procedures, each of which eliminate a fraction of the Hilbert space as localized degrees of freedom and study the localization properties of the effective system with these degrees of freedom removed. We find a distinct signature of said obstruction using each procedure, which appears to be universal across systems with non-zero Chern number. We conclude with a discussion and suggestions for future directions.

The second part of this thesis, comprising Chapters 4 and 5, details our classification of interacting 3D Floquet systems.

In Chapter 4, we begin by discussing the loop decomposition and homotopy approach to the classification of Floquet topological phases. We proceed to review the approach of classification of loop drives by their effective action at a boundary, which we refer to as the effective edge unitary. We review this first for the one dimensional noninteracting case, before continuing to the one dimensional many-body case. In doing this we pay particular attention to the many-body topological edge invariant, which we refer to as the GNVW index.

In Chapter 5, we identify distinct types of boundary behaviors which occur at the 2D

boundary of a 3D many-body loop drive. This is accomplished via the generalization of the aforementioned GNVW index. We proceed to review many-body generalizations of the Rudner drive, referred to as exchange drives, and extend these to three dimensions. We find a bulk-edge correspondence for 3D exchange drives, and show that they exhaust our 2D edge classification. We conclude with a contextual discussion of our work and suggestions for future directions.

CHAPTER 2

Background for our work on localization in static topological insulators

---

Portions of this chapter are adapted from the publication:

Reiss, D., Harper, F., and Roy, R. *Numerical localization signatures of topology in two dimensional insulators.* (In preparation, 2020).

In Section 1.1 we introduced 2D static noninteracting topological systems in class A and outlined some of their distinguishing properties. In this chapter we offer an exposition of existing results and techniques for these 2D class A systems which provide motivation and a foundation for our work in Chapter 3. This material focuses on the interplay between the mutual localization of wavefunctions in real space and the topology of the Hilbert space to which those functions belong.

2.1 Wannier functions

2.1.1 Definition and basic properties

Introduced by Wannier [69, 70], Wannier functions are orthogonal wavefunctions spanning a complete set of electronic bands. Each member of such a set is indexed and centered at a site $\mathbf{R}$ of the underlying lattice, typically decaying quickly away from this site. Although one may construct Wannier functions corresponding to several filled electronic bands, we limit

our discussion here to 2D systems comprising a single filled band for our work in Chapter 3. For a comprehensive introduction to Wannier functions we refer the reader to Reference 71.

We note that in the discussion below, we assume that the system is translation invariant and Wannier functions form a representation of the translation group. In a system which instead has magnetic translation symmetry, the definitions are altered so that the resulting Wannier functions instead form a representation of the magnetic translation group.

Without loss of generality, we make the assumption that the underlying lattice $\mathcal{L}$ is square of unit spacing. Given a translationally invariant Hamiltonian, one can find the Bloch states $|\psi_{\mathbf{k}}\rangle$ corresponding to the band in question through diagonalization. The corresponding Wannier functions $|\phi_{\mathbf{R}}\rangle$ can be constructed as

$$|\phi_{\mathbf{R}}\rangle = \frac{1}{\sqrt{N}} \sum_{\mathbf{k}} \exp\left(-i\mathbf{k}\cdot\mathbf{R}\right) |\psi_{\mathbf{k}}\rangle\,, \tag{2.1}$$

where N is the number of primitive cells in the system. In the thermodynamic limit $N \to \infty$, the sum in Equation (2.1) becomes an integral over the Brillouin zone. Unlike Bloch functions, the Wannier functions are L^2 functions and are normalized. A set of Wannier functions enjoys a number of useful properties. In particular, for any two lattice sites $\mathbf{R}$ and $\mathbf{R}'$, the Wannier functions $|\phi_{\mathbf{R}}\rangle$ and $|\phi'_{\mathbf{R}}\rangle$ are orthonormal,

$$\langle\phi_{\mathbf{R}}|\phi_{\mathbf{R}'}\rangle = \delta_{\mathbf{R},\mathbf{R}'}.$$

In addition, the set of Wannier functions is closed under lattice translations. Given the Wannier function $|\phi_{\mathbf{R}}\rangle$ centered at lattice site $\mathbf{R}$ and any lattice vector $\mathbf{R}'$, the Wannier function $|\phi_{\mathbf{R}+\mathbf{R}'}\rangle$ is the real space translate of $|\phi_{\mathbf{R}}\rangle$ by $\mathbf{R}'$, i.e.

$$\langle\mathbf{r}|\phi_{\mathbf{R}}\rangle = \langle\mathbf{r}+\mathbf{R}'|\phi_{\mathbf{R}+\mathbf{R}'}\rangle\,.$$

The transformation from Bloch states to the Wannier functions, Equation (2.1), may be inverted as

$$|\psi_{\mathbf{k}}\rangle = \frac{1}{\sqrt{N}} \sum_{\mathbf{R}} \exp\left(i\mathbf{k}\cdot\mathbf{R}\right) |\phi_{\mathbf{R}}\rangle\,. \tag{2.2}$$

These identities may be easily verified using Equation (2.1) and Bloch's theorem.

2.1.2 Maximally localized Wannier functions

Wannier functions constructed from the basis of Bloch states in Equation (2.1) are not unique. This non-uniqueness is a consequence of the gauge freedom to redefine the Bloch states by a smooth real $\mathbf{k}$-dependent phase factor $\chi(\mathbf{k})$

$$|\psi'_{\mathbf{k}}\rangle = \exp\left(i\chi(\mathbf{k})\right)|\psi_{\mathbf{k}}\rangle\,.$$

The choice of gauge $\chi(\mathbf{k})$ can change the shape and spread of the resulting Wannier functions.

It is often useful to make a choice of $\chi(\mathbf{k})$ resulting in Wannier functions which are maximally localized, according to some metric. A localization metric Ω commonly used for Wannier functions, defined as

$$\Omega = \langle\phi_{\mathbf{0}}|\, r^2\,|\phi_{\mathbf{0}}\rangle - \langle\phi_{\mathbf{0}}|\,\mathbf{r}\,|\phi_{\mathbf{0}}\rangle^2\,, \tag{2.3}$$

measures the second central moment of the Wannier function at the origin. The metric Ω in Equation (2.3) is the single band form of the *Marzari-Vanderbilt criterion* [72]. One may approach minimization of the functional Ω analytically using a variational approach [71], or computationally through searching the space of smooth functions $\chi(\mathbf{k})$ [73]. Other localization metrics have been considered [74–76]; we restrict our discussion of maximally localized Wannier functions to the metric Ω. In most generic systems these maximally localized Wannier functions decay exponentially away from their central cell [77–80]. However, as we discuss below, when a band has non-zero Chern number the decay of Wannier functions is necessarily slower than exponential.

2.1.3 Projection method for construction of Wannier functions

Aside from the construction of Wannier functions in Equation (2.1), one can also construct Wannier functions through projection of trial functions [81]. Explicitly, consider a trial function $|g_{\mathbf{0}}\rangle$ localized about the origin and project it to the band spanned by the Bloch states

$$|g'_{\mathbf{0}}\rangle = \sum_{\mathbf{k}} |\psi_{\mathbf{k}}\rangle\,\langle\psi_{\mathbf{k}}|g_{\mathbf{0}}\rangle\,.$$

The projected function $|g'_{\mathbf{0}}\rangle$ is then translated to each lattice site to form the set $\{|g'_{\mathbf{R}}\rangle = t(\mathbf{R})\,|g'_{\mathbf{0}}\rangle\}$. This set is not necessarily mutually orthogonal, but generally linearly independent if the initial trial wavefunction $|g_{\mathbf{0}}\rangle$ is sufficiently localized [71]. One may then symmetrically orthogonalize the set $\{|g'_{\mathbf{R}}\rangle\}$, as described in Appendix 2.A, to obtain Wannier functions $\{|\phi_{\mathbf{R}}\rangle\}$. We note that the gauge freedom described in Section 2.1.2 is contained indirectly within this construction in the choice of the trial wavefunction.

2.1.4 Impossibility of exponential Wannier functions in Chern insulators

As discussed in Section 2.1.2 Wannier functions are not unique, but may vary in shape and spread depending on the choice of gauge freedom in the phases of the underlying Bloch states. By choosing the gauge to minimize localization length (according to some metric), Wannier functions can be chosen for most systems to decay exponentially or faster. However, Wannier functions must decay slower than exponentially in systems with non-zero Chern number. In this section we briefly review results of this nature and their implications.

In Reference 82, Thouless shows that bands hosting a non-zero Hall current do not support exponentially localized Wannier functions forming a representation of the magnetic translation group. The main argument stems from writing the Bloch states in terms of Wannier functions, as in Equation (2.2), and computing the Berry curvature given in Equation (1.15). The integral of the Berry curvature can be shown to vanish if the Bloch states $|\psi_{\mathbf{k}}\rangle$ are analytic and single-valued, which for exponentially localized Wannier functions can be shown to be the case using results akin to the Payley-Weiner theorem. The integral of the Berry curvature is proportional to the Hall conductance, by the Kubo formula in Equation (1.16). Therefore bands which support exponentially localized Wannier functions have identically zero Hall conductance.

This result was later strengthened by removing the requirement that the set of localized functions form a representation of the magnetic translation group. In fact, given any set of localized states within a magnetic band of non-zero Hall conductance, it was shown that completeness, orthogonality, and exponential decay were mutually incompatible [83, 84]. The

impossibility of exponentially localized Wannier functions was also shown for the non-trivial phase of the Haldane model described in Section 1.1.3, a system with zero net magnetic field [85].

Monaco et al. unify the above results in Reference 86, showing that for a system comprising n filled gapped bands there exists a system of composite Wannier functions $|\phi_{\alpha,\mathbf{R}}\rangle$, where the index α labels the band, satisfying

$$\sum_{\alpha=1}^{n} \int_{\mathbb{R}^2} r^2 |\langle \mathbf{r}|\phi_{\alpha,\mathbf{0}}\rangle|^2 \mathrm{d}^2\mathbf{r} < \infty, \tag{2.4}$$

if and only if a gapped set of n bands is topologically trivial, i.e., if and only if the bands have Chern number zero. Conversely, if a gapped quantum system has non-zero Chern number, the sum of the second moments for any set of Wannier functions diverges. Furthermore they show that in 2D systems with non-zero Chern number, the *optimal decay* of Wannier functions $\langle \mathbf{r}|\phi_{\mathbf{R}}\rangle$ is power-law decay of degree 2, i.e.,

$$|\langle \mathbf{r}|\phi_{\mathbf{R}}\rangle| \simeq r^{-2}.$$

2.1.5 Discussion

The results above serve as important motivation for our work in Chapter 3. We find it useful to view constructing localized Wannier functions as the choice of some orthonormal basis for the occupied Hilbert space. This basis additionally has the property that it forms a representation of the (magnetic) translation group. For a system with non-zero Chern number, these restrictions on the basis has the implication that each of the basis elements has diverging second moment.

The remainder of this chapter explores other choices of basis for topological systems appearing in the literature, the corresponding restrictions of each basis, and implications on the degree of localization of states in each basis. In Chapter 3 we explore novel basis selection procedures which identify signatures of the topology of the system.

2.2 Coherent states in the lowest Landau level

2.2.1 Definition and basic properties

Due to the similarities between the algebraic structure of the Hilbert space of the quantum harmonic oscillator and Landau levels, one can import many results about *coherent states* to the setting of the IQHE. Before discussing these results in the LLL, we review some basic definitions and properties of coherent states in the quantum harmonic oscillator.

The coherent states $|\alpha\rangle$ are defined to be the eigenstates of the annihilation operator[1] $a = \frac{1}{\sqrt{2}}(x + ip)$

$$a\,|\alpha\rangle = \alpha\,|\alpha\rangle\,,$$

where the eigenvalue $\alpha \in \mathbb{C}$ is the state label. The coherent state $|\alpha\rangle$ can be expanded in the basis of the energy eigenstates $|n\rangle$ as

$$|\alpha\rangle = \exp\left(-\frac{|\alpha|^2}{2}\right)\sum_{n=0}^{\infty}\frac{\alpha^n}{\sqrt{n!}}\,|n\rangle\,.$$

Additionally, the set of coherent states form a resolution of the identity

$$\mathbb{I} = \frac{1}{\pi}\int_{\mathbb{C}}|\alpha\rangle\,\langle\alpha|\,\mathrm{d}\alpha,$$

which implies that they are complete; in fact they are *over-complete*, as we discuss in Section 2.2.2. The coherent states $\{|\alpha\rangle\}$ are not orthogonal, but rather have overlaps

$$\langle\beta|\alpha\rangle = \exp\left(-\frac{|\alpha|^2 + |\beta|^2 - 2\beta^*\alpha}{2}\right),$$

which decay exponentially with distance in α-space. The coherent states are minimum uncertainty states and saturate the Heisenberg uncertainty relation,

$$\Delta x\Delta p = \frac{1}{2}. \tag{2.5}$$

As discussed in Section 1.1.1, the Landau levels contain two copies of the quantum harmonic oscillator algebra. The first, with annihilation operator a, acts to lower the energy

[1]For simplicity of notation, we work in units where $\hbar = m = \omega = 1$.

of a state to the next lowest Landau level. The second, with annihilation operator b, acts to lower the angular momentum within each Landau level. As a and b commute, one can form mutual coherent states which are eigenstates of both operators [87]. We focus on those states within the lowest Landau level, and so only need to consider the eigenstates $|\beta\rangle$ of the annihilation operator[2] $b = \frac{1}{\sqrt{2}}(X + iY)$,

$$b\,|\beta\rangle = \beta\,|\beta\rangle\,.$$

Most results regarding the coherent states in the quantum harmonic oscillator can be imported directly to the coherent states in the lowest Landau level. Note, however, that the coordinate representations of the states are clearly not the same. Additionally, as can be seen from the definition of the annihilation operators, the role of x and p in the harmonic oscillator are replaced by the center coordinates X and Y respectively. For example, Equation (2.5) imports to a minimum uncertainty relation between the two *spatial* center coordinate operators, hinting at the obstruction to real-space localization within the LLL.

Coherent states in the LLL have the real-space wavefunctions

$$\langle x, y|\beta\rangle = \frac{1}{\sqrt{2\pi}} \exp\left(-\frac{x^2+y^2}{4} + \frac{1}{\sqrt{2}}\beta(x - iy) - \frac{1}{2}|\beta|^2\right),$$

or equivalently after completing the square

$$\langle x, y|\beta\rangle = \frac{1}{\sqrt{2\pi}} \exp\left(-\frac{(x-x_{0,\beta})^2 + (y-y_{0,\beta})^2}{4} + \frac{i}{2}\left(xy_{0,\beta} - yx_{0,\beta}\right)\right), \tag{2.6}$$

where $x_{0,\beta} = \sqrt{2}\,\mathrm{Re}(\beta)$ and $y_{0,\beta} = \sqrt{2}\,\mathrm{Im}(\beta)$. These wavefunctions are Gaussian in amplitude, centered about $(x_{0,\beta}, y_{0,\beta}) = \sqrt{2}(\mathrm{Re}(\beta), \mathrm{Im}(\beta))$, and with a position dependent phase factor.

Using coordinates $z = x - iy$, real-space wavefunctions in the lowest Landau level can be written as $f(z)\exp(-|z|^2/4)$, where $f(z)$ is holomorphic[3] [3]. Liouville's theorem[4] asserts

[2]For simplicity of notation, we also work in units where the magnetic length $l = 1$.

[3]This is a manifestation of the Segal-Bargmann space of analytic functions, originally developed in the context of the harmonic oscillator [88, 89].

[4]Liouville's name is attributed to many theorems within physics and mathematics. Here we refer to the famous result within complex analysis.

that bounded entire functions are constant. It is a direct corollary of these two results that the wavefunction which decays the quickest in all directions is one where $f(z) = 1$ is constant and is a Gaussian centered at the origin. The coherent states we have described above are the magnetic translations of this maximally localized function.

2.2.2 Complete sets of coherent states

The coherent states $|\beta\rangle$ form an over-complete basis for the LLL. This is expected as they are enumerated by the complex numbers, an uncountable set, while the orthogonal basis of angular momentum eigenstates is countable.

In Reference 90, Perelomov quantifies the linear dependence of the coherent states and proves several theorems regarding the degree of completeness of particular sets of coherent states. We reproduce one of these results for our work in Chapter 3. Given the set of coherent states

$$\{|\alpha_{mn}\rangle \, | \alpha_{mn} = m\omega_1 + n\omega_2, m, n \in \mathbb{Z}\} \tag{2.7}$$

defined on a lattice in the complex plane where $\mathrm{Im}\,(\omega_1/\omega_2) \neq 0$ with unit cell area S, then this set is incomplete by a countably infinite number of states if $S > \pi$, is supercomplete by a countably infinite number of states if $S < \pi$, and is complete if $S = \pi$ and remains complete if any one state is removed but becomes incomplete if any two states are removed [90].

It is natural to attempt to use a lattice of coherent states which is complete, i.e. Equation (2.7) with unit cell area $S = \pi$, to form an orthogonal basis of wavefunctions with small mutual uncertainty of conjugate operators. In Reference 91, numerical symmetric orthogonalization (see Appendix 2.A for details on symmetric orthogonalization) of such a lattice of coherent states in the quantum harmonic oscillator is performed. It is numerically shown that the average values of x and p do not change under orthogonalization, but the average values of x^2 and p^2 are found to numerically increase. In Reference 92, the numerical symmetric orthogonalization of such a complete basis of coherent states in the LLL was performed. The resulting states were shown to have very large overlaps with the original Gaussian states within a short radius of the center. Outside this radius, the resulting states

crossover to oscillating power-law decay with exponent r^{-2} [92]. A consequence of this is that the second spatial moments of the resulting states diverge. These may be thought of as representative magnetic Wannier functions for the LLL, where the power-law decay at large r is consistent with the non-zero Hall conductivity and the topology-localization dichotomy [82, 86].

2.3 Disorder and the plateaux transition

Clean crystalline models of matter are attractive and often employed in theoretical calculations as they are analytically amenable. However the introduction of disorder, by impurities and crystalline defects, is an inevitable reality in real materials. In this section we provide an overview of the consequences of disorder in 2D insulators, taking particular note of the disordered Landau level. For more depth, we refer the reader to the review articles by Lee and Ramakrishnan [93] and Kramer and MacKinnon [94].

In Reference 95, Anderson introduced the connection between diffusion and the localization of energy eigenstates, and posited that strong disorder was sufficient to localize all eigenstates in any dimension d. Early investigations of this include work probing statistical properties of the disordered Green's function [96] and using self-consistent perturbation theory to approximate the localized eigenstates [97]. The 'gang of four' later introduced their *scaling theory of localization* [98], which investigates how the conductance of a system scales with the system size, and predicts that *any* finite disorder strength is sufficient to localize all eigenstates in $d = 1$ and 2.

The observation of the integer quantum Hall effect contradicts the claim that all eigenstates are localized by weak disorder in $d = 2$. Additionally, Laughlin's thought experiment argues for the existence of extended eigenstates in a strong magnetic field, independent of the microscopic potential [8, 9]. The above mentioned scaling theory was modified to a two-parameter theory, for the diagonal and off diagonal components of the conductivity tensor, which recovers the non-zero Hall conductance [99–101].

When disorder is introduced into a Landau level, the degeneracy is broken, broadening the spectrum of the Landau level. As one approaches the center E_0 of this broadened spectrum from either side, for example by tuning magnetic field to control the Fermi energy, the localization lengths $\xi(E)$ exhibit the singular behavior

$$\xi(E) = |E - E_0|^{-\nu}.$$

The transition across E_0 is a prototypical example of a quantum phase transition[5]. As localized states do not contribute to the Hall conductivity, it is precisely the states at the band center E_0 which are responsible for the Hall effect. The transition between various IQHE plateaux therefore occur at these E_0. For this reason, this quantum phase transition is often referred to as the *plateau transition*.

There are countless experimental and computational studies which investigate the nature of this phase transition and the value of the localization length exponent ν, thought to be universal. There are also a number of analytical treatments, primarily semiclassical or field theoretic in nature. We present some of the more often cited results in Table 2.1.

Authors	Year	Type	ν
Wei et al. [103]	1988	Experiment	2.38
Mil'nikov & Sokolov [104]	1988	Theoretical	7/3
Chalker & Coddington [105]	1988	Computational	2.5
Huckestien et al. [106]	1992	Computational	2.35
Huo & Bhatt [107]	1992	Computational	2.4
Fogler et al. [108]	1998	Theoretical	5/2
Slevin & Ohtsuki [109]	2009	Computational	2.59
Li et al. [110]	2009	Experiment	2.38
Zhu et al. [111]	2019	Computational	2.48

Table 2.1: An abridged sample of the studies probing the value of the localization length exponent ν for the plateau transition. (Table adapted with permission from a collection of results gathered by Spenser Talkington.)

[5]We refer the reader to the review article by Sondhi et al. [102] for more depth on quantum phase transitions.

2.4 Finite size scaling

Experimental and numerical studies of critical phenomena, such as the plateaux transition discussed in Section 2.3, are subject finite size effects. As one approaches a critical point in the thermodynamic limit, the universal power-law divergences of certain quantities, such as the correlation length, is expected. However, in studies of finite systems these divergences are modified as the correlation length may not exceed the system size. Using data from multiple finite system sizes to extract the universal behavior in the thermodynamic limit is known as the theory of finite size scaling.

The theory of finite size scaling was introduced in the context of critical phenomena within films of finite thickness by Fisher and Barber in Reference 112. For a more developed perspective, including the field theoretic justification for the finite size scaling ansatz, we refer the interested reader to the book by Privman [113]. In this section, we review the motivation, techniques, and aspects of the theory which we use in Chapter 3. Portions of this section follow the treatment in the book by Newmann and Barkema [114].

2.4.1 Finite size scaling ansatz

We begin by considering a system parameterized by some dimensionless parameter ρ, which undergoes a critical transition at $\rho_c = 0$. Critical phenomena are characterized by a correlation length ξ which diverges as a power-law with exponent ν,

$$\xi_\infty(\rho) \propto |\rho|^{-\nu},$$

in the thermodynamic limit where the size of the system $L \to \infty$. Various other quantities, depending on the system definition, may also exhibit singular behavior near the critical point in the thermodynamic limit. As an example, we take some quantity A which diverges in the thermodynamic limit with some exponent γ,

$$A_\infty(\rho) \propto |\rho|^{-\gamma}.$$

Rearranging these two power-laws, we can write the divergence of A_∞ in terms of ξ_∞

$$A_\infty \propto \xi_\infty^{\gamma/\nu}.$$

Given the limitations of experimental and numerical data, we are not able to access infinite systems and therefore the above power-law divergences are not exactly realized. To extrapolate data from finite size systems to infer critical exponents of infinite systems, we review the finite size scaling ansatz [114]. Consider the data obtained for some ρ in a finite system of linear dimension L. If $\xi_\infty(\rho) \ll L$, then we expect $A_L(\rho) \simeq A_\infty(\rho)$. On the other hand if $L \ll \xi_\infty(\rho)$, we expect the correlation length to get cut-off at the system size $\xi_L(\rho) \simeq L$, and similarly $A_L(\rho) \simeq L^{\gamma/\nu}$. These considerations motivate the *finite size scaling ansatz* for the scaling of singular quantity A as

$$A_L = \xi_\infty^{\gamma/\nu} f(L/\xi_\infty), \tag{2.8}$$

where f is some dimensionless *scaling function* which satisfies

$$f(L/\xi_\infty) \propto \begin{cases} \text{constant} & L \gg \xi_\infty \\ (L/\xi_\infty)^{\gamma/\nu} & \xi_\infty \gg L \end{cases},$$

and smoothly connects these regimes in the intermediate region where $L \sim \xi_\infty(\rho)$. More commonly used is the rescaled function $\tilde{f}(x) = x^{-\gamma} f(x^\nu)$, so that Equation (2.8) may be rewritten explicitly in terms of the parameter ρ,

$$A_L(\rho) = L^{\gamma/\nu} \tilde{f}(L^{1/\nu}\rho). \tag{2.9}$$

2.4.2 Recovery of critical exponents via data collapse

Given some data for a singular quantity $A_L(\rho)$ at various L and ρ, we now discuss how we can use the finite size scaling ansatz in the form of Equation (2.9) to recover the critical exponents γ and ν. We scale our parameters

$$\rho \to \tilde{\rho} = L^{1/\nu}\rho \tag{2.10}$$

and measurements

$$A_L(\rho) \to \tilde{A}_L(\rho) = L^{-\gamma/\nu} A_L(\rho). \tag{2.11}$$

Plotting $\tilde{A}$ against $\tilde{\rho}$ should then result in data across all system sizes L collapsing onto the curve $\tilde{f}$. However, for the collapse to be successful the scaling in Equations (2.10) and (2.11) must use the critical exponents γ and ν. By varying trial exponents and quantifying the degree of data collapse, we can extract the values of the scaling exponents ν and γ.

In this thesis, we use a measure of the quality of data collapse developed in Reference 115, which we review here. We work with a set of measurements $A_{L_j}(\rho_{i_j})$ where $j \in \{1, 2, \ldots, J\}$ indexes a system size $L_j \in \{L_1, L_2, \ldots, L_J\}$ and $i_j \in \{0, 1, 2, \ldots, I_j\}$ indexes the parameter ρ of a particular measurement at system size L_j. For each system size L_j, we numerically construct a function $g_j(L^{1/\nu}\rho)$ which interpolates between the scaled measurements

$$L^{-\gamma/\nu} A_{L_j}(\rho_{i_j})$$

with domain bounded by the set of measurements at L_j, that is

$$L_j^{1/\nu} \min(\{\rho_{i_j}\}) \leq L^{1/\nu}\rho \leq L_j^{1/\nu} \max(\{\rho_{i_j}\}). \tag{2.12}$$

The quality metric $d(\nu, \gamma)$ is then defined as

$$d(\nu, \gamma) = \left[\frac{1}{\mathcal{N}} \sum_{j \neq k} \sum_{i_k, \text{over}} \left| L_k^{-\gamma/\nu} A_{L_k}(\rho_{i_k}) - g_j(L_k^{1/\nu}\rho_{i_k}) \right|^q \right]^{1/q}, \tag{2.13}$$

where the first sum is over pairs distinct system sizes indexed by j and k, the second sum is over i_k for ρ_{i_k} in the domain of g_j defined in Equation 2.12, $\mathcal{N}$ is the total number of terms in the sum, and q is some integer which we take to be $q = 2$ in this thesis. The quality of collapse $d(\nu, \gamma)$ measures the sum of mutual residuals between the scaled data at any two distinct system sizes. Because the scaled parameters $L^{1/\nu}\rho$ for different system sizes need not align, the interpolation functions g_j allow us to approximate the residual.

By minimizing Equation (2.13) with respect to ν and γ, we will attain the scaled data with the minimal mutual residuals, i.e. the best data collapse. In Chapter 3, we use the Nelder-Mead algorithm to minimize d [116]. Using any optimization method, one should be

careful to scan a large region of ν-γ space to ensure the minimum one finds is not a local minimum. Once the critical exponents ν and γ have been estimated through minimization, one determines the uncertainties $\Delta\nu$ and $\Delta\gamma$ by evaluating the inverse of the Hessian $\partial^2 d(\nu, \gamma)$ at the minimum.

We note that other measures of the quality of data collapse have been developed in References 117, 118, and 119, but are qualitatively equivalent and all correspond to estimating mutual residuals between sets of scaled data.

APPENDIX

2.A Symmetric orthogonalization

In this appendix we describe an orthogonalization construction often referred to as symmetric orthogonalization, or Lowdin orthogonalization [120].

Given a set of linearly independent, but not necessarily orthonormal, vectors $\{|\psi_n\rangle\}$, we form the operator S whose matrix elements (indexed by the same set indexing the input vectors $\{|\psi_n\rangle\}$) are given by the overlaps

$$S_{ij} = \langle\psi_i|\psi_j\rangle\,.$$

The operator S is Hermitian and is also known as the Gram matrix of the spanning set $\{|\psi_n\rangle\}$. The eigenvalues of Gram matrices are non-negative by construction. Additionally, because we posited our set $\{|\psi_n\rangle\}$ was linearly independent, one may show that the eigenvalues of S are positive. One may then form the orthogonal set $\{|\psi'_n\rangle\}$ as

$$\left|\psi'_j\right\rangle = \sum_i S_{ij}^{-1/2}\,|\psi_i\rangle\,.$$

As opposed to iterative methods, such as Gram-Schmidt orthogonalization, the symmetric orthogonalization treats each input vector on equal footing. In fact it can be shown that when using the symmetric orthogonalization the resulting functions $\left|\psi'_j\right\rangle$ are closest to the input vectors in a least-squares sense, that is the quantity

$$\sum_n ||\,|\psi'_n\rangle - |\psi_n\rangle\,||^2$$

is minimized [121, 122].

CHAPTER 3

Numerical localization signatures of topology in two dimensional insulators

---

Portions of this chapter are adapted from the publication:

Reiss, D., Harper, F., and Roy, R. *Numerical localization signatures of topology in two dimensional insulators.* (In preparation, 2020).

3.1 Motivation

The introduction of strong random disorder to topological 2D systems, such as a Landau level of the IQHE, fails to completely localize the energy eigenstates of a system. Rather a delocalization transition is observed as the Fermi energy approaches the center of the band E_0. The localization length $\xi(E_F)$ scales as

$$\xi(E_F) \propto |E_F - E_0|^{-\nu},$$

where the correlation length exponent ν has been studied numerically and experimentally by many groups and is generally agreed to be approximately $\nu \simeq 2.3 - 2.5$; see our overview in Section 2.3 for more details. For the purpose of simplicity, we take $E_0 = 0$ in our discussion.

The introduction of disorder into a system removes all degeneracy and selects an orthogonal basis for the Hilbert space. This basis is unlike its clean counterpart. Any clean translationally invariant system has energy eigenstates corresponding to delocalized Bloch states, while

the energy eigenstates of the disordered system have varying degrees of localization. The orthogonal basis of energy eigenstates induced from disorder also distinguishes itself from any orthogonal basis which forms a representation of a translation or magnetic translation group, which are also completely delocalized; see our overview of the necessary delocalization of Wannier functions in Section 2.1.2 for more details.

If at some spatial point $\mathbf{r}$ the magnitude of the disorder potential is relatively large, creating a deep well or spike in the potential landscape, we may expect one or several localized energy eigenstates to be centered near $\mathbf{r}$. We suggest a potential effective mechanism for the delocalization transition, noting that although we show later in this chapter that this approach does not reproduce the plateau transition, it does reveal other interesting structure within these systems. We consider that these deepest wells and spikes, uniformly distributed in real space, may 'select' localized states from the Hilbert space independent of other local details. If we project out these 'selected' degrees of freedom from the Hilbert space, we expect to be left with an effective disordered system. Within this effective disordered system, we expect the shortest length scales to have increased and the largest energy scales to have decreased. We imagine repeating this process ad infinitum in an attempt to emulate the delocalization transition.

In this chapter we detail various procedures for removing localized degrees of freedom and probing the length scales of the remaining Hilbert space. For each effective system, we define a parameter $\rho \in (0, 1)$ which measures the ratio of states per unit area remaining in our effecitve system to the original system. The original system is represented by $\rho = 1$, and we expect to see a delocalization transition as $\rho \to 0$. Because in the plateau transition the density of states $g(E)$ is roughly constant near $E = 0$, ρ may be considered a proxy for the effective energy scale of the remaining degrees of freedom.

We want to characterize the length scale $\xi(\rho)$ of an effective system in terms of the projection operator P_ρ onto the remaining degrees of freedom. In the plateau transition, $\xi(\rho)$ is defined as the localization length of the next energy eigenstate. Given a localized state $|\psi\rangle$ centered at some position $\mathbf{r}_0$, a measure of its localization length is the second central

moment

$$\xi^2 = \langle\psi| \left(\mathbf{r} - \mathbf{r}_0\right)^2 |\psi\rangle .$$

Assuming that $|\psi\rangle$ has the shortest localization length of any state supported by P_ρ[1], we define

$$\xi^2(\rho) = \min_{\mathbf{r_0}} \sum_{\mathbf{\Delta r}} \frac{|\Delta\mathbf{r}|^2 |\langle \mathbf{r}_0 + \Delta\mathbf{r}| P_\rho |\mathbf{r}_0\rangle|^2}{\left\| P_\rho |\mathbf{r}_0\rangle \right\|^2}. \tag{3.1}$$

We note that in the case of a multi-band model, Equation (3.1) needs to be modified to include minimization of local rotations of onsite orbitals, that is

$$\xi^2 = \min_{\mathbf{r_0}, U} \sum_{\mathbf{\Delta r}, \mathbf{n}} \frac{|\Delta\mathbf{r}|^2 |\langle \mathbf{r}_0 + \Delta\mathbf{r}, n| P_\rho \left(U |\mathbf{r}_0, n\rangle\right)|^2}{\left\| P_\rho |\mathbf{r}_0\rangle \right\|^2},$$

where n is the orbital index and U is a unitary operator which only mixes the onsite occupied orbitals.

Another equivalent formulation of Equation (3.1) involves defining an operator $D_{\mathbf{r}_0}$ which is the projected distance squared operator from $\mathbf{r}_0$ as

$$D_{\mathbf{r}_0} = P_\rho (\mathbf{r} - \mathbf{r_0})^2 P_\rho.$$

Then, we can define the maximally localized state centered at $\mathbf{r}_0$ to be the eigenstate $|\psi_{\mathbf{r}_0}\rangle$ with the minimum non-zero eigenvalue $\xi^2_{\mathbf{r}_0}$,

$$D_{\mathbf{r}_0} |\psi_{\mathbf{r}_0}\rangle = \xi^2_{\mathbf{r}_0} |\psi_{\mathbf{r}_0}\rangle .$$

By minimizing $\xi_{\mathbf{r}_0}$ with respect to $\mathbf{r}_0$ globally, we can determine the shortest localization length ξ and corresponding state $|\psi\rangle$.

In the remainder of this chapter, we detail three procedures for the elimination of local degrees of freedom and present numerical results in the LLL and at various parameters of the Haldane honeycomb model. In the first procedure, we will consider a simultaneous removal of an extensive fraction of the Hilbert space by removing states localized at points of a lattice. We show numerically the shortest length scales in the remaining Hilbert space

[1]This assumption is likely inconsistent with the energy eigenstates in the plateau transition, as we will see later this chapter.

diverge with exponent $\nu \simeq 0.5$ across the topological systems we consider; and so this method certainly does not represent an emulation of the plateau transition. With $\nu \simeq 0.5$ in mind, we propose a second procedure which sequentially eliminates states on expanding sublattices, and find that this second procedure also produces $\nu \simeq 0.5$. Lastly, we consider the sequential elimination of individual maximally localized states, and find results similar to the previous procedures. We conclude the chapter with a discussion and propose future directions building upon our work.

3.2 Elimination of lattice of maximally localized states

3.2.1 Procedure

In this section we describe a method for the simultaneous elimination of a extensive fraction of the Hilbert space.

We work in a Hilbert space $\mathcal{H}$ for a system of gapped noninteracting particles characterized by projection operator P, such that each state occupies a real space area A. Consider a lattice $\mathcal{L}_\rho$ of unit cell area A_ρ such that

$$1 - \frac{A}{A_\rho} = \rho,$$

where $A_\rho > A$ so that ρ is valued in the interval $(0, 1)$. Our approach is to choose a set of linearly independent states centered at sites of $\mathcal{L}_\rho$ and project them out of $\mathcal{H}$.

For each lattice site $\mathbf{r_{ij}} \in \mathcal{L}_\rho$, we find the maximally localized state $|\psi_{ij}\rangle$ centered at $\mathbf{r_{ij}}$. In the LLL these are coherent states, as discussed in Section 2.2. In generic systems, we can define the projected distance squared operator D_{ij}^2 as

$$D_{ij}^2 = P(\mathbf{r} - \mathbf{r}_{ij})^2 P, \tag{3.2}$$

and take the state $|\psi_{ij}\rangle$ to be the eigenket of D_{ij} with the smallest non-zero eigenvalue. The expected value of a state $\langle\psi| D_{ij}^2 |\psi\rangle$ is closely related to the Marzari-Vanderbilt localization functional Ω described for the construction of maximally localized Wannier functions in Section 2.1.2 [72].

After selecting these states, we next project out the subspace spanned by $\{|\psi_{ij}\rangle\}$. While this set of localized states are generically linearly independent, they are not orthogonal, so we cannot project them out independently from one another. An approach is to orthogonalize the states by the symmetric orthogonalization procedure described in Appendix 2.A, resulting in an orthogonal set of states $\left|\psi'_{ij}\right\rangle$ of localized states, still centered at the sites of $\mathcal{L}_\rho$. One may then find the projection on the remaining subspace P_ρ by projecting each resulting state independently, that is

$$P_\rho = P - \sum_{ij \in \mathcal{L}_\rho} \left|\psi'_{ij}\right\rangle \left\langle\psi'_{ij}\right|. \tag{3.3}$$

We aim to quantify the characteristic length scale $\xi(\rho)$ of the residual projection operator P_ρ. We know this to diverge $\xi(\rho) \to \infty$ as $\rho \to 0$ in the LLL case [90, 92], and want to quantitatively describe the divergence and study its variation across various systems.

3.2.2 Results

3.2.2.1 LLL

For the remainder of this chapter, when working in the LLL we choose the symmetric gauge. Furthermore, we work in the truncated angular momentum basis $\{|m\rangle\}$ with $m \in \{0, 1, \ldots, \frac{3}{4}R^2\}$, ensuring that states centered on sites near the boundary of our domain are (approximately) supported in our basis [3].

For this procedure, we choose the lattice $\mathcal{L}_\rho$ to be square with lattice vectors aligned with x and y, and such that the origin of the plane is in the center of the home cell of the lattice. One may then explicitly enumerate the lattice sites

$$\mathbf{r}_{ij} = a_\rho \left(\left(i - \frac{1}{2} \right) \hat{x} + \left(j - \frac{1}{2} \right) \hat{y} \right), \tag{3.4}$$

where $a_\rho = \sqrt{2\pi/(1-\rho)}$ is the lattice spacing. We then perform the procedure defined in Section 3.2.1 for various values of ρ on sites within a radius R.

We want to study the most localized degrees of freedom supported in $\mathcal{H}_\rho$. Due to the symmetry in the construction of Section 3.2.1, the most localized degrees of freedom remaining

will have centers offset from the lattice $\mathcal{L}_\rho$. Because of the offset introduced in Equation (3.4), one such state is centered at the origin. Additionally, by considering the spatial dependence of P_ρ near the origin, we minimize any numerical errors associated with the truncated angular momentum basis near the boundary of our domain. We define the state $|\mathbf{0}_\rho\rangle$ to be the maximally localized state centered at the origin, that is the eigenstate of the distance squared operator

$$P_\rho \mathbf{r}^2 P_\rho \, |\mathbf{0}_\rho\rangle = \xi^2 \, |\mathbf{0}_\rho\rangle \,, \tag{3.5}$$

with minimal non-zero eigenvalue ξ^2. The length $\xi(\rho)$ may also be written in the angular momentum basis

$$\xi(\rho) = \sqrt{\sum_m (2m+1) |\langle m|\mathbf{0}_\rho\rangle|^2}. \tag{3.6}$$

We performed the procedure described above for various domain radii R and density parameters ρ. In particular, the domains considered support between $N = 200$ and 6050 states in the original Hilbert space $\mathcal{H}$, which is accomplished by varying the radius of the disc R. For each radius R we perform the procedure at the same values of ρ, selected using a geometric sequence, so that the region near $\rho = 0$ was sampled more densely. The data is represented in Figure 3.1.

As we work in a truncated basis of angular momentum states on a finite disc, Equation (3.6) is strictly bounded from above. Therefore, for a fixed disc radius R in the limit $\rho \to 0$, the saturation of ξ seen in Figure 3.1 is expected. Additionally before saturation, ξ appears to grow as a power law.

To validate our assumption that the shortest localization length of the remaining degrees of freedom is a suitable proxy for the correlation length of P_ρ, we perform an initial check of the finite size scaling ansatz reviewed in Section 2.4.1. We can assume the divergence occurs at the critical point $\rho = 0$. Recall that given the correlation length of a system in the thermodynamic limit $\xi_\infty(\rho)$, one expects the scaling relation

$$\frac{\xi_L(\rho)}{\xi_\infty(\rho)} = f\left(\frac{L}{\xi_\infty(\rho)}\right), \tag{3.7}$$

where L is the linear extent of the system and f is some dimension-less scaling function.

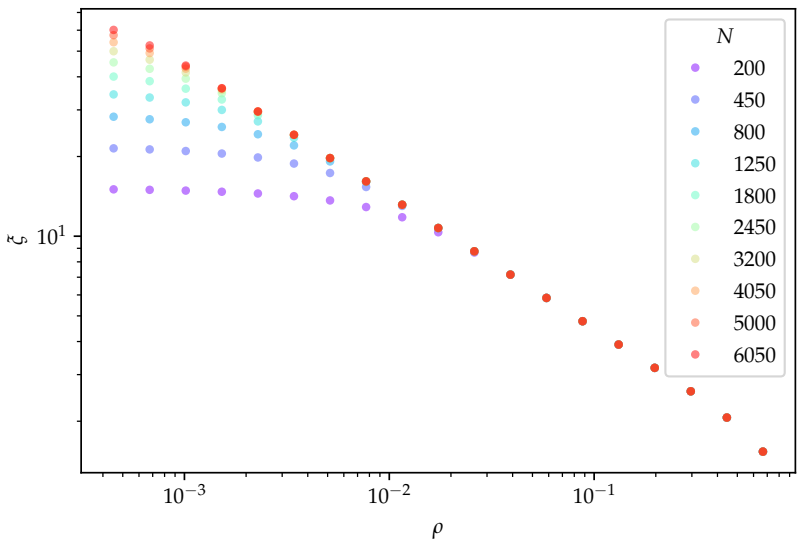

Figure 3.1: Log-log scale plot of $\xi(\rho)$ obtained numerically after the simultaneous elimination of a lattice of localized degrees of freedom as described in Section 3.2.1 in the LLL. The original Hilbert space dimensions N are depicted in different colors. At small ρ and large system sizes, the relationship appears linear suggesting power law behavior in the thermodynamic limit.

In the LLL our domain is a circular disc; we take the linear extent of our system to be $L = \sqrt{N}$, in analog with rectangular systems. For each ρ, we extract an approximation of ξ_∞ as ξ_L for the largest L data available. After scaling using Equation (3.7), we find that our data at various ρ and L does indeed appear to lie on some curve f, as depicted in Figure 3.2.

With this heuristic justification, we proceed to perform finite size scaling analysis to extract the critical exponent ν characterizing the divergence correlation length ξ_∞ in the thermodynamic limit

$$\xi_\infty(\rho) = \rho^{-\nu}.$$

Recall from our review in Section 2.4.1, by modifying the dimensionless scaling function f of Equation (3.7) as $f(x) \to \tilde{f}(x) = x^{-\nu} f(x^\nu)$, one can rewrite the scaling ansatz for the correlation length

$$\frac{\xi_L(\rho)}{L} = \tilde{f}\left(L^{1/\nu}\rho\right), \tag{3.8}$$

which is now independent of ξ_∞, and has introduced the exponent ν explicitly. The scaling

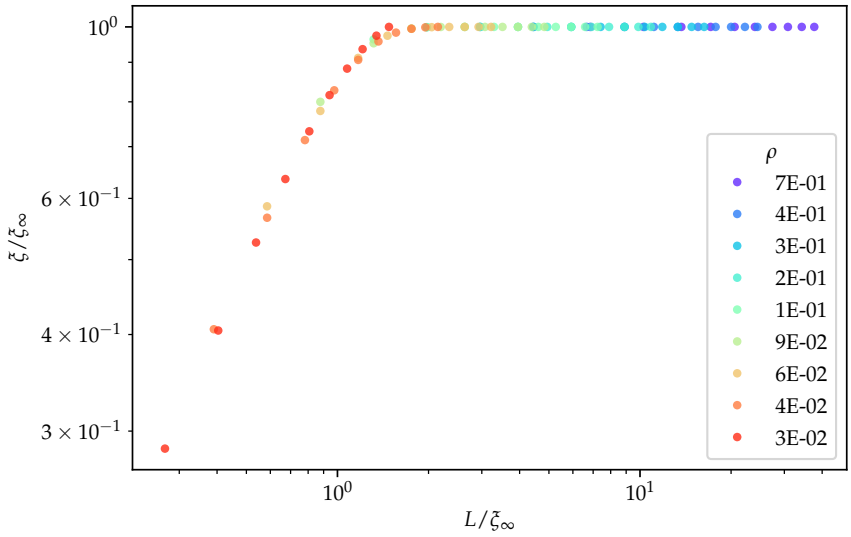

Figure 3.2: Log-log scale plot of the scaled localization lengths $\xi_L(\rho)/\xi_\infty(\rho)$ as a function of the scaled system size $L/\xi_\infty(\rho)$. Different values of ρ are distinguished by color; half of the ρ values have been omitted for clarity. The scaled data appears to fall on a single curve, suggesting that it may be appropriate to treat ξ as the diverging correlation length of P_ρ.

function $\tilde{f}$ should be independent of system size. We therefore can determine ν through optimization of some metric of how well the scaled data collapses onto a single curve as we vary ν.

We perform optimization with respect to ν using a quality metric for data collapse $d(\nu)$, as discussed in Section 2.4.2 [115]. Figure 3.3 depicts the quality of collapse over a range of ν, indicating a global minimum in the vicinity of 0.5. An optimization was performed using the Nelder-Mead descent method determining $\nu = 0.499 \pm 0.005$. Here the uncertainty interval represents the range of ν corresponding to a one percent fluctuation in $d(\nu)$ about its minimum, which can be determined through the numerical evaluation of the second derivative $d''(\nu)$.

Many optimization methods, such as Nelder-Mead, are prone to getting stuck in local minima near some input 'guess' [116]. From the form of the unscaled data in Figure 3.1 for the largest system size $N = 6050$ in the intermediate regime $0 \ll \rho \ll 1$, we expected $\nu \simeq 0.5$.

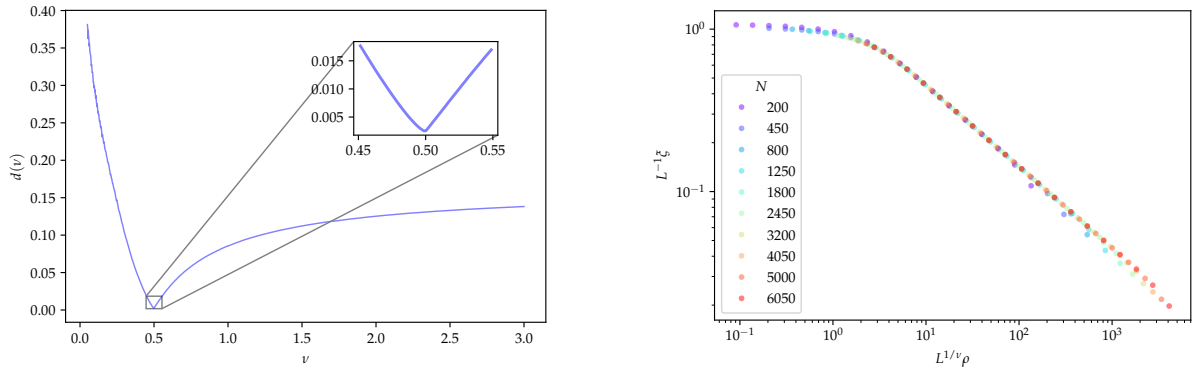

(a) (b)

Figure 3.3: (a) The quality of data collapse $d(\nu)$ as a function of the trial correlation length index ν. For the LLL data depicted in Figure 3.1, optimization of the quality d results in critical exponent $\nu = 0.499 \pm 0.005$. (b) Log-log result of data collapse according to Equation (3.8) using this optimized exponent.

Although our initial scan of $d(\nu)$ in Figure 3.3(a) only reveals one minimum near $\nu \simeq 0.5$, our resolution is finite so we must verify our results. Using the optimal value of ν we explicitly perform the data collapse, shown in Figure 3.3(b). The data clearly collapses onto a single curve, especially when compared to the unscaled data in Figure 3.1, providing a sanity check that the optimization found the appropriate minimum.

3.2.2.2 Haldane honeycomb model

We now shift our focus to the Haldane honeycomb model, aspects of which are discussed in Section 1.1.3.2. The Haldane model is particularly useful because it is defined with a set of parameters for which the topological phase diagram is simple. In particular we can access systems with Chern number $C = 1$ as well as $C = 0$. Therefore we can can probe whether the signature we observed for the LLL is universal across Chern insulators. Additionally we can investigate the response of a trivial insulator.

Furthermore, the Haldane model is a two band model, which reduces the computational cost per unit cell and provides access to larger system sizes. It also enjoys translation

symmetry and easily admits periodic boundary conditions, which is also useful for reducing the computational cost of the elimination procedure detailed in Section 3.2.1.

For the remainder of this chapter, we work with a modified Haldane model with periodic boundary conditions. We have, without loss of generality, modified the lattice to be square with unit spacing and where the orbitals within each unit cell are coincident. We perform numerics at three parameter vectors

$$\mathbf{t}_a = \{t_1 = 1.0, t_2 = 0.1, \phi = \pi/2, M = 0.0\},$$
$$\mathbf{t}_b = \{t_1 = 1.0, t_2 = 0.2, \phi = \pi/2, M = 0.1\},$$
$$\mathbf{t}_c = \{t_1 = 1.0, t_2 = 0.1, \phi = \pi/2, M = 1.0\},$$

where $\mathbf{t}_a$ and $\mathbf{t}_b$ are within the topological phase with $C = 1$, and $\mathbf{t}_c$ is in the trivial phase with $C = 0$. Each of $\mathbf{t}_i$ represent gapped systems, and the projector P corresponds to the lower band.

We denote the lattice underlying the Haldane model by $\mathcal{L}_H$, to avoid ambiguatity with $\mathcal{L}_\rho$. Additionally we take $\mathcal{L}_H$ to be of dimension $L \times L$ and with periodic boundary conditions. As the unit cell area of $\mathcal{L}_H$ is one, we choose $\mathcal{L}_\rho$ to be square of spacing $a_\rho = \sqrt{\frac{1}{1-\rho}}$. Relative to some origin site of $\mathcal{L}_H$, we take the sites of $\mathcal{L}_\rho$ according to Equation (3.4). Due to the periodic boundary conditions, and because $\mathcal{L}_H$ and $\mathcal{L}_\rho$ are incommensurate for generic values of ρ, one has to be careful to consider only the elements of $\mathcal{L}_\rho$ within one copy of $\mathcal{L}_H$. This affects the localization properties of P_ρ near where the boundary conditions are implemented. We will use a method similar to the method used in the LLL to measure $\xi(\rho)$ near the origin site to minimize the influence of these aberrations at the boundary.

To calculate the localization length of remaining degrees of freedom, we define the projected origin state $|\mathbf{0}_\rho\rangle$ as the minimum localization length state centered at the origin site with Equation (3.5). We define the $\mathbf{r}^2$ operator using the *minimum* distance on the torus. Similar to the LLL, we take $\xi(\rho)$ to be the second moment of the projected origin state.

This procedure is quite computationally expensive for tight binding models as we need to compute a number of minimum localization length states to project out. We cannot use

the translation invariance as these states are centered on an incommensurate lattice, and therefore do not form a representation of the translation group. Therefore, we must perform $(1-\rho)N$ exact diagonalizations to find the states we want to eliminate.

We also have to be careful of a scenario where the maximum localization functional at some $\mathbf{r}_{ij}$ in $\mathcal{L}_\rho$ has an approximately degenerate minimum localization length. This can be either a two-fold or four-fold degeneracy which occurs whenever an $\mathbf{r}_{ij}$ is symmetric with respect to an axis of $\mathcal{L}_H$. This approximate degeneracy is especially prominent near $\rho = 0$, as the lattice $\mathcal{L}_\rho$ approaches the periodicity of $\mathcal{L}_H$. We need to break this symmetry to prevent linear dependencies from arising. Within the space of this degeneracy, we choose a representative state which has the smallest overlap with already selected maximally localized states.

We perform the elimination procedure at systems of linear extent L between 12 and 32. We first discuss the $\xi(\rho)$ data at parameters within the topological phase (at $\mathbf{t}_a$ and $\mathbf{t}_b$) which is shown in Figure 3.4.

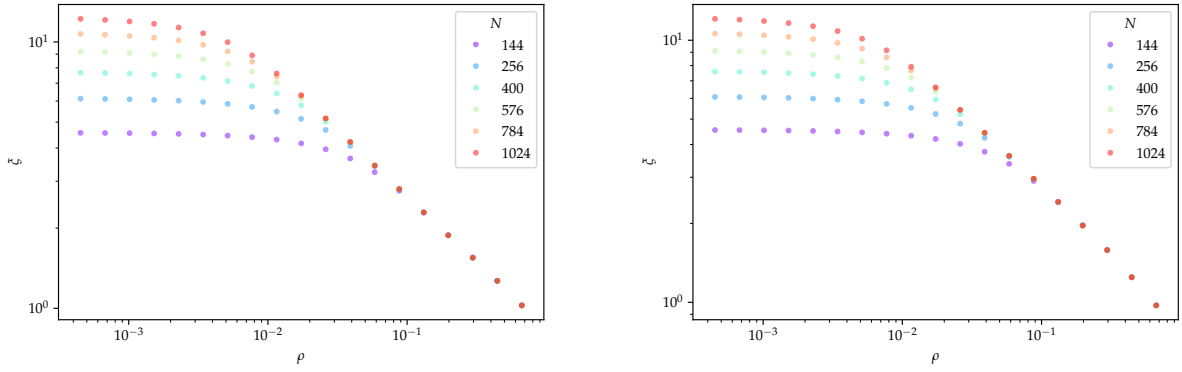

(a) (b)

Figure 3.4: Log-log scale plot of $\xi(\rho)$, achieved numerically after the simultaneous elimination of a lattice of localized degrees of freedom as described in Section 3.2.1 applied to the Haldane model at topological parameters (a) $\mathbf{t}_a$ and (b) $\mathbf{t}_b$.

Within the topological phase of the Haldane model, $\xi(\rho)$ appears to follow a similar scaling behavior to the LLL data in Figure 3.1. We optimize data collapse using the same metric

and optimization methods. We find $\nu = 0.503 \pm 0.011$ and $\nu = 0.499 \pm 0.012$ for parameters $\mathbf{t}_a$ and $\mathbf{t}_b$ respectively. The quality of collapse metric $d(\nu)$ and the collapsed data is depicted in Figure 3.5. A good degree of collapse is attained, and the one percent uncertainty intervals for ν across all the topological systems overlap.

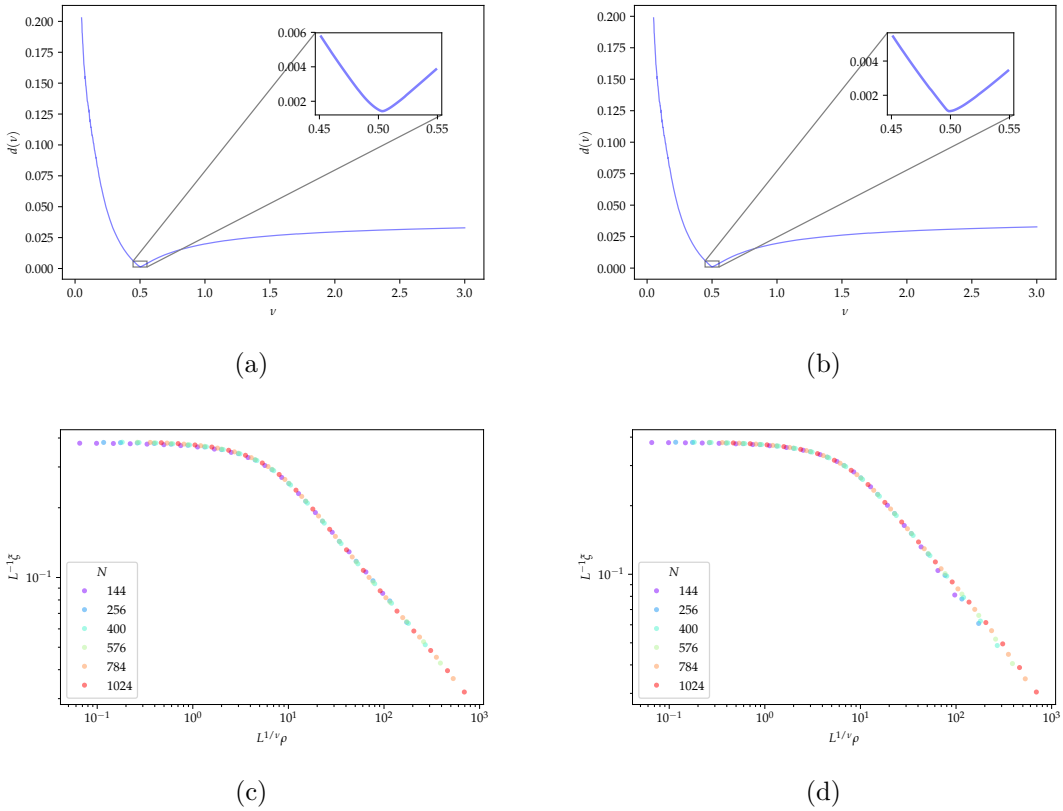

Figure 3.5: The quality of data collapse $d(\nu)$ for systems in the topological Haldane model with parameters (a) $\mathbf{t}_a$ and (b) $\mathbf{t}_b$; optimization of the quality d results in critical exponent of (a) $\nu = 0.503 \pm 0.011$ and (b) $\nu = 0.499 \pm 0.012$. Log-log scale plots of the collapsed data are shown for (c) $\mathbf{t}_a$ and (d) $\mathbf{t}_b$, using the respective optimized exponents.

We now turn our attention to the data $\xi(\rho)$ for the parameters $\mathbf{t}_c$ within the trivial phase of the Haldane model, shown in Figure 3.6. One immediately notices qualitative differences in comparison to the models in the topological phase. In particular, $\xi(\rho)$ appears to be independent of the system size N, indicating the lack of power law scaling.

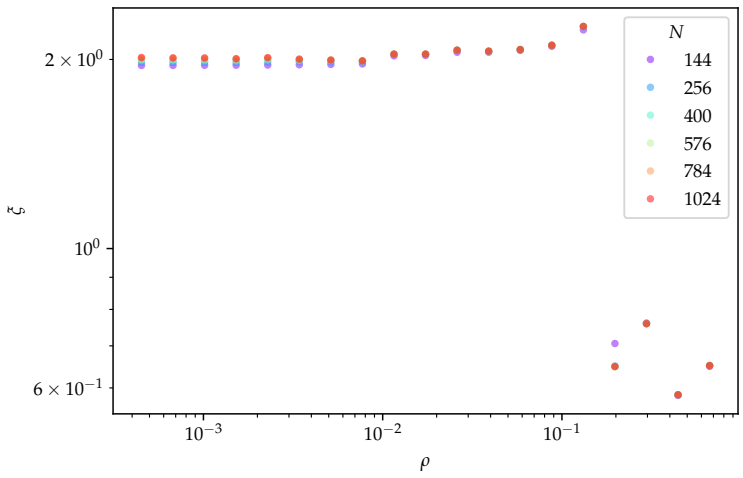

Figure 3.6: Log-log scale plot of $\xi(\rho)$, achieved numerically after the simultaneous elimination of a lattice of localized degrees of freedom as described in Section 3.2.1 applied to the Haldane model at trivial parameters $\mathbf{t}_c$. In the trivial phase we do not see any signatures of power law behavior as $\rho \to 0$, but rather a sudden increase before saturating at $\xi \simeq 2$ independent of system size. The original Hilbert space dimensions N are depicted in different colors, but many system sizes have coincident data and are thus not visible.

3.2.3 Discussion

The critical exponent $\nu \simeq 0.5$ obtained using this procedure appears universal across systems with non-zero Chern number. Although our procedure which naively removes the most localized degrees of freedom does not emulate the plateau transition, it does reveal unexpected real space structure within the projector which may be universal. The exponent $\nu \simeq 0.5$ is significantly smaller than $\nu_{\text{plateau}} \simeq 2.3 - 2.5$, indicating that the shortest length scales in P_ρ are delocalizing "more slowly" compared to the plateau transition. The particular value of $\nu \simeq 0.5$ is especially interesting, and motivates the next elimination procedure we describe in Section 3.3.1.

Systems with zero Chern number do not exhibit a delocalization transition. This means that as $\rho \to 0$, the smallest length scales within the residual projection operator P_ρ do not grow but rather saturate to some L independent constant. This is expected and consistent

with the fact that topological trivial systems support an orthogonal basis of exponentially localized Wannier functions. As $\rho \to 0$, the degrees of freedom we eliminate converge to these Wannier functions.

3.3 Sequential elimination of expanding sublattices of maximally localized states

In this section we provide an alternative procedure for eliminating localized degrees of freedom, based on iterative removal of localized states centered on expanding sublattices. It is not obvious that the correlation length exponent ν for the localization length ξ for bases selected using this procedure should agree with that found using the procedure described in Section 3.2.1. We numerically find they in fact appear to agree. The symmetry of the following procedure also lends itself to physical motivation for the value of the exponent $\nu \simeq 0.5$ as discussed previously.

3.3.1 Procedure

We introduce a square lattice $\mathcal{L}$ of lattice spacing $a = \sqrt{A}$ where A is the real space area occupied per state. In the case of the tight binding model, we simply take $\mathcal{L}$ to be the lattice in the real space definition of the model. In the continuum LLL, we introduce $\mathcal{L}$ such that the origin of the lattice lies at the origin of the plane.

We introduce a decomposition of the lattice (less the origin)

$$\mathcal{L} = \bigoplus_{n=0} \mathcal{L}_n.$$

Each subsequent sublattice in the decomposition $\mathcal{L}_n$ has growing lattice spacing $a_n = a \times \sqrt{2^{n+1}}$, and is translated and rotated such that it is disjoint from the other sublattices and the origin. The sublattices $\mathcal{L}_n$ are illustrated in Figure 3.7.

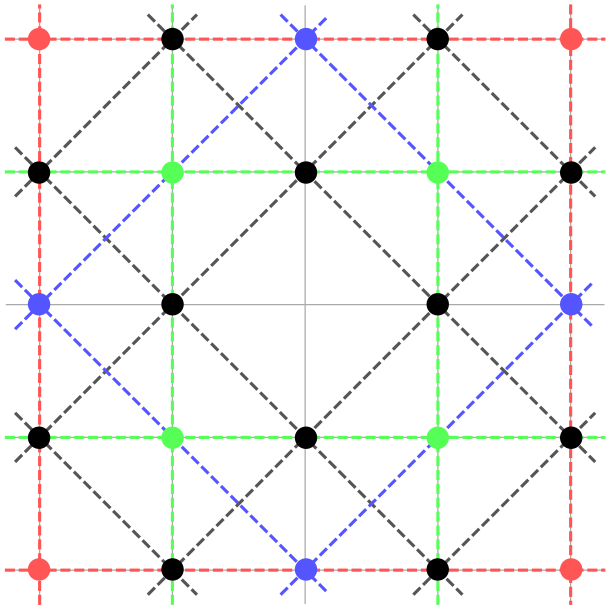

Figure 3.7: An illustration of the decomposition of the underlying lattice (less the origin) $\mathcal{L} = \bigoplus_{n=0} \mathcal{L}_n$, centered at the origin. $\mathcal{L}_0$, $\mathcal{L}_1$, $\mathcal{L}_2$, and $\mathcal{L}_\ni$ are depicted in black, green, blue and red, respectively. Each subsequent sublattice $\mathcal{L}_i$ has growing lattice constant $a_n = \sqrt{2}a_{n-1}$ and is rotated by $\frac{\pi}{4}$ with respect to the previous sublattice.

Our construction decomposes $\mathcal{H}$ as a direct sum

$$\mathcal{H} = \bigoplus_{n=0} \mathcal{H}_n, \tag{3.9}$$

where each subspace $\mathcal{H}_n$ has a mutually orthogonal basis of states $\left|\psi'_{n,ij}\right\rangle$, and each state is localized in real space about points $\mathbf{r}_{ij}$ in the nth sublattice $\mathcal{L}_n$. Each subsequent Hilbert space is therefore approximately half the dimension of its predecessor, i.e., $\dim(\mathcal{H}_0) \simeq \frac{N}{2}, \dim(\mathcal{H}_1) \simeq \frac{N}{4}$, et cetera. Given a projection operator $P = P_0$ onto the occupied states, we now detail an iterative procedure for finding and eliminating such a basis $\{\left|\psi'_{n,ij}\right\rangle\}$. Beginning with $n = 0$:

1. For each site $\mathbf{r}_{ij}$ in the nth sublattice $\mathcal{L}_n$, define the state $|\psi_{n,ij}\rangle$ as the eigenvector corresponding to the minimum non-zero eigenvalue of the projected distance squared operator $D_{n,ij} = P_n(\mathbf{r} - \mathbf{r}_{ij})^2 P_n$.

2. Perform a symmetric orthogonalization of the states $\{|\psi_{n,ij}\rangle\} \to \{\left|\psi'_{n,ij}\right\rangle\}$ following the procedure in Appendix 2.A.

3. Remove the selected states from the projection operator for the next iteration, that is $P_{n+1} = P_n - \sum \left|\psi'_{n,ij}\right\rangle \left\langle\psi'_{n,ij}\right|$. If the rank of P_{n+1} is not zero, then perform another iteration with $n \to n+1$. Otherwise, we have exhausted $\mathcal{H}$.

After each iteration of removing a sublattice of localized degrees of freedom, we can investigate the remaining localized degrees of freedom. We associate to the projector P_n the density parameter $\rho_n = 2^{-n}$, which represents the fraction of the original Hilbert space dimension supported by P_n.

The origin of $\mathcal{L}$, due to the symmetry of the procedure, presents itself as the most *isolated* lattice point at any given step in the procedure. We therefore expect that from the remaining degrees of freedom, we may construct a maximally localized degree of freedom about the origin[2]. At the nth step we find the eigenstate $|\mathbf{0}_{\rho_n}\rangle$ satisfying

$$P_n \mathbf{r}^2 P_n = \xi^2(\rho_n) \, |\mathbf{0}_{\rho_n}\rangle$$

where, in direct analogy with Section 3.2.1, $\xi^2(\rho_n)$ is the smallest non-zero eigenvalue of the projected distance squared operator.

3.3.2 Results

3.3.2.1 LLL

We choose the lattice $\mathcal{L}$ to be square with lattice vectors aligned with x and y, and such that the origin of the plane is coincident with the origin of the lattice.

We performed the procedure detailed in Section 3.3.1 for various domain radii R. In particular the domains considered support between $N = 450$ and 2450 states. For each

[2]At each step there will be points in the lattice which are equivalent to the origin, and one could choose any of these and find the same localization length. In our case, it's best to select the origin as it will be sheltered somewhat from errors accrued near the boundaries.

initial dimension N we perform iterations until the Hilbert space is exhausted. Using this procedure, each system size can now access only the discrete set of values $\rho_n = 2^{-n}$; a system of dimension N can access up to $n \simeq \log_2(N)$. The length $\xi(\rho)$ for various N is plotted in Figure 3.8 and appears to diverge as a truncated power law as expected.

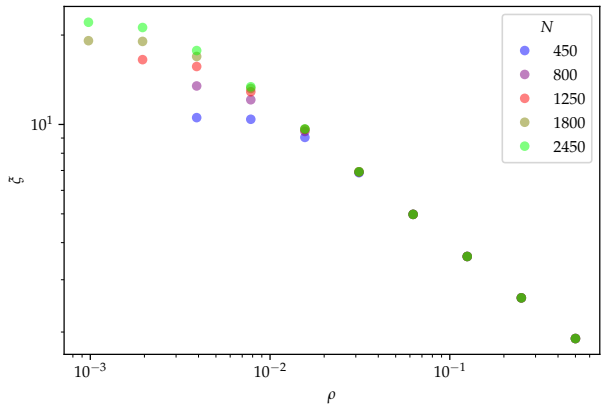

Figure 3.8: Log-log scale plot of $\xi(\rho)$ obtained numerically for the LLL using the sublattice elimination procedure described in Section 3.3.1. The original Hilbert space dimensions N are depicted in different colors.

We again perform optimization of the collapse quality $d(\nu)$ with respect to the correlation length exponent ν. Figure 3.9(a) depicts the quality of collapse over a range of ν, again indicating optimal $\nu \simeq 0.5$. Optimization was performed using the Nelder-Mead descent method determining $\nu = 0.483 \pm 0.039$. The collapsed data is plotted in Figure 3.9(b), which appears to attain a good degree of collapse.

3.3.2.2 Haldane honeycomb model

When applying the sublattice elimination procedure to the Haldane model, we limit ourselves to system sizes $L \times L$, where L is a power of two, in our case $L = 16, 32, 64$ (equivalently, $N = 256, 1024, 4096$). If L is not a power of two, each subsequent sublattice $\mathcal{L}_{n+1}$ in the decomposition will eventually fail to comprise precisely half the states of $\mathcal{L}_n$. Furthermore the symmetry of the origin site will be broken at this point, potentially ruining the validity of our assumption that after any given iteration a maximally localized remaining degree of

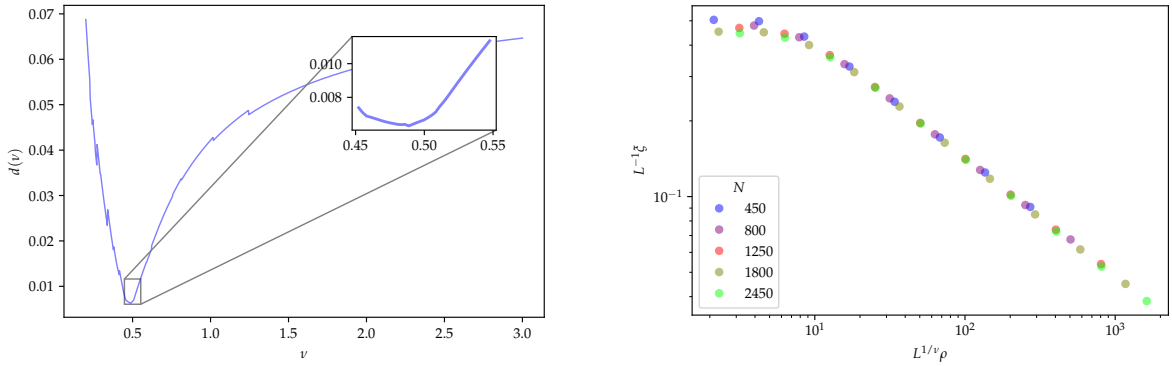

(a) (b)

Figure 3.9: (a) The quality of data collapse $d(\nu)$ for the LLL data depicted in Figure 3.8. Optimization of the quality d results in critical exponent $\nu = 0.483 \pm 0.039$. (b) Log-log plot of data scaled with the optimized exponent.

freedom can be found at the origin.

The $\xi(\rho)$ data for the parameters within the topological phase $\mathbf{t}_a$ and $\mathbf{t}_b$ are shown in Figure 3.10. Again we see that in the topological phase, the localization lengths ξ seem to diverge as a power-law. Optimization of data collapse, depicted in Figure 3.11, results in $\nu = 0.495 \pm 0.010$ for $\mathbf{t}_a$ and $\nu = 0.472 \pm 0.049$ for $\mathbf{t}_b$.

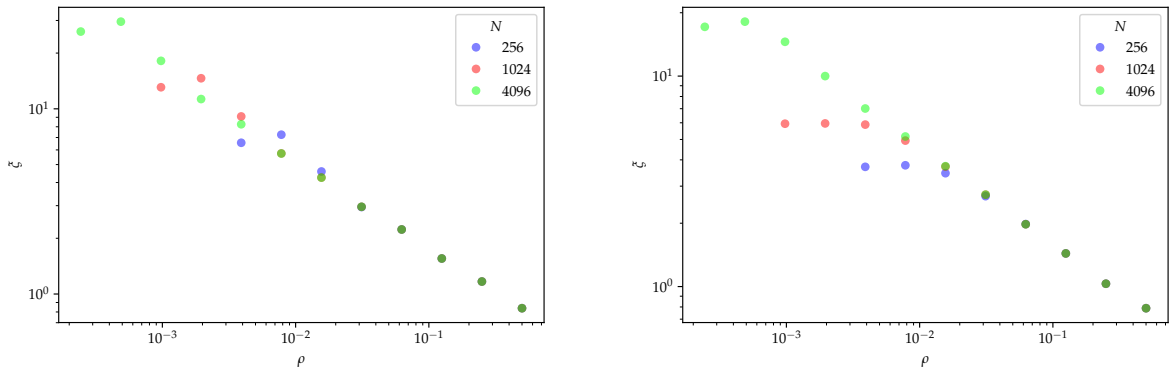

(a) (b)

Figure 3.10: Log-log scale plot of $\xi(\rho)$ obtained numerically through the sublattice elimination procedure described in Section 3.3.1 applied to the Haldane model at topological parameters (a) $\mathbf{t}_a$ and (b) $\mathbf{t}_b$.

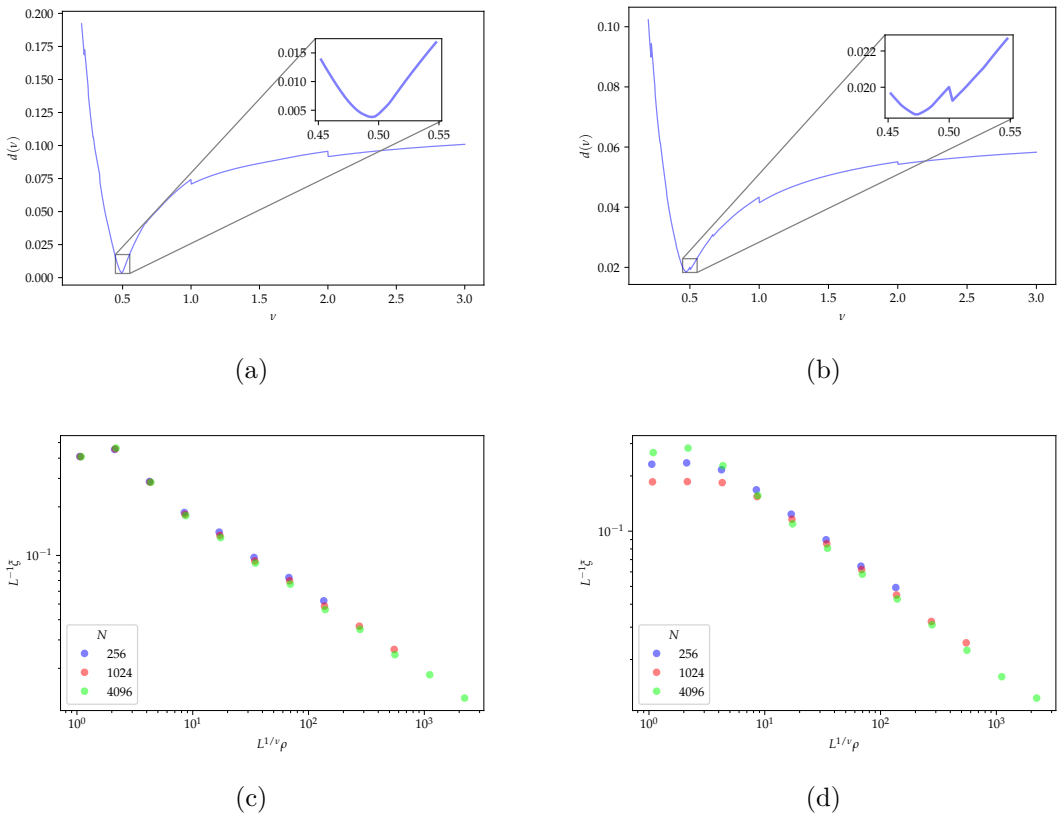

Figure 3.11: The quality of data collapse $d(\nu)$ for data in the topological phase of the Haldane model depicted in Figure 3.10 with parameters (a) $\mathbf{t}_a$ and (b) $\mathbf{t}_b$. Optimization of the quality d results in critical exponent of (a) $\nu = 0.495 \pm 0.010$ and (b) $\nu = 0.472 \pm 0.049$. Log-log scale plots of the collapsed data are shown for (c) $\mathbf{t}_a$ and (d) $\mathbf{t}_b$, using the respective optimized exponents.

The effective localization lengths $\xi(\rho)$ for the Haldane model at $\mathbf{t}_c$ within the trivial phase is shown in Figure 3.12. The length $\xi(\rho)$ very quickly saturates to an N-independent value and does not appear to exhibit a power-law divergence as $\rho \to 0$.

3.3.3 Discussion

The data obtained using this procedure closely resembles that obtained using procedure described in Section 3.2.1. As expected, the trivial system once again shows no singular behavior in ξ. The critical exponents for all topological systems contain $\nu \simeq 0.5$ within their

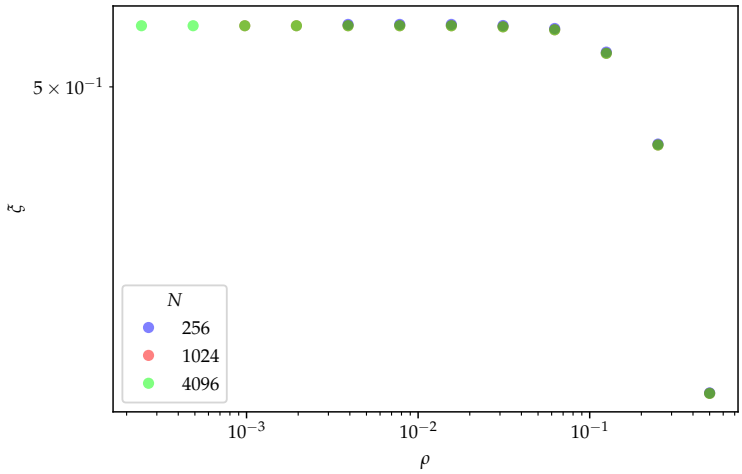

Figure 3.12: A log-log scale plot of $\xi(\rho)$ obtained numerically for the Haldane model at trivial parameters $\mathbf{t}_c$ using the sublattice elimination procedure described in Section 3.3.1. The data for $N = 256$, 1024, and 4096 are essentially coincident, so there appears to be only one set of data.

respective uncertainty intervals.

It is intuitive that the elimination of local states centered on sites of expanding sublattices described in this section should produce the same exponent ν as the simultaneous elimination of states described in Section 3.2.1. Each iteration of this sublattice elimination procedure is equivalent to the simultaneous elimination procedure with $\rho = 1/2$. Each subsequent iteration can be interpreted as performing the simultaneous elimination procedure with $\rho = 1/2$, but replacing the notion 'original/underlying' system after each iteration with the current effective system. For the results for these two methods to be quantitatively consistent, as we observe, the exponent $\nu \simeq 0.5$ must be universal across systems with non-zero Chern number, including intermediate effective systems P_ρ.

The sublattice structure intrinsic to this elimination procedure provides a natural picture of how the localization properties of each effective system evolve as $\rho \to 0$. Recall that in our original system each state occupies a real space area A. When we eliminate a localized degree of freedom centered at some $\mathbf{r}$, we imagine that the effective Hilbert space no longer supports a localized function centered within an area A around $\mathbf{r}$. After removing half of the degrees

of freedom, the distances between potential centers for localized degrees of freedom increase by a factor $\sqrt{2}$, precisely the growth of ξ we observed. This suggests that removing the most localized degrees of freedom *screens* the remaining effective localized degrees of freedom so that their decay is similar to the states of the original system in some scaled coordinates $\mathbf{r} \to \mathbf{r}' = \sqrt{2}\mathbf{r}$. Alternatively stated, the effective system P_ρ in the basis of some scaled real space coordinates $\mathbf{r}'$ is by the measure ξ self-similar to the original system P in the basis of the original coordinates $\mathbf{r}$.

3.4 Sequential elimination of single maximally localized states

In Sections 3.2.1 and 3.3.1 we described methods for eliminating a large fraction of the Hilbert space simultaneously. Numerically we found that in various systems with non-zero Chern number, the localization length $\xi(\rho)$ diverged with exponent $\nu \simeq 0.5$ using both aforementioned procedures. In this section, we present and describe numerical results for a final procedure for the elimination of local degrees of freedom, whereby we only eliminate one state at a time.

3.4.1 Procedure

Similarly to the procedure detailed in Section 3.3.1, we introduce a square lattice $\mathcal{L}$ of lattice spacing $a = \sqrt{A}$ where A is the real space area occupied per state.

Given a projection operator $P = P_0$ onto the space of occupied states (of dimension N), we now detail a procedure to iteratively eliminate the single most localized state. Because we are now eliminating one state at a time, after step n the fraction of remaining states ρ_n is

$$\rho_n = 1 - \frac{n}{N}.$$

Beginning with $n = 0$:

1. For each site $\mathbf{r}_{ij}$ in $\mathcal{L}$, define the state $|\psi_{n,ij}\rangle$ as the eigenvector corresponding to the minimum non-zero eigenvalue $\xi^2_{ij}(\rho_n)$ of the projected distance squared operator

$D_{n,ij} = P_n(\mathbf{r} - \mathbf{r}_{ij})^2 P_n$.

2. Select the state $|\psi_{n,IJ}\rangle$ corresponding to the site with the minimum second moment, that is

$$\xi^2_{IJ}(\rho_n) = \min_{ij} \left\{ \xi^2_{ij}(\rho_n)) \right\}. \tag{3.10}$$

   If there is a degenerate minimum, we can freely choose any such IJ.

3. Remove the selected state from the projection operator for the next iteration, that is $P_{n+1} = P_n - \sum |\psi_{n,IJ}\rangle \langle \psi_{n,IJ}|$. If the rank of P_{n+1} is not zero, then perform another iteration with $n \to n+1$. Otherwise, we have exhausted $\mathcal{H}$.

In contrast to the previous procedures which were symmetric about the origin, this procedure guarantees no symmetry. At each step n, we can associate the minimum second central moment (as defined in Equation (3.10)) $\xi(\rho_n)$ $(= \xi_{IJ}(\rho_n))$ with the density ρ_n.

3.4.2 Results

3.4.2.1 LLL

We performed the procedure detailed in Section 3.4.1 for various circular domains, comprising systems of dimension between $N = 200$ and 900 states. These system sizes are much smaller than the ones used for the procedures discussed in Sections 3.2.1 and 3.3.1. This is because the iterative process of Section 3.4.1 is significantly more computationally expensive.

For each system dimension N, we iteratively eliminate the state with the minimum localization length from the system. It is numerically infeasible to perform this minimization in the space of normalized functions. Instead we introduce a lattice $\mathcal{L}$ of unit cell area 2π of candidate function centers, and find the maximally localized function with respect to each of these centers. We then approximate the global minimum to be the minimum of functions centered on this lattice. The minimal localization lengths $\xi(\rho)$ for various N is plotted in Figure 3.13.

We once again perform optimization of the data collapse quality $d(\nu)$ with respect to the

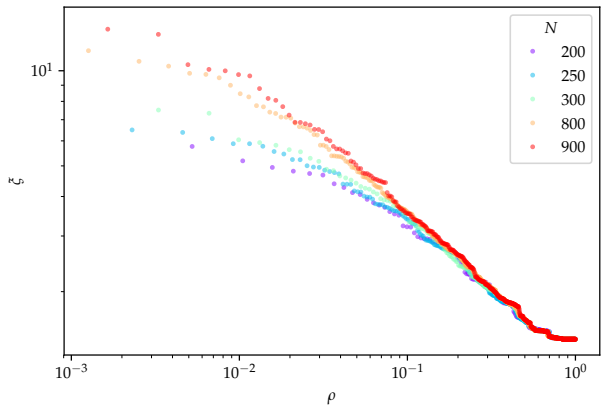

Figure 3.13: Log-log scale plot of $\xi(\rho)$ obtained numerically for the LLL using the sublattice elimination procedure described in Section 3.4.1. The original Hilbert space dimensions N are depicted in different colors.

correlation length exponent ν. Figure 3.14(a) depicts the quality of collapse over a range of ν, again indicating optimal $\nu \simeq 0.5$. Optimization was performed using the Nelder-Mead descent method determining $\nu = 0.487 \pm 0.049$. The collapsed data is plotted in Figure 3.14(b), which appears to attain a good degree of collapse.

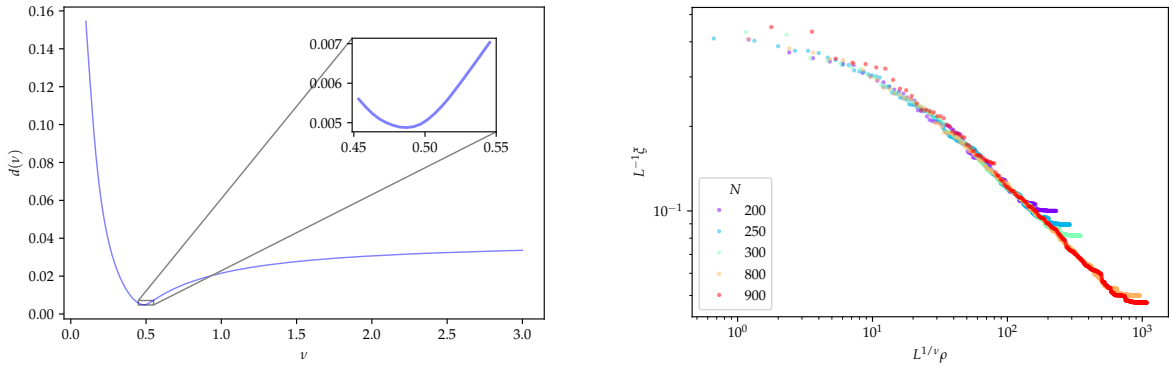

(a) (b)

Figure 3.14: (a) The quality of data collapse $d(\nu)$ for the LLL data depicted in Figure 3.13. Optimization of the quality $d(\nu)$ results in critical exponent $\nu = 0.487 \pm 0.049$. (b) Log-log plot of data scaled with the optimized exponent.

3.4.2.2 Haldane honeycomb model

We have performed the single state elimination procedure detailed in Section 3.4.1 for square systems with periodic boundary conditions, of dimension $N = L \times L$ between $L = 16$ and 30 (or equivalently between $N = 256$ and 900).

The $\xi(\rho)$ data for the parameters within the topological phase $\mathbf{t}_a$ and $\mathbf{t}_b$ are shown in Figure 3.15. Again we see that in the topological phase, the localization lengths ξ seem to diverge as a power-law. Optimization of data collapse, depicted in Figure 3.16, results in $\nu = 0.483 \pm 0.069$ for $\mathbf{t}_a$ and $\nu = 0.478 \pm 0.045$ for $\mathbf{t}_b$.

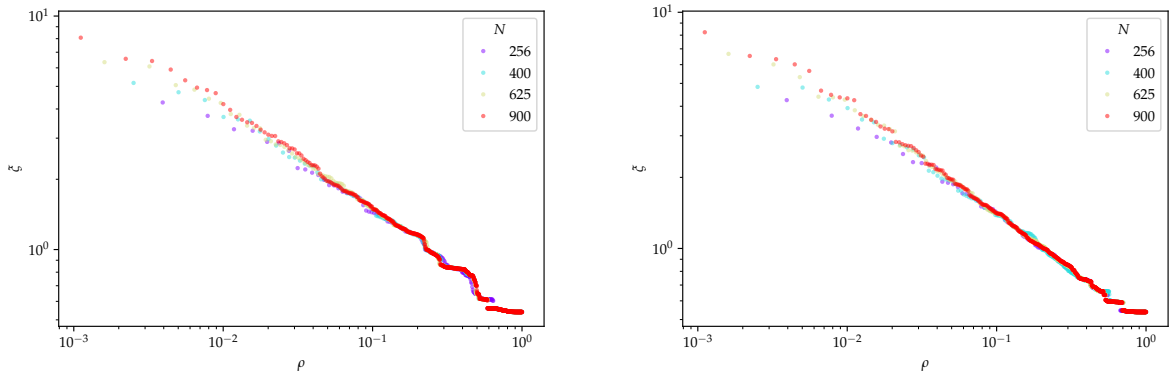

(a) (b)

Figure 3.15: Log-log scale plot of $\xi(\rho)$ obtained numerically through the iterative single state elimination procedure described in Section 3.4.1 applied to the Haldane model at topological parameters (a) $\mathbf{t}_a$ and (b) $\mathbf{t}_b$.

The effective localization lengths $\xi(\rho)$ for the Haldane model at $\mathbf{t}_c$ within the trivial phase is shown in Figure 3.17. Within the trivial phase, $\xi(\rho)$ again very quickly saturates to an N-independent value and, as expected, does not appear to exhibit a power-law divergence as $\rho \to 0$.

3.4.3 Discussion

Once again, the single state removal procedure detailed in Section 3.4.1 results in $\nu \simeq 0.5$ for each topological system we considered. At first glance, this procedure might appear to

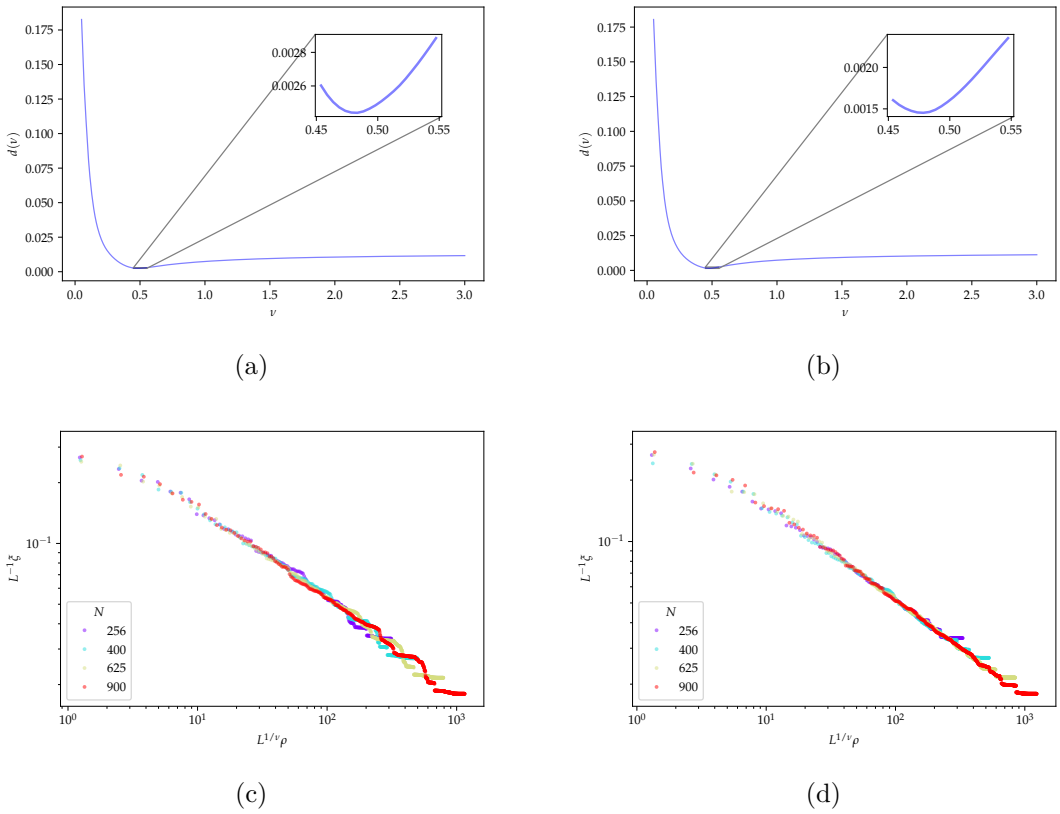

Figure 3.16: The quality of data collapse $d(\nu)$ for data in the topological phase of the Haldane model depicted in Figure 3.15 with parameters (a) $\mathbf{t}_a$ and (b) $\mathbf{t}_b$. Optimization of the quality d results in critical exponent of (a) $\nu = 0.483 \pm 0.069$ and (b) $\nu = 0.478 \pm 0.045$. Log-log scale plots of the collapsed data are shown for (c) $\mathbf{t}_a$ and (d) $\mathbf{t}_b$, using the respective optimized exponents.

be better motivated to emulate the plateau transition, as compared to the more symmetric procedures of Sections 3.2.1 and 3.3.1. However, in the thermodynamic limit it does not make a lot of sense to remove a single state iteratively. If we instead interpret this method as removing a fraction $1/N$ of the maximally localized states, we see that each iteration of this method is equivalent to the simultaneous elimination procedure. It is therefore not surprising that we again find ν consistent with these previous methods.

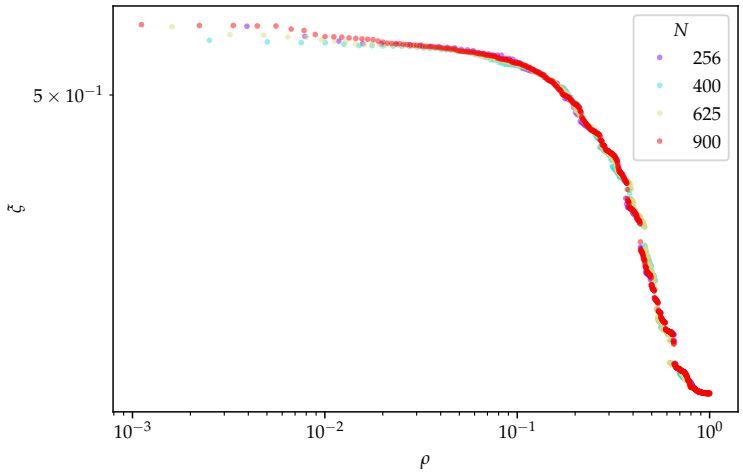

Figure 3.17: A log-log scale plot of $\xi(\rho)$ obtained numerically for the Haldane model at trivial parameters $\mathbf{t}_c$ using the iterative single state elimination procedure described in Section 3.4.1. The data for various system sizes N are essentially coincident and show no semblance of power-law divergence.

3.5 Conclusions and future directions

In this chapter we detailed three procedures for eliminating local degrees of freedom from a system characterized by projection P, providing access to various effective systems with projection P_ρ. Our numeric data suggest, apparently universally across systems with non-zero Chern number, that the shortest length scale $\xi(\rho)$ remaining in P_ρ exhibits the singular behavior as $\rho \to 0$,

$$\xi(\rho) = \rho^{-\nu},$$

with $\nu \simeq 0.5$.

Although our initial motivation to emulate the plateau transition was not achieved, our investigation revealed some non-obvious self-similar structure within the real space representation of the projection operator for Chern insulators. As discussed in Section 3.3.1, if while eliminating local states we simultaneously rescale spatial coordinates so that each remaining state occupies a unit area, the shortest length scales $\xi(\rho)$ can be viewed as a self-similar property of the family of projectors P_ρ.

These constructions are useful for diagnosing the topology of a band numerically, especially in systems where the phase diagram is unknown or the traditional methods for computing the Chern number fail. These methods are spectrum independent, and so they should also succeed in diagnosing topology in disordered systems as long as the disorder is weak enough not to substantially mix bands.

Future investigations may look more closely at the finer structure of the real space matrix elements of P_ρ in the limit $\rho \to 0$, which one could use to better understand why $\nu \simeq 0.5$ and which other metrics of P enjoy this self-similar quality.

Refining these elimination procedures to make better use of symmetry and parallelizing relevant portions of the implementation could allow access to larger system sizes. Further application of these procedures to other Chern insulators, including bands of higher Chern number, may further support the universality of $\nu \simeq 0.5$.

These elimination procedures may potentially be extended to different symmetry classes, for example by imposing symmetry restrictions on eliminated states. Additionally, generalizing these elimination procedures to the many body case could be useful in diagnosing the many-body localized phase.

Finally, it is possible that these procedures can be altered in some way to reproduce the plateau transition. Although we were not successful in this regard, potential modifications include eliminating non-maximal localized degrees of freedom, introducing correlations between centers of eliminated degrees of freedom, or introducing randomness into the procedure. We have begun investigating some of these directions unsuccessfully, but are still optimistic that some modification may be successful.

CHAPTER 4

Background for our work on interacting Floquet topological phases

---

Portions of this chapter are adapted from the publication:

Reiss, D., Harper, F., and Roy, R. *Interacting Floquet topological phases in three dimensions.* Physical Review B **98**, 045127 (2018).

In Section 1.2 we introduced the notion of a Floquet system and showed that some single-particle systems, in particular the Rudner model, exhibit chiral edge modes which can be characterized by a topological invariant associated with its unitary time-evolution operator. In this chapter, we review material which generalizes these ideas to many classes of single and many-particle Floquet systems. This background information will be essential for the succeeding discussion of the classification of three dimensional interacting Floquet toplogical phases in Chapter 5.

4.1 Loop decomposition and homotopy approach

The classification of dynamical systems we will follow in Chapter 5 relies on the homotopy approach introduced in Reference 55. That homotopy approach is concerned with finding topologically distinct paths $U(t)$ within the global space of local unitary evolutions. This framework has the advantage that it disentangles questions about the topology of the path $U(t)$ from questions about the stability of the resulting phase. Interacting Floquet systems,

for example, are believed to be inherently unstable to heating, since energy is pumped into the system with every driving cycle [123–125]. To prevent heating to infinite temperature, strong disorder may be added so that the system becomes many-body localized [126–129] (see Reference 130 for a review of many-body localization). Alternatively, even in the absence of many-body localization, Floquet systems can retain their topological characterization over a (quasi-)exponential prethermal time scale during which heating is negligible[131–133]. In the homotopy approach, the topology of an evolution is well defined independently of these heating effects, which would nevertheless need to be considered in a physical realization of the model, or to formally define a "phase" [55].

The homotopy approach also allows a distinction to be made between static topological order, which depends only on the end point of the unitary evolution $U(T)$, and inherently dynamical topological order, which depends on the complete path of the evolution $U(t)$. As argued in Reference 55, this latter dynamical order can be completely classified by studying a subset of unitary evolutions known as unitary loops which, for a closed system, satisfy

$$U(0) = U(T) = \mathbb{I}.$$

Although unitary loops are somewhat peculiar, non-generic, and do not usually describe physically realistic drives, they are a theoretical tool that can be used to isolate the dynamical part of a drive.

In brief, if a generic unitary evolution $U(t)$ has an endpoint of the form $U(T) = e^{-iH_F}$, where H_F is a well-defined (Floquet) Hamiltonian, then the complete evolution can be expressed as a unitary loop followed by an evolution with the static Hamiltonian H_F. The unitary loop component is responsible for the 'dynamical' order, while the constant evolution component is responsible for the 'static' order. The uniqueness of this decomposition depends on the nature of the Floquet Hamiltonian H_F. We leave a discussion of this subtlety to Reference 55. An explicit method for constructing a unitary loop from an arbitrary many-body localized drive was given in Reference 134, although we emphasize that unitary loops are applicable more generally than this [55].

For our purposes, we restrict our view to the classification of unitary loops which, given the

above decomposition, can capture all inherently dynamical topological evolutions. Specifically, we classify unitary loops by studying their edge behavior, which can be observed when a loop drive is applied to a system with a boundary: In an open system a loop evolution will not necessarily return to the identity at $t = T$, and may instead generate topologically protected edge modes.

Explicitly, we can write a generic closed system Hamiltonian which generates a unitary loop as

$$H_{\text{closed}}(t) = H_{\text{open}}(t) + H_{\text{edge}}(t),$$

where H_{edge} connects sites across a predetermined boundary and H_{open} connects sites away from this boundary. We can then evolve with $H_{\text{open}}(t)$ for a complete cycle to obtain the action of the drive for the open system. However, if the Hamiltonian satisfies some notion of locality, then it will have a corresponding Lieb-Robinson velocity [135]. In turn, this implies that the open system evolution differs from the closed system evolution only in a finite region in the vicinity of the boundary, and so both evolutions must act as the identity deep within the bulk (see Figure 4.1). We can formally restrict the open system evolution to this boundary region, and we refer to this restricted unitary operator as the 'effective edge unitary' U_{eff}. A proof that U_{eff} can always be defined is given in Reference 136.

4.2 Effective unitary operators at a 1D boundary: noninteracting case

Dynamical phases of 2D Floquet systems with no symmetry were classified based on their boundary behavior in References 134, 136, building on a rigorous classification of 1D unitary operators from Reference 67. The aim of Chapter 5 is to obtain a similar classification of 3D Floquet systems by considering the distinct behaviors that may arise at a 2D boundary. To this end, we now briefly review the classification of unitary operators at a 1D boundary, before going on to discuss the 2D case.

As motivated in Section 4.1, dynamical Floquet phases are described by unitary loops,

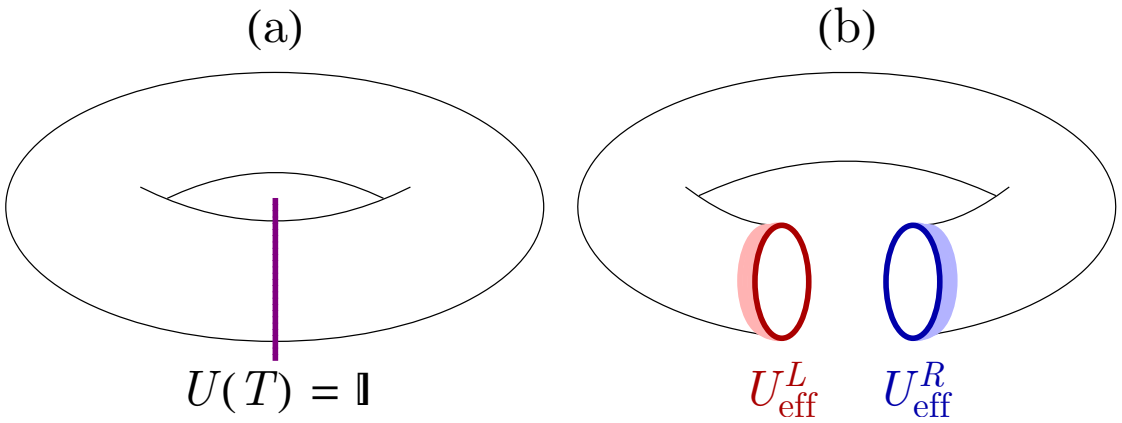

Figure 4.1: Effective edge unitary for a loop evolution applied to an open system. (a) In a closed system, the loop evolution acts like the identity after a complete cycle. The open system Hamiltonian can be formed from the closed system Hamiltonian by removing terms which connect sites across the boundary cut (purple line). (b) The open-system evolution differs only from the identity in a narrow region in the vicinity of the cut, indicated by red and blue shading. The action of the open-system unitary is captured by an effective edge unitary U_{eff} for each boundary. (Figure adapted from Reference 137 with permission from the *American Physical Society*.)

which in turn may be classified by their edge behavior in an open system. For 2D phases, this edge behavior is encapsulated in a 1D unitary operator U_{eff}. Since the underlying Hamiltonian which generates the evolution should be physically motivated, the only restriction on the form of U_{eff} is that it should be *local*—i.e., it should map local operators onto other local operators. For simplicity, we consider local operators to be those expressible as a sum over terms which each act as the identity everywhere except on a region of finite size. We expect that our results may be easily extended to more flexible definitions of locality. There is no requirement, however, that it be possible to generate U_{eff} with a local *one-dimensional* Hamiltonian. This potential anomaly partitions the space of 1D edge behaviors into different equivalence classes.

Our ultimate aim is to classify the equivalence classes of many-body unitaries. However, much of the intuition required for this can be developed in the noninteracting case, which we

review in this section. We consider a 1D lattice $\Gamma = \mathbb{Z}$, whose Hilbert space is spanned by a basis of single-particle on-site occupation states, $\{|i\rangle\}$ with $i \in \mathbb{Z}$. If this is the boundary of a 2D Floquet loop drive, then the effective edge unitary U_{eff} is a local 1D unitary operator. In the language of Reference 67, U_{eff} is a *quantum walk*.

As a motivating example, we consider a unitary operator τ which acts as a unit translation to the right, $\tau |i\rangle = |i+1\rangle$. The operator τ is clearly local, since for a generic local operator $\hat{O}$, conjugation through $\tau \hat{O} \tau^{-1}$ simply translates $\hat{O}$ to the right, yielding another local operator. However, τ cannot be generated in finite time by any local 1D Hamiltonian, and is therefore anomalous [67]. More general unitary operators of this form, known as *shifts*, can be obtained by taking τ^p, where p is an integer.

The authors of Reference 67, building on earlier work by Kitaev [26], form a rigorous classification of quantum walks in 1D, finding that a generic local quantum walk is a shift operator τ^p combined with a locally generated 1D unitary. These form equivalence classes labeled by the integer p describing the shift, with different unitary operators within each equivalence class related by locally generated 1D unitary operators. In this way, the 'pure' shifts τ^p form representative effective edge unitaries which populate all distinct equivalence classes.

The index defining an equivalence class can be interpreted as the net particle flow along the lattice effected by a unitary operator in the class. For example, the shift operator τ^p translates a single particle p sites to the right, and so p is a measure of the charge transported by the drive. For a generic unitary operator, the index p can be extracted directly from the real-space unitary.

Explicitly, the index of a noninteracting one-dimensional unitary U can be calculated as

$$\text{ind } U = \sum_{x \geq 0 > y} \left(\text{Tr} \left(U_{xy}^* \right) U_{xy} - \text{Tr} \left(U_{yx}^* \right) U_{yx} \right) \tag{4.1}$$

where U_{ab} are orbital submatrices of U between lattice sites a and b, and Tr is the ordinary trace [67]. We note that Kitaev [26] provides an equivalent formula and calls this index the *flow* of unitary U.

If the system has translational symmetry, then the integer p is equivalent to the Brillouin zone winding number that describes the wrapping of $U(k)$ around the unit circle as a function of momentum,

$$p = \frac{1}{2\pi i} \int \mathrm{d}k \, \mathrm{tr} \left[U^{-1}(k) \partial_k U(k) \right].$$

An example of a 2D drive that generates this chiral edge behavior was introduced in Reference 40 and reviewed in Section 1.2.2. The effective edge unitary of this system is the shift operator τ we discussed above. Explicit calculation of the index in Equation (4.1) can be performed quickly as we will briefly demonstrate here. The only non-zero elements of the shift operator τ are $\tau_{n+1\,n} = 1$. It is then easy to see that the only non-zero element of the sum in Equation (4.1) is when $x = 0$ and $y = -1$. Therefore we find ind $U = 1$.

As we are considering effective edge unitaries, the unitary operators are by definition local operators. Under this assumption, the following are shown in Reference 67:

- ind U is an integer,
- ind $U = 0$ if and only if U is locally similar to a decoupled unitary, that is if there exists a locally generated unitary V such that the transformed unitary $V^\dagger U V$ has matrix elements $\left(V^\dagger U V\right)_{x_1 x_2} = 0$ if $x_1 \leq 0$ and $x_2 > 0$,
- ind $U_1 =$ ind U_0 if and only if U_0 and U_1 are connected in the space of local unitaries.

The consequences of these properties is that the space of noninteracting local one-dimensional unitaries are partitioned by an equivalence relation parametrized by the the value of ind U. Each equivalence class with ind $U = p$ is locally similar to the shift operator τ^p. This notion of equivalence is protected against any perturbations which are generated by a (potentially time-dependent) local Hamiltonian restricted to the edge of the system. Furthermore, any drive whose bulk behavior is a loop drive will have boundary behavior belonging to one of these equivalence classes. Therefore, all possible equivalence classes can be enumerated by iterating the Rudner drive of Reference 40 discussed in Section 1.2.2 (or it's inverse) $|p|$ times in succession.

4.3 Effective unitary operators at a 1D boundary: many-body case

In the many-body case the underlying Hilbert space is much larger, but the different possible edge behaviors again form distinct equivalence classes characterized by quantized chiral transport. The 1D boundary is still described by a lattice $\Gamma = \mathbb{Z}$, but each lattice site $x \in \Gamma$ is now associated with an (identical) d-dimensional Hilbert space $\mathcal{H}_x$. The entire Hilbert space is the tensor product of all on-site Hilbert spaces,

$$\mathcal{H} = \bigotimes_{x \in \Gamma} \mathcal{H}_x.$$

For concreteness, we can assume each factor $\mathcal{H}_x$ corresponds to a single spin-$(d-1)/2$ particle. As before, a physically reasonable effective edge unitary U_{eff} acting on this Hilbert space should be a local operator, which will now generically involve interactions. In the language of Reference 67, an operator of this form is equivalent to a (quantum) *cellular automaton*.

In Reference 67, 1D cellular automata were classified according to the net flow of quantum information through the system. As in the single-particle case, unitary operators which enact chiral flow are known as *shifts*. However, a many-body shift translates the entire on-site Hilbert space $\mathcal{H}_x$, or more generally a subspace of $\mathcal{H}_x$, for example through

$$\mathcal{H}_{x,1} \otimes \mathcal{H}_{x,2} \longrightarrow \mathcal{H}_{x+1,1} \otimes \mathcal{H}_{x,2}.$$

In this way, a general shift operator may involve a tensor product of Hilbert spaces moving in different directions. As an example of this, Figure 4.2 shows the action of the shift operator $\sigma_3 \otimes \sigma_2^{-1}$, where the factor σ_p indicates the translation of a Hilbert space of dimension p to the right (and the inverse shift σ_p^{-1} to the left). Since the two Hilbert space factors have different dimensions, there is net chiral flow to the right.

Similar to the 1D case, the authors of Reference 67 demonstrate that a generic 1D cellular automaton is a shift operator $\sigma_p \otimes \sigma_q^{-1}$ (with p and q coprime) followed by a locally generated

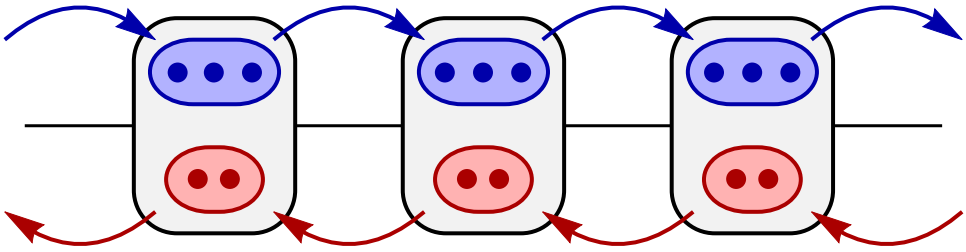

Figure 4.2: The action of the shift operator $\sigma_3 \otimes \sigma_2^{-1}$. The on-site Hilbert space has total dimension six, and may be expressed as the tensor product of a dimension-3 Hilbert space (blue) with a dimension-2 Hilbert space (red) . The unitary acts as a shift to the right on the dimension-3 space but as a shift to the left on the dimension-2 space. This shift is the representative 1D edge unitary in the equivalence class with index $\mathrm{ind}(U) = 3/2$. (Figure adapted from Reference 137 with permission from the *American Physical Society*.)

1D unitary. In particular, adding additional factors to the tensor product or acting with different unitary operators in succession does not modify this general structure [136]. In this way, local many-body unitary operators in 1D form equivalence classes which are each labeled by a rational number p/q, with p and q describing the underlying shift operator. Different unitary operators within the same equivalence classes are related by a locally generated (in 1D) unitary evolution (or more formally, a locally generated unitary circuit of finite depth). The set of 'pure' shifts of the form $\sigma_p \otimes \sigma_q^{-1}$ populate all distinct equivalence classes. In the context of Floquet systems, these equivalence classes correspond to effective edge unitaries with distinct topological invariants.

Reference 67 also demonstrates that the discrete index p/q, which we refer to as the GNVW index, is locally computable for an arbitrary unitary operator, a construction which we now review. First we define a notion of operator overlap. We consider two observable algebras $\mathcal{A}_1$ and $\mathcal{A}_2$ which, for example, could correspond to two spatial regions of a physical system. The matrix units $|e_{ij}\rangle \cong |i\rangle\langle j|$, with $|i\rangle$ and $|j\rangle$ states from the appropriate region,

form a suitable basis for these. A projector onto each algebra can be defined through

$$P_n = d_n \sum_{ij} |e_{ij}\rangle\langle e_{ij}| \,,$$

where d_n is the dimension of $\mathcal{A}_n$. With this setup, we define the overlap measure

$$\eta(\mathcal{A}_1, \mathcal{A}_2) = \sqrt{\mathbf{Tr}(P_1 P_2)},$$

where $\mathbf{Tr}(M) = \frac{1}{d}\mathrm{Tr}(M)$ is the normalised trace over the union algebra $\mathcal{A}_1 \cup \mathcal{A}_2$. In Reference 67 it is demonstrated that the expression $\eta(\mathcal{A}_1, \mathcal{A}_2)$ gives a useful measure of the overlap between algebras $\mathcal{A}_1$ and $\mathcal{A}_2$. In particular, η is always greater than or equal to one, with equality holding only when $\mathcal{A}_1$ and $\mathcal{A}_2$ commute.

The GNVW index uses the quantity η to compare the observable algebras of the 1D boundary system before and after the action of the effective edge unitary. Explicitly, we imagine cutting the (infinite) 1D boundary lattice into left and right halves. We then choose a finite (but large) set of sites immediately to the left and to the right of the cut and denote the Hilbert space corresponding to each as L or R, respectively. We denote the corresponding observable algebras as $\mathcal{A}_L$ and $\mathcal{A}_R$. Now, a unitary operator U acts on a member of an observable algebra through conjugation: i.e., the unitary action α_U on some element M is $\alpha_U(M) = UMU^{-1}$. In this notation, the GNVW index of a unitary operator U is given by the ratio

$$\mathrm{ind}(U) = \frac{\eta(\alpha_U(\mathcal{A}_L), \mathcal{A}_R)}{\eta(\alpha_U(\mathcal{A}_R), \mathcal{A}_L)}. \tag{4.2}$$

In this way, the index compares the extent to which the observable algebra in L is mapped onto the observable algebra in R, and vice versa, by the action of the 1D unitary.

In Reference 67 it is shown that $\mathrm{ind}(U)$ is always a positive rational number, p/q. In addition, the value of the index is independent of the choice of L and R (as long as they are sufficiently large) and independent of the location of the cut within the system. Importantly, $\mathrm{ind}(U)$ is robust against unitary evolutions generated by local 1D Hamiltonians. In this way, $\mathrm{ind}(U)$ is a stable topological index that defines a set of equivalence classes enumerated by positive rational numbers. In contrast to the noninteracting case discussed in Section 4.2,

the index p/q does not have a simple interpretation as the amount of charge (or particle) transport through the system. Instead, the index $\mathrm{ind}(U)$ provides a measure of the quantum information transported, as explored in detail in Reference 138.

It can be verified that the shift operator $\sigma_p \otimes \sigma_q^{-1}$ corresponds to the equivalence class with index $\mathrm{ind}(U) = p/q$. A generic (local) 1D unitary operator can always be brought to a representative shift of this form through the action of a finite-depth quantum circuit (regrouping lattice sites if necessary). In the context of 2D Floquet systems, these representative shift unitaries correspond to the chiral transport of a many-body state around the 1D boundary [134, 136].

CHAPTER 5

Interacting Floquet topological phases in three dimensions

Portions of this chapter are adapted from the publication:

Reiss, D., Harper, F., and Roy, R. *Interacting Floquet topological phases in three dimensions.* Physical Review B **98**, 045127 (2018).

5.1 Overview

A particularly surprising set of Floquet topological phases are those which are robust even in the absence of symmetry [40, 134, 136, 139, 140]. In the presence of interactions, 2D systems in this class have been shown to exhibit robust Hilbert space translation at the boundary of an open system [134, 136], and may be combined with bulk topological order to generate Floquet enriched topological phases [139, 140]. Despite their range of novel features, systems in this class have so far only been studied in 2D; in this chapter, we set out to find and classify the Floquet topological phases that exist in 3D, under the assumption of translational invariance.

Similar to the classification of the related 2D phases, our approach is to first identify the distinct types of boundary behavior that these 3D Floquet systems may exhibit. By invoking ideas from Reference 67, we find that local, translationally invariant unitary operators in two dimensions form distinct equivalence classes with representative 'shift' (or translation)

actions. In turn, this boundary classification partitions the space of 3D unitary evolutions in the bulk into distinct classes. Each class may be labeled by a topological invariant (in this case, an infinite set of reciprocal lattice vectors), with evolutions that are members of the same class being topologically equivalent at a boundary. We construct exactly solvable bulk drives which populate these equivalence classes, and in the process, identify a geometric property of such a drive that determines its anomalous behavior at an arbitrary boundary, a result that also applies to 2D. We conjecture that there are no intrinsically 3D Floquet topological phases (without symmetry), making this classification complete.

The structure of this chapter is as follows: In Section 5.2, we describe and classify local, translationally invariant unitary operators with no symmetry in two dimensions, and show how this classification may be applied to the boundaries of 3D Floquet systems. In Section 5.3, we describe a modification of the exactly solvable 'exchange drives' introduced in References 40, 134, and 136, and show that these have bulk geometric properties directly related to their action at a boundary. In Section 5.4, we extend these models to 3D, and demonstrate that they may be used to generate boundary behavior from all equivalence classes. We summarize and discuss our results in Section 5.5.

5.2 Boundary classifications in 3D

Dynamical phases of 2D Floquet systems with no symmetry were classified based on their boundary behavior in References 134 and 136, building on a rigorous classification of 1D unitary operators from Reference 67. The aim of this chapter is to obtain a similar classification of 3D Floquet systems by considering the distinct behaviors that may arise at a 2D boundary. In Chapter 4 we briefly reviewed the classification of unitary operators at a 1D boundary. Motivated by the lower-dimensional case, our approach is to study the properties of local unitary operators in *two* dimensions, corresponding to the effective edge unitary of a 3D unitary loop. We define a robust topological invariant for this class of unitaries and use it to infer the existence of equivalence classes corresponding to distinct topological phases.

The boundary is now a 2D Bravais lattice, which we take without loss of generality to be square so that $\Gamma = \mathbb{Z}^2$. On each lattice site there is a d-dimensional Hilbert space $\mathcal{H}_{x,y}$, and the complete Hilbert space is the tensor product over these,

$$\mathcal{H} = \bigotimes_{x,y\in\Gamma} \mathcal{H}_{x,y}.$$

As before, we may assume for concreteness that each on-site Hilbert space describes a single spin-$(d-1)/2$ particle. In general, the boundary behavior is described by an effective edge unitary U_{eff} which acts on this Hilbert space and which is local and two dimensional. However, U_{eff} is not necessarily generated by a local 2D Hamiltonian that acts only within the boundary region. In the language of Reference 67, U_{eff} is again a cellular automaton (although we note that this reference only studies cellular automata in 1D).

Without translational invariance, there is a large set of distinct effective edge unitaries that could be constructed—for example, we could stack shift operators σ_p with different p in parallel rows in uncountably many ways. In this paper we restrict the discussion to the manageable translationally invariant case, and leave a more general study to future work.

In order to import some of the results from the 1D case, we will treat the infinite 2D boundary as the limiting case of a sequence of quasi-1D cylindrical systems. First, since U is local, it has some Lieb-Robinson length λ_{LR} [135], and we assume for simplicity that the action of U is strictly zero for separations greater than this length. Then, given a lattice vector $\mathbf{r}$ and sufficiently large integer N such that $|N\mathbf{r}| \gg \lambda_{\text{LR}}$, we define a finite periodic system by identifying all lattice sites that are separated by an integer multiple of $N\mathbf{r}$. This periodic system can be thought of as having a compact dimension along the $\mathbf{r}$-direction with period $N\mathbf{r}$ and an extended dimension along any primitive lattice vector $\mathbf{r}'$ which is linearly independent to $\mathbf{r}$. We denote the restriction of a unitary operator U to this periodic system as $U_{N,\mathbf{r}}$; since U is translationally invariant and local, this restriction is always well defined.

We may now compute the GNVW index for this semi-infinite system by treating it as essentially 1D. Explicitly, we define a cut along $\mathbf{r}$, which divides the system in two halves (L and R) as illustrated in Figure 5.1. The index, $\text{ind}(U_{N,\mathbf{r}}, \mathbf{r})$, associated with this cut can then be calculated by grouping sites in the $\mathbf{r}$-direction into a single 1D 'site' and applying

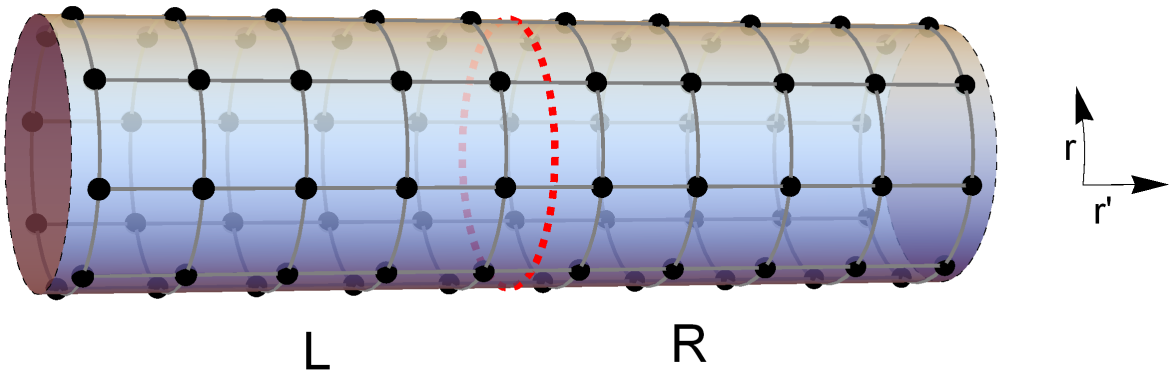

Figure 5.1: Illustration of a choice of cut (red dashed line) which divides a 2D system with a compact dimension along $\mathbf{r}$ into the two halves L and R. By grouping the Hilbert space of N sites along the compact dimension, one may calculate the 1D GNVW index. This index is invariant under translations of the cut by $\mathbf{r}'$. (Figure adapted from Reference 137 with permission from the *American Physical Society*.)

Equation (4.2). Physically, the index gives a measure of the flow of quantum information across the cut in the axial direction of the cylinder.

Due to translational invariance, the index $\mathrm{ind}(U_{N,\mathbf{r}}, \mathbf{r})$ does not depend on the location of the cut. The value of $\mathrm{ind}(U_{N,\mathbf{r}}, \mathbf{r})$ will, however, generally depend on the extent of the compact dimension $N\mathbf{r}$: If this dimension is made larger, then more information can flow across the cut. We therefore define a *scaled* additive index

$$\nu(\mathbf{r}) = \lim_{N\to\infty} \frac{1}{N} \log \mathrm{ind}(U_{N,\mathbf{r}}, \mathbf{r}), \tag{5.1}$$

where the size of the periodic system is increased by taking the limit $N \to \infty$ for a fixed lattice vector $\mathbf{r}$. This limit defines a sequence of periodic cylindrical systems which tends towards the infinite plane. The index $\mathrm{ind}(U_{N,\mathbf{r}}, \mathbf{r})$ should scale as a power of N due to translation invariance, and we consequently expect the scaled index $\nu(\mathbf{r})$ to be finite. We can interpret $\nu(\mathbf{r})$ as a measure of the flow of quantum information across a cut along $\mathbf{r}$ due to the action of the unitary, per length $|\mathbf{r}|$. We note for later use that since $\mathrm{ind}(U_{N,\mathbf{r}}, \mathbf{r})$ is always a rational

number [67], the scaled index can be equivalently written as a sum over primes p,

$$\nu(\mathbf{r}) = \sum_p n_p(\mathbf{r}) \log p, \tag{5.2}$$

with integral coefficients n_p.

In contrast to the 1D case, the flow of quantum information within a 2D boundary depends on the direction of the cut across which it is measured. This is indicated by the fact that the index $\nu(\mathbf{r})$ depends on a lattice vector $\mathbf{r}$. However, due to the properties of unitary evolutions, we would expect different $\nu(\mathbf{r})$ corresponding to different lattice vectors $\mathbf{r}$ to be related. In Section 5.2.1 we show that $\nu(\mathbf{r})$ is a linear function of 2D lattice vectors, satisfying the property

$$\nu(\mathbf{r}_1 + \mathbf{r}_2) = \nu(\mathbf{r}_1) + \nu(\mathbf{r}_2). \tag{5.3}$$

It follows that the coefficients $n_p(\mathbf{r})$ in the sum over primes in Equation (5.2) are integer-valued linear functions of $\mathbf{r}$, and so each may be written as

$$n_p(\mathbf{r}) = \frac{1}{2\pi}\mathbf{G}_p \cdot \mathbf{r}, \tag{5.4}$$

given as the inner product of $\mathbf{r}$ with some reciprocal lattice vector $\mathbf{G}_p$. The reciprocal lattice vectors $\{\mathbf{G}_p\}$ in this way provide a more fundamental description of an effective edge unitary than a value of $\nu(\mathbf{r})$ alone, as they allow the index $\nu(\mathbf{r})$ to be calculated for *any* value of $\mathbf{r}$.

Overall, translationally invariant unitaries in two dimensions are classified by a set of reciprocal lattice vectors $\{\mathbf{G}_p\}$, indexed by primes p. These determine the scaled additive index $\nu(\mathbf{r})$ along any direction $\mathbf{r}$ through Equation (5.2), and consequently quantify the flow of quantum information across any cut in the 2D boundary. Conversely, by 'measuring' $\nu(\mathbf{r})$ for a unitary U along some basis $\{\mathbf{r}_1, \mathbf{r}_2\}$ of the lattice, we can uniquely determine the vectors $\{\mathbf{G}_p\}$ using the relation

$$\mathbf{G}_p = n_p(\mathbf{r_1})\mathbf{b}_1 + n_p(\mathbf{r}_2)\mathbf{b}_2,$$

where $\{\mathbf{b}_1, \mathbf{b}_2\}$ are reciprocal lattice vectors corresponding to $\{\mathbf{r}_1, \mathbf{r}_2\}$ (satisfying $\mathbf{r}_i \cdot \mathbf{b}_j = 2\pi\delta_{ij}$). Since this classification is discrete, it partitions the set of 2D translationally invariant unitaries into discrete equivalence classes.

We can define a representative unitary $V_{\{\mathbf{G}_p\}}$ corresponding to a given set of vectors $\{\mathbf{G}_p\}$ as follows. First, for each value of p with a nonzero reciprocal lattice vector $\mathbf{G}_p$, we define a local Hilbert space with dimension p on each site; the total Hilbert space is the tensor product of these Hilbert spaces over the complete 2D lattice. We then define a translation vector $\mathbf{r}_{\mathrm{tr},p}$ corresponding to each nonzero $\mathbf{G}_p$ through

$$\mathbf{r}_{\mathrm{tr},p} = \frac{1}{2\pi}\left[(\mathbf{r}_1 \times \mathbf{r}_2) \times \mathbf{G}_p\right] \tag{5.5}$$

where it may be verified that $\mathbf{r}_{\mathrm{tr},p}$ lies in the direct lattice with basis $\{\mathbf{r}_1, \mathbf{r}_2\}$.

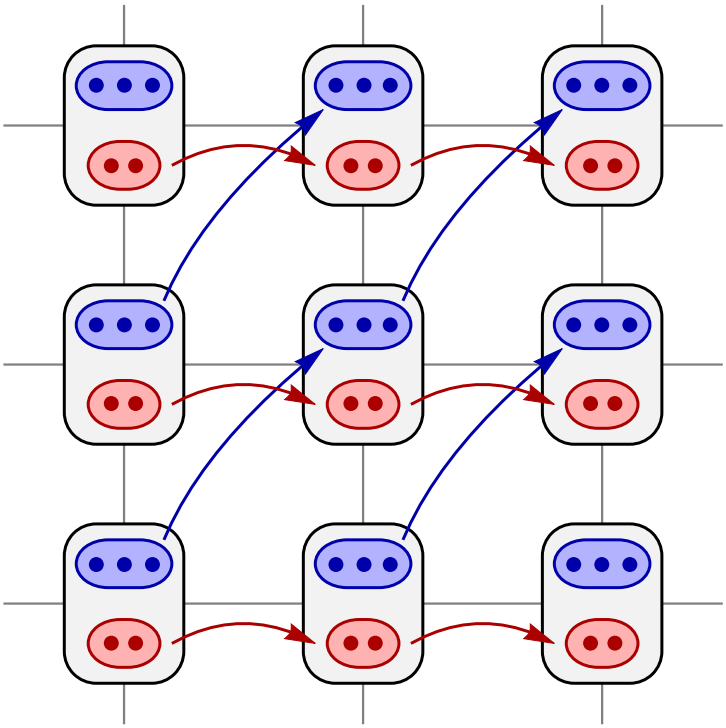

Figure 5.2: The action of the representative unitary in the equivalence class characterized by $\mathbf{G}_2 = -2\pi\hat{\mathbf{y}}$ and $\mathbf{G}_3 = 2\pi\hat{\mathbf{x}} - 2\pi\hat{\mathbf{y}}$, with all other $\mathbf{G}_p = 0$, on a 2D lattice spanned by $\{\mathbf{r}_1 = \hat{\mathbf{x}}, \mathbf{r}_2 = \hat{\mathbf{y}}\}$. The on-site Hilbert space is the tensor product of a dimension-2 factor and a dimension-3 factor. The unitary acts as a shift of the dimension-2 factor by translation vector $\hat{\mathbf{y}}$ and a shift of the dimension-3 factor by translation vector $\hat{\mathbf{x}} + \hat{\mathbf{y}}$. (Figure adapted from Reference 137 with permission from the *American Physical Society*.)

The representative unitary $V_{\{\mathbf{G}_p\}}$ acts independently on each p-dimensional factor of

this Hilbert space as a translation with direction and magnitude $\mathbf{r}_{\mathrm{tr},p}$. In terms of the one-dimensional shift operators defined in Section 4.3, we can write this as

$$V_{\{\mathbf{G}_p\}} = \bigotimes_p \sigma_{\mathbf{r}_{\mathrm{tr},p}},$$

where each shift $\sigma_{\mathbf{r},p}$ now has both a direction $\mathbf{r}$ and a Hilbert space dimension p associated with it, and where the product is taken over all primes p. In this way, the shift for each Hilbert space in the tensor product can have a different magnitude and direction. By expressing a given vector $\mathbf{r}$ in the basis $\{\mathbf{r}_1, \mathbf{r}_2\}$ and exploiting the linearity of $\nu(\mathbf{r})$, it may be verified that this representative unitary $V_{\{\mathbf{G}_p\}}$ generates the expected value of the chiral unitary index $\nu(\mathbf{r})$ for any choice of cut $\mathbf{r}$. An example of a unitary operator with non-zero $\mathbf{G}_2$ and $\mathbf{G}_3$ is illustrated in Figure 5.2.

The set of reciprocal lattice vectors $\{\mathbf{G}_p\}$ characterizing a particular equivalence class of unitaries inherits a group structure under two products within the space of unitaries from the group structure of the GNVW index [67]. Under the sequential action of two unitaries $U_3 = U_2 \circ U_1$, the reciprocal lattice vectors add term-wise, $\{\mathbf{G}_{p,3} = \mathbf{G}_{p,1} + \mathbf{G}_{p,2}\}$. Similarly, if we consider the site-wise tensor product of two systems, with unitary $U_3 = U_1 \otimes U_2$, the reciprocal lattice vectors again add term-wise according to $\{\mathbf{G}_{p,3} = \mathbf{G}_{p,1} + \mathbf{G}_{p,2}\}$. In Section 5.2.2 we show that an arbitrary set of shifts can always be characterized by a set of reciprocal lattice vectors $\{\mathbf{G}_p\}$ with p prime. In Appendix 5.B, we show that edge behavior described by different $\{\mathbf{G}_p\}$ is stable under locally generated (in 2D) unitary deformations at the edge.

5.2.1 Linearity of the scaled additive index

In this section, we study the properties of the index $\nu(\mathbf{r})$ as the direction of the cut $\mathbf{r}$ is varied. We consider a translationally invariant local unitary operator U restricted to a periodic cylindrical system. Specifically, we take three cylindrical systems defined by $(N, \mathbf{r}_1)$, $(N, \mathbf{r}_2)$ and $(N, \mathbf{r}_1 + \mathbf{r}_2)$, and write the action of the unitary restricted to each of these as $U_{N,\mathbf{r}_1}$, $U_{N,\mathbf{r}_2}$ and $U_{N,\mathbf{r}_1+\mathbf{r}_2}$, respectively.

We now construct a fourth system, as shown in Figure 5.3, by cutting the systems $(N, \mathbf{r}_1)$ and $(N, \mathbf{r}_2)$ each along a common extended direction $\mathbf{r}'$ and reconnecting them along this line. The reconnection is carried out by restoring local terms in the unitary such that the final system is compact along the $\mathbf{r}_1 + \mathbf{r}_2$ direction with length $N(\mathbf{r}_1 + \mathbf{r}_2)$. We write the action of the unitary on this composite system as $U'_{N,\mathbf{r}_1+\mathbf{r}_2}$, and note that further than λ_{LR} away from either cut, the action of $U'_{N,\mathbf{r}_1+\mathbf{r}_2}$ is identical to that of $U_{N,\mathbf{r}_1+\mathbf{r}_2}$.

We now argue that both of these unitaries correspond to the same index $\nu(\mathbf{r}_1 + \mathbf{r}_2)$ and further, that $\nu(\mathbf{r}_1 + \mathbf{r}_2) = \nu(\mathbf{r}_1) + \nu(\mathbf{r}_2)$. First, since $U'_{N,\mathbf{r}_1+\mathbf{r}_2}$ and $U_{N,\mathbf{r}_1+\mathbf{r}_2}$ differ (if at all) only in the vicinity of the two horizontal cuts used in defining the system, we must have

$$\mathrm{ind}\left(U_{N,\mathbf{r}_1+\mathbf{r}_2}\right) = \delta \times \mathrm{ind}\left(U'_{N,\mathbf{r}_1+\mathbf{r}_2}\right), \tag{5.6}$$

where δ is the contribution to the index caused by rejoining local terms in the unitary action across the cuts. We discuss the scaling of δ below as N is taken to infinity, and argue that it is negligible in the infinite limit.

We also construct a 1D cell structure for these systems compatible with both a 'triangular' slice along the $\mathbf{r}_1$ direction followed by the $\mathbf{r}_2$ direction, and a 'linear' slice along the $\mathbf{r}_1 + \mathbf{r}_2$ direction, as shown in Figure 5.4. The index $\mathrm{ind}(U)$ computed for a given unitary, from the properties of the GNVW index [67], must be the same for either of these cuts. Choosing the triangular slice, we see that the unitary $U'_{N,\mathbf{r}_1+\mathbf{r}_2}$ acts like either $U_{N,\mathbf{r}_1}$ or $U_{N,\mathbf{r}_2}$ away from the horizontal cuts. Overall, this means that

$$\mathrm{ind}(U_{N,\mathbf{r}_1+\mathbf{r}_2}) = \delta \times \mathrm{ind}(U_{N,\mathbf{r}_1}) \times \mathrm{ind}(U_{N,\mathbf{r_2}}), \tag{5.7}$$

where the δ here may differ from that in Equation (5.6), but will have the same scaling.

In both cases, the multiplicative correction to the index δ, which is introduced when rejoining two periodic systems, is bounded above and below by constants which depend only on the Lieb-Robinson length λ_{LR} of the underlying 2D unitary U, and the on-site Hilbert space dimension d. Explicitly, for any 1D system, the largest possible correction is achieved by a unitary whose action is equivalent to translation of the entire Hilbert space by the Lieb-Robinson length λ_{LR}. The upper bound on δ describes the case where the unitary before

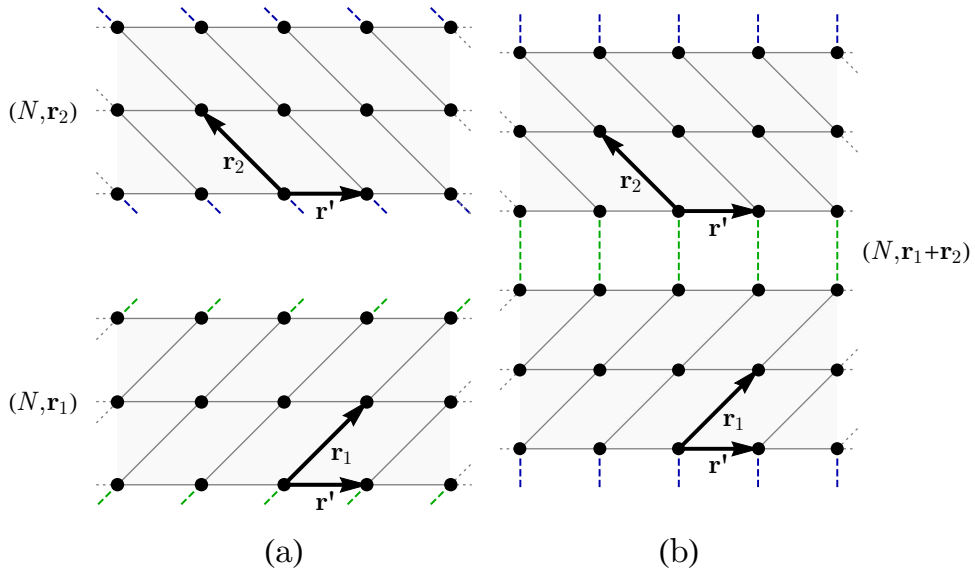

Figure 5.3: The construction of a system from two periodic systems with common extended dimension $\mathbf{r}'$. (a) The lower periodic system has compact dimension along $\mathbf{r}_1$, with sites connected by the dashed green lines identified. Similarly, the upper system has periodic boundary conditions in the $\mathbf{r}_2$ dimension, with sites connected by dashed blue lines identified. (b) By cutting each system along a 1D sublattice in the $\mathbf{r}'$ dimension, and identifying sites between the two systems along the cuts (connected by dashed green/blue lines) we construct a system with periodic dimension along $\mathbf{r}_1 + \mathbf{r}_2$. (Figure adapted from Reference 137 with permission from the *American Physical Society*.)

cutting and rejoining translates a region of dimension λ_{LR} near each cut from L to R by a distance λ_{LR}, but after cutting and rejoining translates the region from R to L by λ_{LR}. The lower bound is obtained by considering the opposite case. These bounds are essentially independent of the system size N, and so δ stays approximately constant as the limit $N \to \infty$ is taken.

By constructing a sequence of systems with increasing N, and calculating $\nu(\mathbf{r})$ using Equations (5.1) and (5.7), we obtain the relations

$$\nu'(\mathbf{r}_1 + \mathbf{r}_2) = \nu(\mathbf{r}_1 + \mathbf{r}_2) = \nu(\mathbf{r}_1) + \nu(\mathbf{r}_2). \tag{5.8}$$

In particular, we see that ν is a linear function of 2D lattice vectors.

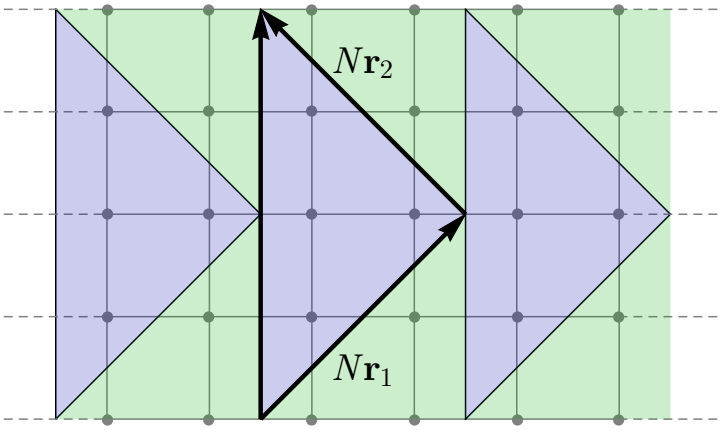

Figure 5.4: Illustration of a 1D cell structure imposed on a 2D system with a compact dimension. For a system with compact dimension of length $N(\mathbf{r}_1 + \mathbf{r}_2)$ we can group the Hilbert spaces of sites within a blue region and pair of green regions into a single site on a 1D chain. The 1D GNVW index, however, is independent of the choice of location of cut used to define L and R in its computation. Therefore, dividing the 2D system using a 'triangular' cut (along $N\mathbf{r}_1$ followed by $N\mathbf{r}_2$) or using a 'linear' cut (along $N(\mathbf{r}_1 + \mathbf{r}_2)$) gives the same index $\mathrm{ind}(U)$. (Figure adapted from Reference 137 with permission from the *American Physical Society*.)

5.2.2 Further details on the classification of 2D effective edge unitaries

In Section 5.2 above, we argued that translationally invariant unitary operators in 2D form equivalence classes labeled by a set of reciprocal lattice vectors $\{\mathbf{G}_p\}$ with p prime. In this section, we show that generic (site-by-site) tensor products of such unitary operators always reduce to this form.

We first note that we can associate a reciprocal lattice vector $\mathbf{G}_n$ with each term of such a tensor product, using the arguments of Section 5.2. We can therefore initially characterize a general product drive by a set of pairs $\{(\mathbf{G}_n, d_n)\}$, where d_n labels the Hilbert space dimension of the nth term (but where the d_n will not generally be prime or unique). To remove any repetition, if any two terms in the product have the same Hilbert space dimension $d_n = d_m$, we may replace the pairs $(\mathbf{G}_n, d_n)$ and $(\mathbf{G}_m, d_m)$ with the single pair $(\mathbf{G}_n + \mathbf{G}_m, d_n = d_m)$.

This is because the information transported is equivalent after the replacement, as may be demonstrated by regrouping the sites on the lattice using the methods of Reference 136.

To reduce all the Hilbert space dimensions to primes, we may view any term for which d_n is not prime as a tensor product of drives, according to its prime factorization. Explicitly, if $d_n = 2^{n_2}3^{n_3}5^{n_5}\ldots$, we can replace $(\mathbf{G}_n, d_n)$ with a term for every prime factor $\{(n_2\mathbf{G}_n, 2), (n_3\mathbf{G}_n, 3), (n_5\mathbf{G}_n, 5), \ldots\}$. Again, the information transported in the 2D boundary system is equivalent in both cases by the regrouping operations of Reference 136.

By performing this reduction to prime dimensions and further combining terms of the same dimension, we find that a general effective edge unitary can always be characterized by a set of reciprocal lattice vectors $\{\mathbf{G}_p\}$, each corresponding to an on-site Hilbert space with prime dimension p. Using Equation (5.2), the scaled chiral flow associated with this effective edge unitary can easily be calculated.

5.2.3 2D boundaries of 3D unitary loops

We are ultimately interested in 3D bulk drives, whose boundaries may be more complicated than the infinite 2D planes considered above. For this reason, we now extend our discussion to 2D systems embedded in 3D. We take some translationally invariant 3D unitary loop drive U_{3D}, defined on a 3D lattice $\Gamma_{\text{3D}} = \mathbb{Z}^3$, which may be used to generate a 2D effective edge unitary at any 2D boundary. If the boundary is a 2D plane, then the surface behavior falls into equivalence classes exactly as described above. To describe the behavior at more general boundary surfaces, however, we consider two 2D Bravais lattices $\mathcal{L}_1$ and $\mathcal{L}_2$, which intersect at a common 1D sublattice with primitive lattice vector $\mathbf{r}$. Each lattice $\mathcal{L}_{1/2}$ is spanned by the basis $\{\mathbf{r}, \mathbf{r}'_{1/2}\}$. We define the complete boundary system to consist of sites belonging to $\mathcal{L}_1$ on one side of the common sublattice, and sites belonging to $\mathcal{L}_2$ on the other. The underlying bulk drive U_{3D} is a translationally invariant unitary loop, and so this procedure defines an effective edge unitary U_{eff} that acts on the quasi-2D boundary system.

Since $\mathbf{r}$ is a vector in both $\mathcal{L}_1$ and $\mathcal{L}_2$, we can still define a periodic system by identifying the Hilbert spaces of sites displaced by $N\mathbf{r}$, as illustrated in Figure 5.5. We can therefore

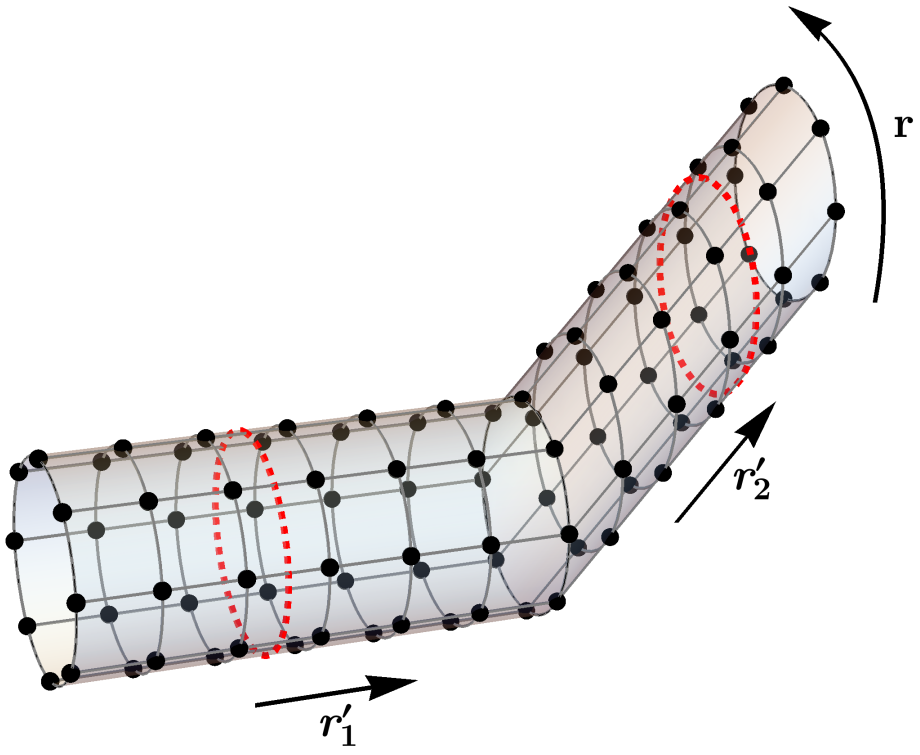

Figure 5.5: Illustration of the interface between two periodic systems with shared compact dimension along $\mathbf{r}$, and extended dimensions along $\mathbf{r}'_1$ and $\mathbf{r}'_2$. The chiral unitary index may be calculated by grouping sites along the $\mathbf{r}$ direction and dividing the resulting 1D system into two halves, L and R. The dashed red lines show two possible cuts for dividing the system. The chiral unitary index is independent of the location of the cut. (Figure adapted from Reference 137 with permission from the *American Physical Society*.)

again compute $\text{ind}(U_{N,\mathbf{r}})$ by dividing the system along $\mathbf{r}$ into two halves, L and R. However, the GNVW index is a local invariant [67], and so the value of $\text{ind}(U_{N,\mathbf{r}})$ is independent of the location of the dividing cut. In particular, far from the interface (where the axial direction is either $\mathbf{r}'_1$ or $\mathbf{r}'_2$), a computation of $\text{ind}(U_{N,\mathbf{r}})$ will yield the same result. By taking the limit $N \to \infty$, we see that the scaled index $\nu(\mathbf{r})$ is consistent across the entire boundary.

The arguments above apply to any pair of 2D planar boundaries which intersect at a line. For a 3D bulk unitary $U_{3\text{D}}$, we can find three pairwise-intersecting planar boundaries in which the interface between each pair is a 1D sublattice spanned by a basis vector of the

original 3D lattice Γ_{3D}. This is illustrated in Figure 5.6. Since the scaled additive index is a locally computed quantity, the values of $\nu(\mathbf{r})$ computed within different 2D planar boundaries must be consistent with each other and with the linearity described in Equation (5.3) (where $\mathbf{r}$ is now promoted to a lattice vector in 3D).

Overall, this means that the effective edge behavior of a translationally invariant 3D loop drive is classified by a set of *three-dimensional* reciprocal lattice vectors $\{\mathbf{G}_p\}$, indexed by primes p. Given the set $\{\mathbf{G}_p\}$, the scaled index $\nu(\mathbf{r})$ is specified for any 2D boundary and any 1D cut within this boundary (defined by the three-dimensional lattice vector $\mathbf{r}$). Due to the discreteness of this classification, effective edge unitaries arising from 3D unitary loop drives may be put into equivalence classes, each labeled by a different set of reciprocal lattice vectors $\{\mathbf{G}_p\}$. In turn, each 3D unitary loop must have an edge behavior belonging to one of these classes, and the space of locally generated 3D loops inherits the classification.

Just as in the 2D case, we can define a representative effective edge unitary $V_{\{\mathbf{G}_p\}}$ on a particular boundary which corresponds to a given set of vectors $\{\mathbf{G}_p\}$. As before, we define a set of translation vectors $\{\mathbf{r}_{\mathrm{tr},p}\}$ corresponding to $\{\mathbf{G}_p\}$ through

$$\mathbf{r}_{\mathrm{tr},p} = \frac{1}{2\pi}\left[(\mathbf{r}_1 \times \mathbf{r}_2) \times \mathbf{G}_p\right] \tag{5.9}$$

but where $\mathbf{r}_1$, $\mathbf{r}_2$ and $\mathbf{G}_p$ are now 3D vectors. The representative unitary $V_{\{\mathbf{G}_p\}}$ acts as a translation with vector $\mathbf{r}_{\mathrm{tr},p}$ on a p-dimensional Hilbert space factor on each site, and may be written as a tensor product of shift operators as

$$V_{\{\mathbf{G}_p\}} = \bigotimes_p \sigma_{\mathbf{r}_{\mathrm{tr},p},p}.$$

Other effective edge unitaries within the same class are related to the representative edge unitary by a locally generated 2D unitary evolution.

For a given equivalence class and boundary surface, the flow of information per unit cell across a cut in the direction of $\mathbf{r}$ is characterized by the index $\nu(\mathbf{r})$. Rewriting Equation (5.2), this can be expressed as

$$\nu(\mathbf{r}) = \frac{1}{2\pi}\sum_p (\mathbf{G}_p \cdot \mathbf{r}) \log p.$$

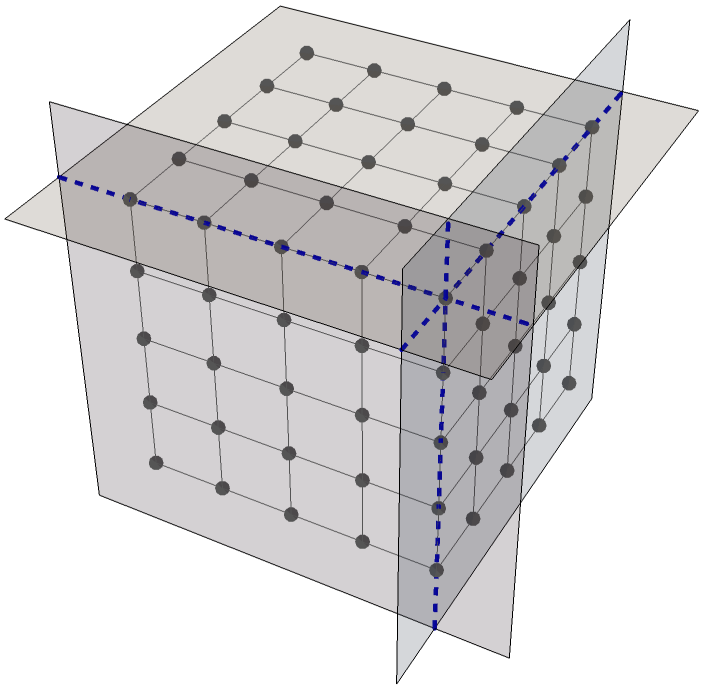

Figure 5.6: Three pairwise-intersecting planar boundaries of a 3D system. The intersection between each pair of planes is spanned by a basis vector of the 3D lattice. Values of the chiral unitary index computed within different boundary planes must be consistent with each other and with linearity. (Figure adapted from Reference 137 with permission from the *American Physical Society*.)

As an example, Figure 5.7 shows the action of a simple effective edge unitary and gives the associated vectors $\mathbf{r}_{\mathrm{tr},p}$ and $\{\mathbf{G}_p\}$, and the index $\nu(\mathbf{r})$ for a choice of cut $\mathbf{r}$.

In the 1D case, each equivalence class of 1D edge behavior has a representative effective edge unitary which is generated by an exactly solvable 2D bulk exchange drive [134, 136]. We demonstrate in the next section that the representative edge unitary of each *two-dimensional* equivalence class may similarly be generated by an exactly solvable 3D bulk exchange drive.

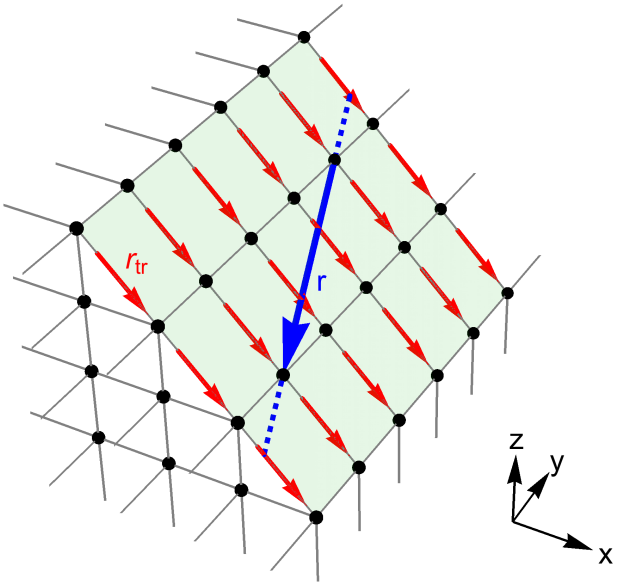

Figure 5.7: The action of a simple effective edge unitary characterized by reciprocal lattice vector $\mathbf{G}_2 = -2\pi\hat{\mathbf{y}}$ (with all other $\mathbf{G}_p$ zero) in a surface with basis $\mathbf{r}_1 = (1, 0, -1)$ and $\mathbf{r}_2 = (0, 1, 0)$ (note: on-site Hilbert space is not shown). Within this surface, the unitary acts as a translation by vector $\mathbf{r}_{\mathrm{tr},2} = (1, 0, -1)$, indicated by red arrows. The blue dashed line indicates a 1D sublattice of this surface, with primitive lattice vector $\mathbf{r} = (1, -3, -1)$ indicated by the blue arrow. The flow of information across this cut per sublattice unit cell is quantified by the index $\nu(\mathbf{r}) = 1/(2\pi)\,(\mathbf{G}_2 \cdot \mathbf{r}) \log 2 = 3 \log 2$. (Figure adapted from Reference 137 with permission from the *American Physical Society*.)

5.3 2D Bulk Exchange Drives

In the previous section, we obtained a classification of local 2D unitary operators with translational invariance, and argued that this provides an equivalent classification of *bulk* Floquet phases in 3D. We showed that each equivalence class is characterized by an infinite set of reciprocal lattice vectors $\{\mathbf{G}_p\}$, and that each class has a representative effective edge unitary $V_{\{\mathbf{G}_p\}}$ that is a product of shift operators (or translations) by vectors given in Equation (5.9). The next aim of this paper is to obtain a set of exactly solvable 3D bulk drives, known as 'exchange drives', which may be used to generate these different representative

edge behaviors. To aid the discussion, we first review exchange drives in two dimensions and show how they can be used to generate all possible 1D boundary behaviors. In Section 5.4, we will naturally extend these ideas to exchange drives in 3D.

5.3.1 Model triangular drive

We first describe a simple four-step unitary loop drive in 2D which can be used as a building block for more general drives. This is a modification of the models introduced in References 134 and 136, which in turn build on the noninteracting drive of Reference 40 (which we reviewed in Section 1.2.2).

The model may be defined on any Bravais lattice with a two-site basis. For simplicity, however, we will assume the lattice is square (i.e. $\Gamma = \mathbb{Z}^2$), has unit lattice spacing, and has both sites within each unit cell (labeled A and B) coincident. Note that this construction is in contrast to References 40, 134, and 136, in which the lattice basis is nonzero. On each site of each sublattice there is a finite, d-dimensional Hilbert space which, for concreteness, we may again assume describes a spin-$(d-1)/2$. In this way, the state at a particular site may be written $|\mathbf{r}, a, \alpha\rangle$, where $\mathbf{r}$ labels the lattice site, $a \in \{A, B\}$ labels the sublattice, and $\alpha \in \mathcal{H}_{\mathbf{r},a}$ labels the state within the on-site Hilbert space. A basis for many-body states is the tensor product of such states.

Following Reference 136, we consider exchange operators of the form

$$U^{\leftrightarrow}_{\mathbf{r},\mathbf{r}'} = \sum_{\alpha,\beta} |\mathbf{r}, A, \beta\rangle \otimes |\mathbf{r}', B, \alpha\rangle \langle \mathbf{r}, A, \alpha| \otimes \langle \mathbf{r}', B, \beta| ,$$

which exchange the state on site $(\mathbf{r}, A)$ with the state on site $(\mathbf{r}', B)$. Note that the operator $U^{\leftrightarrow}_{\mathbf{r},\mathbf{r}'}$ is strictly local for finite $|\mathbf{r} - \mathbf{r}'|$, having no effect on sites other than $\mathbf{r}$ and $\mathbf{r}'$. It can therefore be generated by a similarly local Hamiltonian.

In terms of this operator, we define the four-step drive $U_4 U_3 U_2 U_1$, where each U_n takes the form

$$U_n = \bigotimes_{\mathbf{r}} U^{\leftrightarrow}_{\mathbf{r},\mathbf{r}+\mathbf{b}_n}, \tag{5.10}$$

with $\mathbf{b}_1 = -(\hat{\mathbf{x}} + \hat{\mathbf{y}})$, $\mathbf{b}_2 = -\hat{\mathbf{y}}$, $\mathbf{b}_3 = \mathbf{0}$, and $\mathbf{b}_4 = -\hat{\mathbf{x}}$. Each step of the drive is a product of exchange operations over disjoint pairs of sites separated by $\mathbf{b}_n$, as illustrated in Figure 5.8(a).

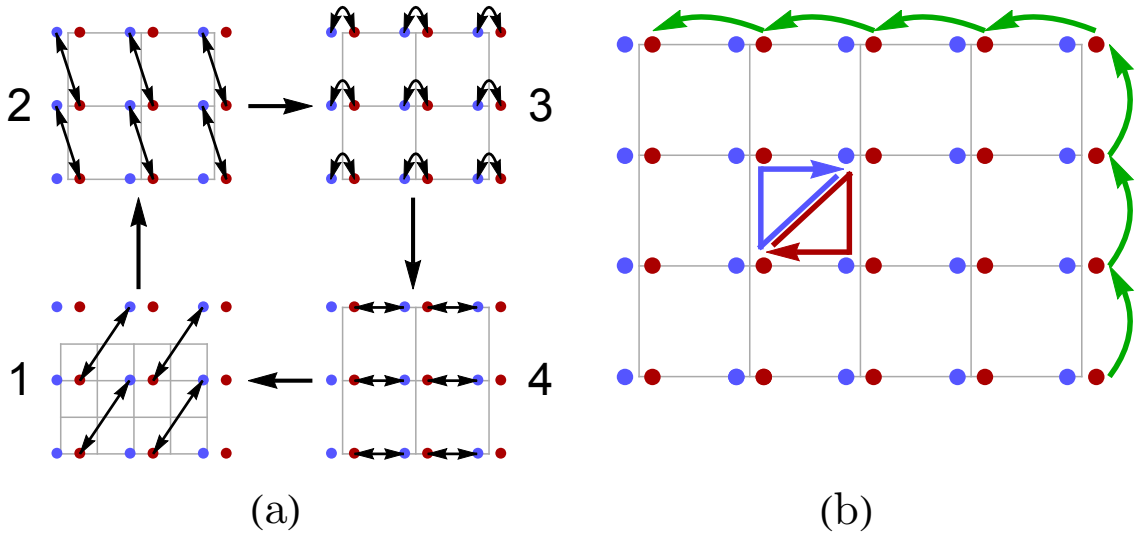

Figure 5.8: Illustration of the four-step exchange drive described in the main text. (a) The steps represent exchanges between nearby on-site states. A-sites are depicted in light blue and B-sites are depicted in dark red. (b) On-site states in the bulk follow a triangular loop path around a half-plaquette. On-site states at the edge are transported by an effective translation operator represented by the green arrows. (Figure adapted from Reference 137 with permission from the *American Physical Society*.)

Since the action of the unitary operator is invariant under lattice translations, we can obtain a complete picture of the drive by focusing on the evolution of a particular on-site component of a generic many-body state. We find that a state beginning at an A-site moves in a clockwise loop around the half-plaquette to its lower-left, while a state beginning at a B-site moves in a clockwise loop around the half-plaquette to its upper-right, as illustrated in Figure 5.8(b). In this way, each on-site state in the bulk returns to its original position. Since this happens simultaneously for every site, the complete unitary operator acts as the identity on a generic many-body state in the bulk, and is therefore a unitary loop.

At the boundary of an open system, however, some exchange operations are forbidden,

and the drive generates anomalous chiral transport [134, 136]. For the system in Figure 5.8(b), the overall action of the drive is a translation of sublattice states counter-clockwise around the 1D edge: In other words, the effective edge unitary of the drive is a shift σ_d. By current conservation, this edge behavior must be the same along any edge cut, even if the cut is not parallel to a lattice vector. Note that it would be impossible to generate such a chiral translation with a local Hamiltonian in a purely 1D quantum system [136], and so this boundary behavior is anomalous. By running this model triangular drive several times, or in the opposite direction, or on more complicated tensor product Hilbert spaces, it is possible to generate boundary shifts $\sigma^p \otimes \sigma^{-q}$ corresponding to every equivalence class introduced in Section 4.3.

5.3.2 Bulk characterization of 2D exchange drives

We now construct more general 2D exchange drives from this primitive triangular drive, and show that they may be used to generate all the different 1D edge behaviors (i.e. combinations of shifts $\sigma_p \otimes \sigma_q^{-1}$) described in Section 4.3. In the process, we show that the geometry of a generic 2D exchange drive in the bulk is directly related to its edge behavior.

Assuming the same lattice structure as in Section 5.3.1, we consider a general drive with $2N$ steps, $U = U_{2N} \dots U_1$, with individual steps of the drive being exchanges in the form of Equation (5.10). We refer to such a drive as an *exchange drive*. Each step is characterized by a Bravais lattice vector $\mathbf{b}_n$, which is the displacement between the exchanged sublattice sites directed from A to B. After n steps, an on-site state beginning at an A-site will be displaced by

$$\mathbf{d}_n = \sum_{m=1}^{n} (-1)^{m+1} \mathbf{b}_m, \tag{5.11}$$

where the minus sign arises because each step of the drive moves a state between sublattices. Similarly, a state beginning at a B-site will be displaced by $-\mathbf{d}_n$.

As motivated in Section 4.1, we are most interested in many-body loop evolutions, which act as the identity in the bulk after a complete driving cycle. The requirement that the drive

be a loop enforces the condition

$$\sum_{n=1}^{2N}(-1)^{n+1}\mathbf{b}_n = 0, \tag{5.12}$$

so that the final displacement vector $\mathbf{d}_{2N}$ is zero. Now, each on-site state follows a closed path during the evolution, and we define the signed area of this path by

$$A_s = \frac{1}{2A_{\text{prim}}}\sum_{n=1}^{2N-2}(-1)^n\left(\mathbf{d}_n \times \mathbf{b}_{n+1}\right)\cdot\hat{\mathbf{z}}, \tag{5.13}$$

where $\hat{\mathbf{z}}$ is a unit vector perpendicular to the system and A_{prim} is the area of a primitive triangle on the lattice ($A_{\text{prim}} = 1/2$ in our convention). Equation (5.13) calculates the net oriented area enclosed by an on-site state beginning at a site in the bulk and following the complete evolution of the drive, in units of the primitive triangle area. In general, an arbitrary drive may generate both positively and negatively oriented components, with counter-clockwise loops corresponding to positive areas (see Figure 5.9). As defined, the signed area A_s is always an integer, which we will find gives a direct measure of the shift behavior at the edge.

We now introduce operations that we will use to deform an exchange drive while preserving its signed area and (possibly anomalous) edge behavior. Proofs of these statements may be found in Appendix 5.A. First, we define a trivial drive to be an exchange drive in which states follow some exchange path and then exactly retrace this path in reverse, satisfying the condition $\mathbf{b}_n = \mathbf{b}_{2N-(n-1)}$. The signed area of a trivial drive is zero by construction.

Next, given an exchange drive, we note that we may continuously insert trivial drives at any point without affecting its signed area or edge properties. That is, given a general drive $U = U_{2N}\ldots U_1$ and a trivial drive T, the drive $U' = U_{2N}\ldots U_n T U_{n-1}\ldots U_1$ is continuously connected to U and has the same signed area. One may also continuously deform an exchange drive by cyclically permuting its steps. These deformations do not affect the signed area of the drive and leave the transport at the edge unaffected, results which are proved in Appendix 5.A. We note that these properties can be demonstrated without appealing to the edge classification previously discussed in Section 5.2.

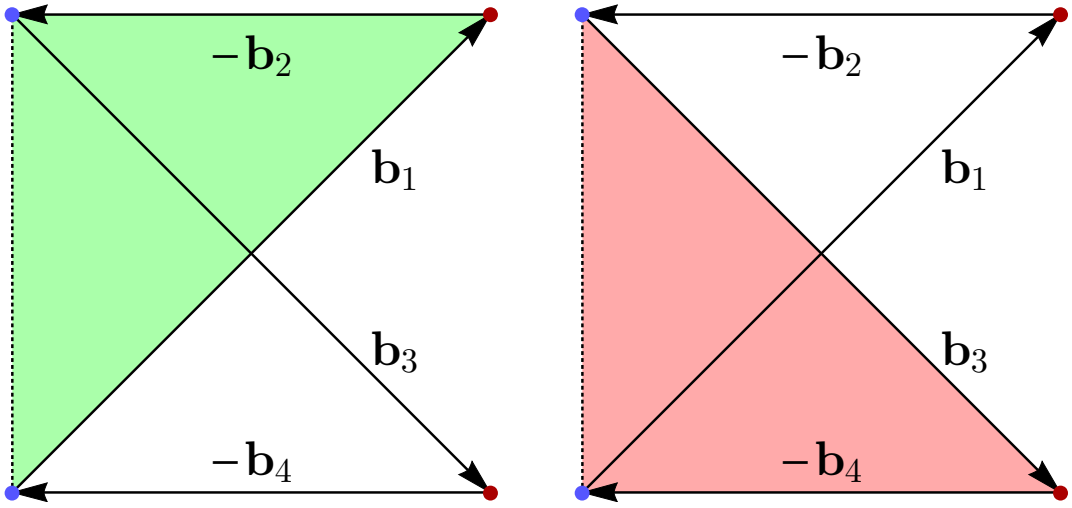

Figure 5.9: Illustration of the signed area summands in Equation (5.13) for a four-step example drive with $\mathbf{b}_1 = \hat{\mathbf{x}} + \hat{\mathbf{y}}$, $\mathbf{b}_2 = \hat{\mathbf{x}}$, $\mathbf{b}_3 = \hat{\mathbf{x}} - \hat{\mathbf{y}}$, $\mathbf{b}_4 = \hat{\mathbf{x}}$. Since $N = 2$ there are $2N - 2 = 2$ terms in the sum. The signed area of the green (red) triangle represents the first (second) term in the sum and is equal to positive (negative) 1, scaled by the primitive triangle area. In total, this four-step exchange drive has $A_s = 0$. (Figure adapted from Reference 137 with permission from the *American Physical Society*.)

Using the tools above, we can decompose a general loop exchange drive into a sequence of four-step triangular loop drives. To do this, we insert a trivial drive between each pair of steps that does not include the first or final step. The nature of the trivial drive inserted will depend on the parity of the step: After odd steps, we insert the trivial drive $U'_{2n+1}U'_{2n+1}$, where U'_{2n+1} is an exchange step with $\mathbf{b}'_{2n+1} = \mathbf{d}_{2n+1}$. After even steps, we insert the trivial drive $U_{\mathrm{OS}}U'_{2n}U'_{2n}U_{\mathrm{OS}}$, where U'_{2n} is an exchange step with $\mathbf{b}'_{2n} = \mathbf{d}_{2n}$ and where U_{OS} is an on-site exchange step with $\mathbf{b} = 0$. The extra swap in the even case acts to effectively transform even steps into odd steps.

After these insertions, the modified drive can be partitioned into a sequence of $(2N - 2)$ four-step loop drives,

$$\begin{aligned} U' &= \ldots U'_4 U_{OS} U_4 U'_3 \cdot U'_3 U_3 U_{OS} U'_2 \cdot U'_2 U_{OS} U_2 U_1, \\ &= \ldots L_3 \cdot L_2 \cdot L_1, \end{aligned} \tag{5.14}$$

a process which is illustrated in Figure 5.10. It is simple to verify that each four-step loop drive in the partition has a minimum of one on-site swap step, and thus forms either a triangular drive or a trivial drive. Since the operations used to modify the drive preserve the signed area, the signed area of the complete drive may be written in terms of its components as

$$A_s(U) = A_s(U') = \sum_n A_s(L_n),$$

where we have written $A_s(U)$ for the signed area of loop drive U, etc. This property is illustrated in Figure 5.10.

5.3.3 Bulk-edge correspondence of 2D exchange drives

Using the loop decomposition of the previous section, the signed area of an arbitrary exchange drive may be related to its chiral transport (of quantum information) at the edge. We define a primitive drive to be a four-step drive in which bulk states follow the path of a primitive triangle, such as the drive described in Section 5.3.1. Since a primitive drive is triangular, one of its steps must be an on-site swap with $\mathbf{b}_n = 0$. However, as cyclic permutations of loops are equivalent (see Appendix 5.A), we may assume without loss of generality that the on-site swap occurs on the third step. Therefore, we may equivalently define a primitive drive as a four-step loop drive in which $\{\mathbf{b}_2, \mathbf{b}_4\}$ form a basis for the Bravais lattice and $\mathbf{b}_3 = 0$.

Now, every primitive drive has an effective edge action equivalent either to the model drive in Section 5.3.1 or to its inverse — in other words, its edge action is a shift σ_d or a shift σ_d^{-1}. To see this, we perform an invertible orientation-preserving and area-preserving transformation which maps the generic primitive drive (characterized by the basis $\{\mathbf{b}_2, \mathbf{b}_4\}$) onto the model primitive drive presented in Section 5.3.1 or its inverse (characterized by the basis $\{-\mathbf{y}, -\mathbf{x}\}$ or $\{-\mathbf{x}, -\mathbf{y}\}$, respectively). The chosen transformation preserves the orientation of sites at the edge, and will map the edge behavior of the generic primitive drive directly onto that of the model primitive drive (or its inverse).

The decomposition of an exchange drive into triangular drives given in Equation (5.14) does not generally reduce the original drive to *primitive* drives (as some of the constituent

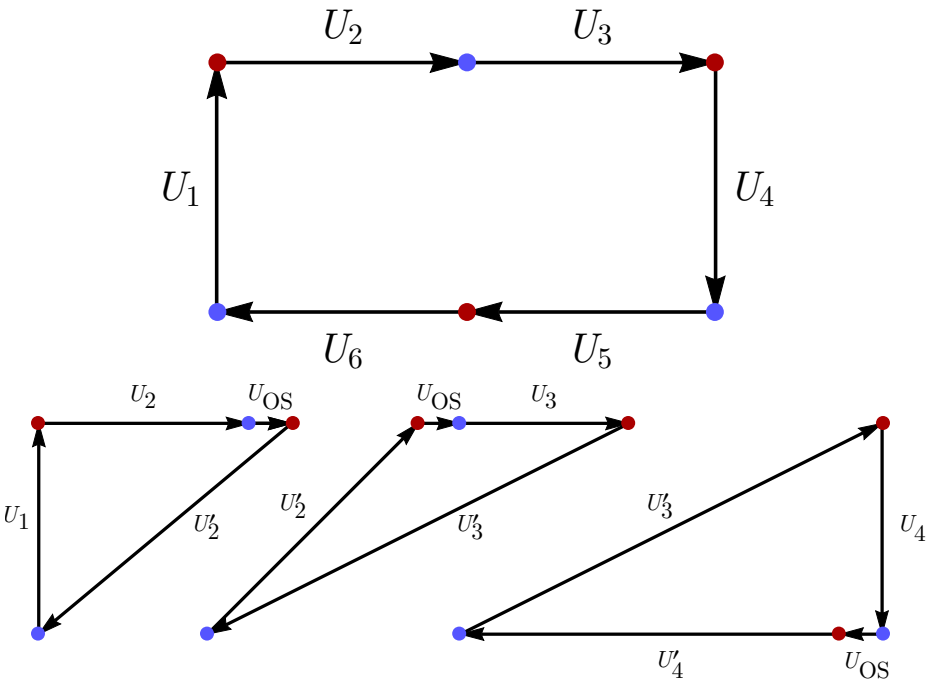

Figure 5.10: Illustration of the triangular decomposition in Equation (5.14) for an example drive, with steps given by U_1 through U_6. Since $N = 3$ there are $2N - 2 = 4$ loops in the decomposition but the fourth loop is a trivial drive and we do not depict it here. For clarity, sublattice sites which are not reached by the state localized in the bottom left have been omitted from the figure. The complete drive has signed area $A_s = 4$ (in units of the primitive triangle), while the loops in the decomposition have areas (from left to right) of $A_s = 1/2$, $A_s = 1/2$ and $A_s = 1$. (Figure adapted from Reference 137 with permission from the *American Physical Society*.)

triangles will have areas larger than A_{prim}). However, we can use what we know about primitive triangles to deduce the effective edge behavior of a general (nonprimitive) triangular drive, $U_{\triangle}$. To see this, note that a drive of this form *is* primitive on some number of *sublattices* of the original lattice. This can be shown by considering the sublattice formed from the span of the vectors $\{\mathbf{b}_2, \mathbf{b}_4\}$ defining $U_{\triangle}$, on which the drive is clearly primitive. Other sublattices on which $U_{\triangle}$ is primitive can be obtained by translating the first sublattice by the basis vectors of the original lattice. This is illustrated in Appendix 5.C, where it is also demonstrated that states on different sublattices do not interact during the drive.

We claim, and prove in Appendix 5.C, that the number of Bravais sublattices N on which a four-step triangular drive is primitive is given by $N = |A_s|$, where A_s is the signed area of that triangular drive. In this way, a four-step triangular drive acts on $|A_s|$ separate sublattices as either the model drive (if $\mathrm{sgn}(A_s) = -1$) or its inverse (if $\mathrm{sgn}(A_s) = 1$). Since the edge behaviors of the model drive and its inverse are shifts of the d-dimensional Hilbert spaces in opposite directions, the overall edge behavior of a general triangular drive is A_s copies of this shift with the appropriate chirality.

Combining the discussions above, we find that the edge behavior of a general 2D translation-invariant exchange drive U is characterized by its signed area in the bulk, $A_s(U)$, and is equivalent to A_s copies of a chiral shift of a d-dimensional on-site Hilbert space. Since the bulk motion of a primitive drive has the opposite chirality to its edge motion, a (negative) positive signed bulk area corresponds to (counter-)clockwise translation at the edge. By forming tensor products of exchange drives, each corresponding to a different on-site Hilbert space, all possible 1D boundary behaviors (with general form $\sigma_p \otimes \sigma_q^{-1}$) can be realized.

5.4 Bulk and edge behavior of 3D exchange drives

5.4.1 Bulk-edge correspondence for 3D exchange drives

We now extend the ideas of the previous section to translation-invariant exchange drives in 3D. As in the 2D case, an exchange drive may be defined on any 3D lattice with a two-site basis $\{A, B\}$. For concreteness, we can assume the lattice is cubic (i.e. $\Gamma_{3\mathrm{D}} = \mathbb{Z}^3$) and has two coincident sublattices. A boundary of such a system may then be obtained by taking a planar slice through Γ to expose some surface containing a 2D Bravais sublattice. More general boundaries can be obtained by taking several intersecting slices. As discussed in Section 5.2, the general edge behavior is described by a set of reciprocal lattice vectors $\{\mathbf{G}_p\}$, while the quantum information flow within a boundary can be characterized by the scaled index $\nu(\mathbf{r})$, defined across a cut in the direction of $\mathbf{r}$.

We consider bulk exchange drives comprising $2N$ steps in the form of Equation (5.10), with

each $\mathbf{b}_n \in \Gamma_{3D}$ now a 3D lattice vector. We recall that these exchange drives are loops, and that they involve local exchange operations that occur throughout the lattice simultaneously (due to translational invariance). Generalizing the signed area of Equation (5.13), we claim that the bulk characterization of a 3D exchange drive is given by the reciprocal lattice vector

$$\mathbf{G} = \frac{2\pi}{V_r} \sum_{n=1}^{2N-1} (-1)^n \left(\mathbf{d}_n \times \mathbf{b}_{n+1}\right), \tag{5.15}$$

where V_r is the volume of the direct lattice unit cell. We will show that this bulk invariant $\mathbf{G}$ is directly related to the set of reciprocal lattice vectors $\{\mathbf{G}_p\}$ (introduced in Section 5.2.3) which characterize the edge behavior.

As in the 2D case, the bulk characterization may be justified by decomposing a general exchange drive into four-step triangular drives. While the decomposition in Equation (5.14) continues to hold, the triangular components are now generally not coplanar. Nevertheless, it follows from the arguments of the previous section that the vector $\mathbf{G}$ for a general drive is the sum of the $\mathbf{G}$ for each triangular drive in its decomposition. The decomposition therefore preserves the value of $\mathbf{G}$, and we can understand the edge behavior of a general exchange drive by focusing on its triangular components.

As in 2D, a triangular drive may be defined by the vectors $\{\mathbf{b}_1, \mathbf{b}_2, \mathbf{b}_3, \mathbf{b}_4\}$, where a cyclic permutation has been chosen so that $\mathbf{b}_3 = \mathbf{0}$. In this setup, the triangular drive lies in a plane we call the 'triangle plane', which includes the vectors $\mathbf{b}_2$ and $\mathbf{b}_4$. We consider the action of this drive on some 2D boundary lattice, spanned by the basis $\{\mathbf{r}_1, \mathbf{r}_2\}$, which defines a 'surface plane'. Neglecting the case where the surface plane and triangle plane are parallel (where the edge behavior is trivial), the intersection of these planes is a 1D Bravais sublattice generated by a primitive vector $\mathbf{a}_1 \in \Gamma_{3D}$. We can therefore choose an ordered basis $\{\mathbf{a}_1, \mathbf{a}_2, \mathbf{a}_3\}$ for Γ_{3D}, where $\{\mathbf{a}_1, \mathbf{a}_2\}$ span the triangle plane (and $\mathbf{a}_3$ is any linearly independent primitive vector). Note that $\mathbf{b}_2$ and $\mathbf{b}_4$ are not necessarily primitive vectors, and in general $(\mathbf{b}_2 \times \mathbf{b}_4) = A_s(\mathbf{a}_1 \times \mathbf{a}_2)$, where A_s is the signed area discussed previously. According to Equation (5.15), this triangular drive will have the characteristic reciprocal lattice vector

$$\mathbf{G} = \frac{2\pi}{V_r}(\mathbf{b}_2 \times \mathbf{b}_4) = \frac{2\pi}{V_r} A_s(\mathbf{a}_1 \times \mathbf{a}_2). \tag{5.16}$$

We now consider the edge behavior of this drive in the surface plane. We can write the ordered basis for the surface plane $\{\mathbf{r}_1, \mathbf{r}_2\}$ in terms of the basis of the 3D lattice as $\mathbf{r_1} = \mathbf{a}_1$ and $\mathbf{r_2} = D\mathbf{a}_2 + E\mathbf{a}_3$ (where $D, E \in \mathbb{Z}$ are coprime). This surface is equivalently characterized by the outward-pointing reciprocal lattice vector

$$\mathbf{k}_s = \frac{2\pi}{V_r}(\mathbf{r}_1 \times \mathbf{r}_2).$$

We claim that the edge behavior of the bulk triangular drive described above is a shift (or translation) within the surface lattice given by the direct lattice vector

$$\mathbf{r}_{\text{tr}} = \frac{2\pi}{V_k}\left(\mathbf{k}_s \times \mathbf{G}\right) = \frac{1}{2\pi}\left[(\mathbf{r}_1 \times \mathbf{r}_2) \times \mathbf{G}\right], \tag{5.17}$$

where V_k is the volume of the 3D reciprocal lattice unit cell. For the triangular drive above this reduces to

$$\mathbf{r}_{\text{tr}} = \frac{1}{V_r}(\mathbf{r}_1 \times \mathbf{r}_2) \times (\mathbf{b}_2 \times \mathbf{b}_4) = -A_s E\mathbf{a}_1.$$

The fact that this is the correct edge behavior can be justified as follows: Since a triangular drive in 3D acts on a stack of parallel decoupled planes, the edge surface will host a 1D shift (or translation) for each triangle plane that terminates on it. The number of triangle planes terminating per unit cell of the 2D boundary sublattice is exactly E, and the factor of A_s accounts for the fact that the triangular drive may not be primitive. The overall minus sign arises because the chirality of the bulk motion is opposite that of the edge motion. Thus, $\mathbf{r}_{\text{tr}}$ gives the effective edge translation correctly for a triangular drive and an arbitrary edge surface.

Since $\mathbf{G}$ for a general exchange drive is given by the sum of $\mathbf{G}$ over its triangular components, it follows that Equation (5.17) holds for *any* 3D exchange drive. In this way, Equations (5.15) and (5.17) completely characterize the bulk and edge behavior of a generic 3D translation-invariant exchange drive.

5.4.2 Tensor Products of 3D exchange drives

In Section 5.2 we found that 2D boundary behaviors form equivalence classes characterized by a set of reciprocal lattice vectors $\{\mathbf{G}_p\}$. The representative edge behavior of given class is a tensor product of shifts $\sigma_{\mathbf{r}_{\mathrm{tr}},p}$ by vectors $\mathbf{r}_{\mathrm{tr},p}$ (defined in Equation (5.9)), each acting on an on-site Hilbert space with prime dimension p. In order to generate the edge behavior of a general equivalence class, we should take a tensor product of the bulk exchange drives described in the previous section.

For the equivalence class with reciprocal lattice vectors $\{\mathbf{G}_p\}$, we take a tensor product Hilbert space which has an on-site factor of dimension p for each non-zero $\mathbf{G}_p$. For each p-dimensional subspace, we choose a bulk exchange drive that is characterized by the reciprocal lattice vector $\mathbf{G} = \mathbf{G}_p$, as defined in Equation (5.15). Any bulk exchange drive with this property is suitable, but for simplicity we can always choose a four-step triangular drive with the appropriate area. Then, by the reasoning above, the complete product drive will produce the required translation by lattice vector $\mathbf{r}_{\mathrm{tr,p}}$ for each p-dimensional subspace on an exposed surface. In other words, a product drive of this form in the bulk will reproduce the representative effective edge unitary of the equivalence class $V_{\{\mathbf{G}_p\}}$ on an exposed boundary. In this way, 3D product drives of this form are representatives of the different equivalence classes of 3D dynamical Floquet phases.

5.4.3 Bulk-edge correspondence for general Floquet drives

Finally, we summarize the interpretation of this bulk-edge correspondence for unitary evolutions in general. An arbitrary Floquet drive will not generally be a unitary loop but, as motivated in Section 4.1, can often be interpreted as a unitary loop composed with an evolution by a constant Hamiltonian. In many cases the unitary loop component can be extracted from a given Floquet drive directly, as discussed in References 55 and 134. Since the unitary loop component captures the inherently *dynamical* part of an evolution, a classification of unitary loops is equivalent to a classification of Floquet topological phases.

In this way, the conclusions above are applicable beyond the somewhat restrictive case of unitary loop evolutions.

However, a unitary loop will not in general be a pure exchange drive. Nevertheless, from the arguments above, an arbitrary unitary loop will have boundary behavior which is topologically equivalent to that of a pure exchange drive. Specifically, the effective edge unitary of an arbitrary loop can be brought into a tensor product of shift operators by a locally generated unitary operator acting only within the boundary region. It is in this sense that a generic unitary loop is equivalent to an exchange drive, and in this manner that unitary loops form equivalence classes labeled by a set of reciprocal lattice vectors $\{\mathbf{G}_p\}$.

In order to determine in practice which equivalence class a given unitary loop belongs to, it is first necessary to obtain its corresponding effective edge unitary U_{eff} for a choice of boundary. This can be achieved by removing terms from the generating Hamiltonian which connect sites across the boundary, as discussed in Section 4.1. Once this has been obtained, the GNVW index across a given cut within the (necessarily finite) 2D boundary region can be computed using Equation (4.2). Note that this requires grouping sites in a direction parallel to the cut to obtain a quasi-1D chain in the manner described in Section 5.2. In order to compute the scaled additive index $\nu(\mathbf{r})$, the GNVW index must be calculated in this manner for a sequence of finite systems as the dimensions are made infinite, and the resulting $\nu(\mathbf{r})$ obtained using Equation (5.1). The value of $\nu(\mathbf{r})$ should tend towards its limiting value very quickly once the dimensions of the system are larger than the Lieb-Robinson length of U_{eff}.

However, the value of $\nu(\mathbf{r})$ for a cut in a boundary surface does not on its own determine the equivalence class of the unitary loop. To obtain the complete set of reciprocal lattice vectors $\{\mathbf{G}_p\}$, we must compute $\nu(\mathbf{r})$ for three linearly independent boundary cut directions $\mathbf{r}$. With these, the values of $\{\mathbf{G}_p\}$ can finally be extracted using equation Equation (5.2.3).

In principle, the procedure described above can be used to determine the equivalence class of any 3D unitary loop. While the process is more involved than calculating the topological invariant of a unitary loop in 2D, both methods ultimately rely on computing the GNVW index for a (quasi)-1D system. In Reference 134, the authors argued that matrix product unitaries

(MPUs) [141] offer a particularly efficient representation of unitary operators at a 1D boundary, which enables the GNVW index to be computed in a numerically efficient manner. Specifically, the GNVW classification implies that any 1D local unitary operator is a combination of a shift operation and a locally generated 1D unitary (or finite-depth quantum circuit). Since both shifts and finite-depth quantum circuits admit efficient MPU representations, it follows that any effective edge unitary also admits an efficient MPU representation. Once expressed as an MPU, the GNVW index can be calculated straightforwardly using the method described in Reference 134.

Since our procedure for calculating the topological invariant of a 2D effective edge unitary relies on computation of the GNVW index, we might hope to be able to apply the advantages of an MPU representation in this case too. Indeed, we believe that the arguments of Reference 134 can be applied directly to this higher dimensional case, with two important caveats. First, the boundary region is now 2D, and calculation of $\nu(\mathbf{r})$ formally requires taking the limit of infinite system size. MPUs are applicable only to 1D systems, and so in order to use them we must 'regroup' lattice sites along one direction to form a quasi-1D chain. However, this regrouping is already part of the procedure for calculating $\nu(\mathbf{r})$, and so MPUs are compatible with this part of the approach (albeit at the expense of using larger matrices to account for the additional sites). Although taking the infinite system-size limit is not feasible with MPUs, we expect the scaling behavior (and limiting value of $\nu(\mathbf{r})$) to become apparent very quickly once the system size is larger than the Lieb-Robinson length of the effective edge unitary. In addition, since $\nu(\mathbf{r})$ takes discrete (rational) values, small finite-size effects can be identified and ignored.

5.5 Discussion

In summary, we have studied 3D many-body Floquet topological phases with translational invariance but no other symmetry from the perspective of their edge behavior. We found that phases of this form fall into equivalence classes that are somewhat analogous to those of weak topological phases. Members of each class share the same anomalous information

transport at a 2D boundary, which is equivalent to a tensor product of shifts (or translations) that arise in lower dimensions. Each equivalence class is described by a set of reciprocal lattice vectors $\{\mathbf{G}_p\}$ corresponding to each prime p, which may be computed directly from the unitary evolution. The representative edge behavior in each equivalence class (corresponding to a tensor product of pure shifts) can be generated by an exactly solvable exchange drive in the bulk.

These equivalence classes capture all possible topological phases (with no symmetry) whose edge behavior is equivalent to that of a tensor product of lower dimensional phases. For this classification to be *complete*, however, there would need to exist no intrinsically 3D ('strong') Floquet topological phases in this class. In the noninteracting case, we know this to be true: Reference 55 demonstrates that noninteracting Floquet systems in class A host only a trivial 3D phase. Given that exchange drives can be interpreted as the many-body extension of noninteracting phases, this property leads us to conjecture that our classification *is* complete. However, further investigation and proof of this conjecture remain important goals for future work, which could perhaps be pursued using a higher-dimensional extension of the methods of Reference 67. However, even without this conjecture holding, our work provides a complete classification of weak Floquet topological phases in 3D.

In classifying these phases, we developed a method for determining the effective edge behavior of an arbitrary exchange drive in 2D or 3D using geometric aspects of its action in the bulk. We found that 3D exchange drives may be characterized by an infinite set of reciprocal lattice vectors $\{\mathbf{G}_p\}$, with p indexing prime Hilbert space dimensions, which may be calculated directly from the form of the bulk exchange drive. These bulk quantities are equal to the topological invariants that classify the edge behavior of the exchange drive, providing a form of bulk-edge correspondence. The vectors $\{\mathbf{G}_p\}$ share some similarities to weak invariants of static topological insulators [31, 32, 142–144]. However, in contrast to the static case, these 3D chiral Floquet phases cannot generally be viewed as stacks of decoupled 2D layers. Instead, different Hilbert space factors within a tensor product may stack in different directions, as illustrated in Figure 5.2.

We briefly discuss how our work fits into the broader classification schemes that have been introduced to study topological phases. Since the phases we describe are weak and require translational invariance, their formal classification derives from that of strong topological phases in one lower dimension. Specifically, our phases are related to tensor products of layers of 2D Floquet topological phases, as has been motivated throughout this work. Such 2D phases are classified by rational numbers p/q [134, 136], and in principle the reciprocal lattice vectors $\{\mathbf{G}_p\}$ of our classification could be expressed as a set of rational numbers p/q corresponding to each spatial dimension—although this description would obscure much of the symmetry of the phase.

More broadly, bosonic Floquet symmetry-protected topological phases have been classified within the group cohomology framework, in one dimension and beyond [50–53, 55]. In brief, many inherently dynamical phases protected by a (unitary) symmetry group G in d dimensions are believed to be classified by the cohomology group $H^d(G, \mathrm{U}(1))$. However, the cohomology approach is known to be unable to capture static chiral phases [145], a property which also seems to extend to the Floquet case [134]. Whether or not chiral phases (such as those in this thesis) can be brought within the cohomology framework remains an interesting outstanding question.

Our classification suggests a number of interesting directions for future work. A natural follow-up is to ask whether a similar classification can be obtained for 3D Floquet phases of fermions, as well as in systems with additional symmetries. In addition, by combining these phases with topological order, it may be possible to obtain analogues of the Floquet enriched topological phases found in References 139 and 140. Finally, it would be useful to obtain a rigorous proof of the conjecture that there are no inherently 3D Floquet topological phases in systems without symmetry, perhaps by developing an extension of the GNVW index to higher dimensions [67].

APPENDIX

5.A Continuous modifications of loop drives

In this appendix we define transformations which may be carried out on a unitary exchange drive, and prove that these transformations leave the effective edge behavior unaltered.

Proposition 1 *Given a 2D unitary loop L which acts trivially in the bulk but nontrivially (i.e. as a shift) at the boundary of an open system and a unitary swap U which interchanges pairs of states separated by a finite distance, we consider the sequence of drives $U^{-1}LU$. We claim that this sequence has the same edge behavior as L.*

Proof: Since U acts as a product over disjoint pairs of sites, we can disentangle its effects in the bulk from its effects on the edge. To do this, we extend the original edge region of L to include sites which are connected to it by the action of U. In this way, we can write the composite unitary as the product of the identity in the bulk and a piece which acts at the edge, as shown in Figure 5.11. Now, considering the action restricted to this new edge region, the unitary acts as a product of local unitaries and a shift (translation) operator. However, no local 1D unitary evolution can generate (or destroy) chiral edge behavior [136], and so the conjugation with U can have no effect on the chiral properties of L.

An alternative point of view is that conjugation with U acts as a local basis transformation of the Hilbert space restricted to the edge. A local basis transformation of a quasi-1D system cannot change the global properties of the drive.

□

Note that U is an exchange operator and can be continuously connected to the identity, and so we can define $U(\theta)$ such that $U(0) = \mathbb{I}$ and $U(1) = U$. We therefore see that conjugation with $U(\theta)$ defines a continuous transformation within the space of unitary loops. Further, note that this composite unitary $U^{-1}LU$ is also a loop as it is trivial in the bulk.

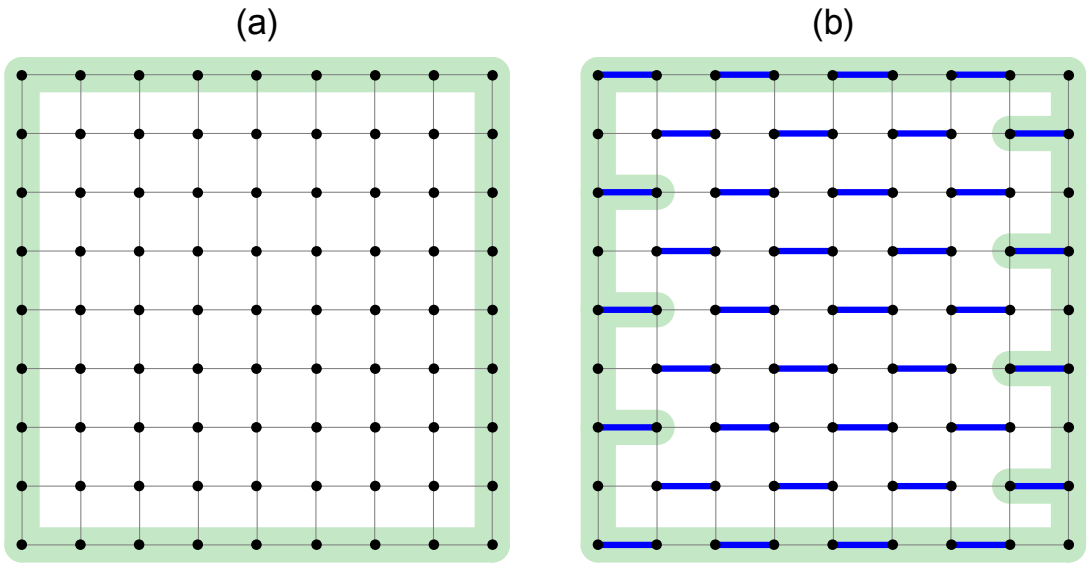

Figure 5.11: (a) A unitary loop L acts trivially in the bulk but may act nontrivially in a quasi-1D edge region located near a boundary (green shaded region). (b) Conjugating the unitary loop L with a product of disjoint pairwise swaps (thick blue lines) may connect bulk sites to the edge region. We define a new quasi-1D edge region which includes these former bulk sites (green shaded region). (Figure adapted from Reference 137 with permission from the *American Physical Society*.)

Proposition 2 *Given a unitary loop L and a finite sequence of local unitary swaps*

$$\{U_1, \ldots, U_N\},$$

the composite unitary operator $(U_1 \ldots U_N)^{-1} L (U_1 \ldots U_N)$ has the same edge behavior as L.

Proof: One repeats the argument in Proposition 1 N times. □

Proposition 3 *Any drive T comprising a sequence of unitary swaps $(U_1 \ldots U_N)$ followed by the inverse swaps in reverse order $(U_N^{-1} \ldots U_1^{-1})$ has trivial effective edge behavior.*

Proof: This follows directly by Proposition 2 if we take L to be $\mathbb{I}$. □

Note that T above is a general 'trivial' drive as defined in Section 5.3. We can therefore

continuously append or remove trivial drives from a sequence of loop drives without affecting the effective edge behavior.

Proposition 4 *Given a unitary loop L which is the product of a sequence of local unitary swaps $L = U_1 \dots U_N$, any cyclic permutation of the steps of L is a loop with the same edge behavior.*

Proof: Consider a cyclic permutation of L, $L' = U_n U_{n+1} \dots U_N U_1 \dots U_{n-1}$. Construct the unitary $V = (U_n U_{n+1} \dots U_N)^{-1}$. Then $V^{-1} L V$ is the cyclic permutation we are considering and by Proposition 2 has the same edge behavior as L. □

5.B Stability of 2D effective edge unitaries

In Reference 136 it is shown that a shift (translation) operator $(\sigma_p)^n$ acting on a 1D boundary cannot be continuously deformed to a different shift operator $(\sigma_p)^{n'}$ with $n \neq n'$ through a locally generated 1D unitary evolution. This includes the trivial shift operator $(\sigma_p)^0 = \mathbb{I}$. In this section we formally show that this stability continues to hold when applied to the more complicated boundary behavior (described by some reciprocal lattice vector $\mathbf{G}_p$) that may act at a 2D boundary.

We consider two 2D boundary systems (which we assume to be identical 2-tori with finite size) with the same on-site Hilbert space dimension p. If these drives have different on-site Hilbert space dimensions or different sizes then they are trivially nonequivalent. On each system, we take unitaries characterized by nonequivalent $\mathbf{G}_p$ and $\mathbf{G}'_p$, leading to distinct behavior. The action of each unitary is characterized by a translation vector within the 2D boundary surface, as argued in Section 5.2.

We now create an effective 1D system by grouping the sites on the 2-torus surface as illustrated in Figure 5.12. If the translation vectors of the two drives are not parallel, we group together the sites on the 2-torus that lie in the direction of the translation vector of (say) the second drive. If the translations of the two drives are parallel, we group together the

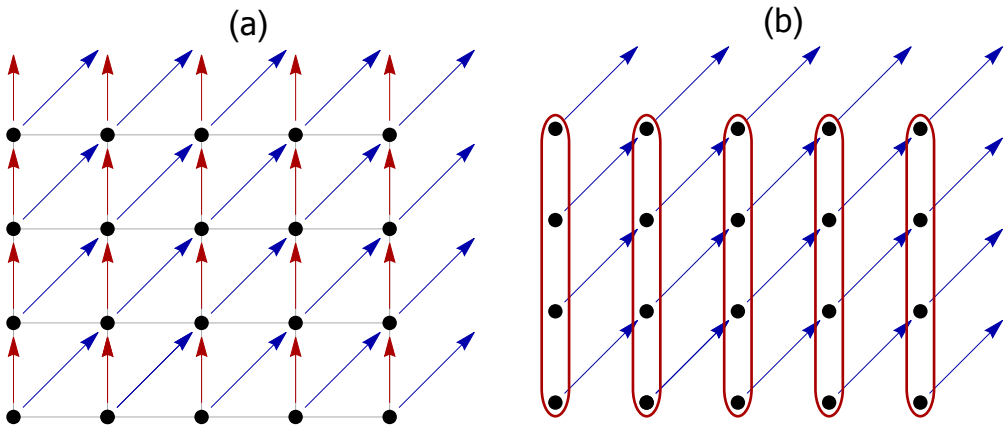

Figure 5.12: Boundary behavior on a 2D surface described by different $\mathbf{G}_p$ and $\mathbf{G}'_p$ cannot be deformed into one another by locally generated unitary evolutions within the boundary. (a) Two different boundary behaviors, corresponding to distinct translation vectors $\mathbf{r}_{\mathrm{tr}}$, are indicated (by red and blue arrows) on a 2D boundary. (b) This 2D behavior can be reduced to an effective 1D model by grouping lattice sites in the direction of one of the $\mathbf{r}_{\mathrm{tr}}$. In this effective model, one effective edge unitary becomes a permutation of the on-site Hilbert space (within the red grouping) and the other becomes a translation in the horizontal direction combined with a permutation (blue arrows). (Figure adapted from Reference 137 with permission from the *American Physical Society*.)

sites of the 2-torus that lie along any chosen direction that is not parallel to the translation vectors. In both cases, we are left with two effective 1D edge behaviors that are topologically distinct [134, 136]. By the arguments of Reference 136, the two effective edge unitaries cannot be deformed into one another by a local 1D perturbation, which implies that the original 2D effective edge unitaries cannot be deformed into one another either. This argument holds for each step in the sequence of boundary systems if their size is made infinite, and extends straightforwardly to drives labeled by a set of reciprocal lattice vectors $\{\mathbf{G}_p\}$.

5.C Nonprimitive triangular drives

In this section, we show that the number of independent sublattices on which a triangular drive is primitive is equal to the magnitude of its signed area (in units of the primitive triangle area). Consider an arbitrary four-step triangular drive defined by vectors $\{\mathbf{b}_1, \mathbf{b}_2, \mathbf{b}_3, \mathbf{b}_4\}$, which we take without loss of generality to have $\mathbf{b}_3 = 0$. If the triangle is not primitive, there are additional Bravais lattice points on the edges or contained within the interior of the triangle, the number of which we denote by e and i respectively.

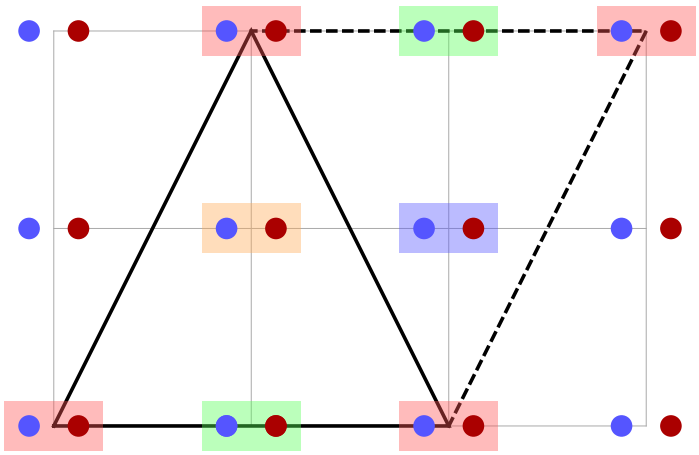

Figure 5.13: A nonprimitive triangular exchange drive is represented by the solid lines, and a parallelogram is formed over a choice of edge. The shading of lattice sites indicates membership of different sublattices spanned by vectors of the parallelogram. The area of the solid triangle is four times the area of a primitive triangle, and there are correspondingly four different sublattices spanned by its component vectors. (Figure adapted from Reference 137 with permission from the *American Physical Society*.)

By specifying an edge of the triangle, we may form a parallelogram (over this edge) as illustrated in Figure 5.13. This parallelogram may be tessellated to tile a sublattice partitioned by the drive. Each interior point of the original triangle results in two interior points of the parallelogram. Each edge point of the original triangle which lies on the edge used to construct the parallelogram results in an interior point of the parallelogram. Edge points on the other edges of the original triangle each result in two edge points of the parallelogram;

however, these points are separated by a sublattice vector. By tiling the lattice with the same parallelogram but shifting the origin to these edge points and interior points, the total number of distinct sublattices spanned by the drive is found to be $1 + e + 2i$.

Pick's theorem states that the area of a lattice polygon, in terms of the unit cell area, is given by

$$A = \frac{v}{2} + \frac{e}{2} + i - 1,$$

where v is the number of vertices [146]. Recalling that the signed area defined in Equation (5.13) is given in terms of the primitive triangle area, we obtain

$$\begin{aligned} |A_s| &= 2A, \\ &= 1 + e + 2i, \end{aligned}$$

for a triangular drive. Hence, the number of independent sublattices is equal to the magnitude of the signed area of the drive. Since each independent sublattice generates its own edge behavior, the edge behavior of a triangular drive is equivalent to a composition of $|A_s|$ primitive drives.

BIBLIOGRAPHY

[1] K. v. Klitzing, G. Dorda, and M. Pepper. New method for high-accuracy determination of the fine-structure constant based on quantized Hall resistance. *Phys. Rev. Lett.*, 45:494–497, August 1980.

[2] Richard Prange and Steven Girvin. *The Quantum Hall Effect*. Springer, 1987.

[3] Daijiro Yoshioka. *The Quantum Hall Effect*. Springer, 1998.

[4] David Tong. Lecture notes on the quantum Hall effect, January 2016.

[5] P.M. Chaikin and T.C. Lubensky. *Principles of condensed matter physics*. Cambridge University Press, 1995.

[6] A. Altland and B. Simons. *Condensed matter field theory*. Cambridge University Press, 2006.

[7] David Tong. Lecture notes on kinetic theory, October 2012.

[8] R. B. Laughlin. Quantized Hall conductivity in two dimensions. *Phys. Rev. B*, 23:5632–5633, May 1981.

[9] B. I. Halperin. Quantized Hall conductance, current-carrying edge states, and the existence of extended states in a two-dimensional disordered potential. *Phys. Rev. B*, 25:2185–2190, February 1982.

[10] Ryota Nakai, Shinsei Ryu, and Kentaro Nomura. Laughlin's argument for the quantized thermal Hall effect. *Phys. Rev. B*, 95:165405, April 2017.

[11] D. J. Thouless, M. Kohmoto, M. P. Nightingale, and M. den Nijs. Quantized Hall conductance in a two-dimensional periodic potential. *Phys. Rev. Lett.*, 49:405–408, August 1982.

[12] J. E. Avron, R. Seiler, and B. Simon. Homotopy and quantization in condensed matter physics. *Phys. Rev. Lett.*, 51:51–53, July 1983.

[13] Barry Simon. Holonomy, the quantum adiabatic theorem, and Berry's phase. *Phys. Rev. Lett.*, 51:2167–2170, December 1983.

[14] Mahito Kohmoto. Topological invariant and the quantization of the Hall conductance. *Annals of Physics*, 160(2):343 – 354, 1985.

[15] Yasuhiro Hatsugai. Chern number and edge states in the integer quantum Hall effect. *Phys. Rev. Lett.*, 71:3697–3700, November 1993.

[16] Douglas R. Hofstadter. Energy levels and wave functions of Bloch electrons in rational and irrational magnetic fields. *Phys. Rev. B*, 14:2239–2249, September 1976.

[17] Fenner Harper. *The Hofstadter model and other fractional Chern insulators.* PhD thesis, University of Oxford, 2015.

[18] F. D. M. Haldane. Model for a quantum Hall effect without Landau levels: Condensed-matter realization of the "parity anomaly". *Phys. Rev. Lett.*, 61:2015–2018, October 1988.

[19] David Carpentier. Topology of Bands in Solids: From Insulators to Dirac Matter. In Bertrand Duplantier, Vincent Rivasseau, and Jean-Nöel Fuchs, editors, *Dirac Matter*, volume 71, pages 95–129. Springer International Publishing, Cham, 2017. Series Title: Progress in Mathematical Physics.

[20] Alexander Altland and Martin R. Zirnbauer. Nonstandard symmetry classes in mesoscopic normal-superconducting hybrid structures. *Phys. Rev. B*, 55:1142–1161, January 1997.

[21] Alexei Kitaev. Periodic table for topological insulators and superconductors. *AIP Conference Proceedings*, 1134(1):22–30, 2009.

[22] Max Karoubi. *K-theory: An introduction.* Springer-Verlag, 1978.

[23] R. Bott and R. Seeley. Some remarks on the paper of Callias. *Communications in Mathematical Physics*, 62(3):235–245, October 1978.

[24] A. Kitaev. Unpaired majorana fermions in quantum wires. *Physics-Uspekhi*, 44(10S):131–136, October 2001.

[25] N. Read and Dmitry Green. Paired states of fermions in two dimensions with breaking of parity and time-reversal symmetries and the fractional quantum Hall effect. *Phys. Rev. B*, 61:10267–10297, April 2000.

[26] Alexei Kitaev. Anyons in an exactly solved model and beyond. *Annals of Physics*, 321(1):2 – 111, January 2006.

[27] C. L. Kane and E. J. Mele. Quantum spin Hall effect in graphene. *Phys. Rev. Lett.*, 95:226801, November 2005.

[28] C. L. Kane and E. J. Mele. Z_2 topological order and the quantum spin Hall effect. *Phys. Rev. Lett.*, 95:146802, September 2005.

[29] B. Andrei Bernevig, Taylor L. Hughes, and Shou-Cheng Zhang. Quantum spin Hall effect and topological phase transition in HgTe quantum wells. *Science*, 314(5806):1757–1761, 2006.

[30] J. E. Moore and L. Balents. Topological invariants of time-reversal-invariant band structures. *Phys. Rev. B*, 75:121306, March 2007.

[31] Rahul Roy. Topological phases and the quantum spin Hall effect in three dimensions. *Phys. Rev. B*, 79:195322, May 2009.

[32] Liang Fu, C. L. Kane, and E. J. Mele. Topological insulators in three dimensions. *Phys. Rev. Lett.*, 98:106803, March 2007.

[33] Vedika Khemani, Achilleas Lazarides, Roderich Moessner, and S. L. Sondhi. Phase structure of driven quantum systems. *Phys. Rev. Lett.*, 116:250401, June 2016.

[34] Dominic V. Else, Bela Bauer, and Chetan Nayak. Prethermal phases of matter protected by time-translation symmetry. *Phys. Rev. X*, 7:011026, March 2017.

[35] C. W. von Keyserlingk and S. L. Sondhi. Phase structure of one-dimensional interacting Floquet systems. II. Symmetry-broken phases. *Phys. Rev. B*, 93:245146, June 2016.

[36] Dominic V. Else, Bela Bauer, and Chetan Nayak. Floquet time crystals. *Phys. Rev. Lett.*, 117:090402, August 2016.

[37] N. Y. Yao, A. C. Potter, I.-D. Potirniche, and A. Vishwanath. Discrete time crystals: Rigidity, criticality, and realizations. *Phys. Rev. Lett.*, 118:030401, January 2017.

[38] Takuya Kitagawa, Erez Berg, Mark Rudner, and Eugene Demler. Topological characterization of periodically driven quantum systems. *Phys. Rev. B*, 82:235114, December 2010.

[39] Liang Jiang, Takuya Kitagawa, Jason Alicea, A. R. Akhmerov, David Pekker, Gil Refael, J. Ignacio Cirac, Eugene Demler, Mikhail D. Lukin, and Peter Zoller. Majorana fermions in equilibrium and in driven cold-atom quantum wires. *Phys. Rev. Lett.*, 106:220402, June 2011.

[40] Mark S. Rudner, Netanel H. Lindner, Erez Berg, and Michael Levin. Anomalous edge states and the bulk-edge correspondence for periodically driven two-dimensional systems. *Phys. Rev. X*, 3:031005, July 2013.

[41] Manisha Thakurathi, Aavishkar A. Patel, Diptiman Sen, and Amit Dutta. Floquet generation of Majorana end modes and topological invariants. *Phys. Rev. B*, 88:155133, October 2013.

[42] J. K. Asbóth, B. Tarasinski, and P. Delplace. Chiral symmetry and bulk-boundary correspondence in periodically driven one-dimensional systems. *Phys. Rev. B*, 90:125143, September 2014.

[43] Frederik Nathan and Mark S Rudner. Topological singularities and the general classification of Floquet–Bloch systems. *New Journal of Physics*, 17(12):125014, December 2015.

[44] Jelena Klinovaja, Peter Stano, and Daniel Loss. Topological Floquet phases in driven coupled nanowires. *Phys. Rev. Lett.*, 116:176401, April 2016.

[45] Paraj Titum, Netanel H. Lindner, Mikael C. Rechtsman, and Gil Refael. Disorder-induced Floquet topological insulators. *Phys. Rev. Lett.*, 114:056801, February 2015.

[46] David Carpentier, Pierre Delplace, Michel Fruchart, and Krzysztof Gawedzki. Topological index for periodically driven time-reversal invariant 2D systems. *Phys. Rev. Lett.*, 114:106806, March 2015.

[47] Michel Fruchart. Complex classes of periodically driven topological lattice systems. *Phys. Rev. B*, 93:115429, March 2016.

[48] Paraj Titum, Erez Berg, Mark S. Rudner, Gil Refael, and Netanel H. Lindner. Anomalous Floquet-Anderson insulator as a nonadiabatic quantized charge pump. *Phys. Rev. X*, 6:021013, May 2016.

[49] Rahul Roy and Fenner Harper. Periodic table for Floquet topological insulators. *Phys. Rev. B*, 96:155118, October 2017.

[50] C. W. von Keyserlingk and S. L. Sondhi. Phase structure of one-dimensional interacting Floquet systems. I. Abelian symmetry-protected topological phases. *Phys. Rev. B*, 93:245145, June 2016.

[51] Dominic V. Else and Chetan Nayak. Classification of topological phases in periodically driven interacting systems. *Phys. Rev. B*, 93:201103, May 2016.

[52] Andrew C. Potter, Takahiro Morimoto, and Ashvin Vishwanath. Classification of interacting topological Floquet phases in one dimension. *Physical Review X*, 6(4):041001, October 2016.

[53] Rahul Roy and Fenner Harper. Abelian Floquet symmetry-protected topological phases in one dimension. *Phys. Rev. B*, 94:125105, September 2016.

[54] Andrew C. Potter and Takahiro Morimoto. Dynamically enriched topological orders in driven two-dimensional systems. *Phys. Rev. B*, 95:155126, April 2017.

[55] Rahul Roy and Fenner Harper. Floquet topological phases with symmetry in all dimensions. *Phys. Rev. B*, 95:195128, May 2017.

[56] Takuya Kitagawa, Matthew A. Broome, Alessandro Fedrizzi, Mark S. Rudner, Erez Berg, Ivan Kassal, Alán Aspuru-Guzik, Eugene Demler, and Andrew G. White. Observation of topologically protected bound states in photonic quantum walks. *Nature Communications*, 3(1):882, January 2012.

[57] Mikael C. Rechtsman, Julia M. Zeuner, Yonatan Plotnik, Yaakov Lumer, Daniel Podolsky, Felix Dreisow, Stefan Nolte, Mordechai Segev, and Alexander Szameit. Photonic Floquet topological insulators. *Nature*, 496(7444):196–200, April 2013.

[58] Gregor Jotzu, Michael Messer, Rémi Desbuquois, Martin Lebrat, Thomas Uehlinger, Daniel Greif, and Tilman Esslinger. Experimental realization of the topological Haldane model with ultracold fermions. *Nature*, 515(7526):237–240, November 2014.

[59] K. Jiménez-García, L. J. LeBlanc, R. A. Williams, M. C. Beeler, C. Qu, M. Gong, C. Zhang, and I. B. Spielman. Tunable spin-orbit coupling via strong driving in ultracold-atom systems. *Phys. Rev. Lett.*, 114:125301, March 2015.

[60] J. Zhang, P. W. Hess, A. Kyprianidis, P. Becker, A. Lee, J. Smith, G. Pagano, I.-D. Potirniche, A. C. Potter, A. Vishwanath, N. Y. Yao, and C. Monroe. Observation of a discrete time crystal. *Nature*, 543(7644):217–220, March 2017.

[61] Fenner Harper, Rahul Roy, Mark S. Rudner, and S.L. Sondhi. Topology and broken symmetry in Floquet systems. *Annual Review of Condensed Matter Physics*, 11(1), 2020.

[62] G. Floquet. On the linear differential equations with periodic coefficients. *Scientific Annals of the Ecole Normale Superieure*, 2e serie, 12:47–88, 1883.

[63] Takashi Oka and Hideo Aoki. Photovoltaic Hall effect in graphene. *Phys. Rev. B*, 79:081406, February 2009.

[64] Netanel H. Lindner, Gil Refael, and Victor Galitski. Floquet topological insulator in semiconductor quantum wells. *Nature Physics*, 7(6):490–495, June 2011.

[65] M. Aidelsburger, M. Atala, M. Lohse, J. T. Barreiro, B. Paredes, and I. Bloch. Realization of the Hofstadter Hamiltonian with ultracold atoms in optical lattices. *Phys. Rev. Lett.*, 111:185301, October 2013.

[66] N. Fläschner, B. S. Rem, M. Tarnowski, D. Vogel, D.-S. Lühmann, K. Sengstock, and C. Weitenberg. Experimental reconstruction of the Berry curvature in a Floquet Bloch band. *Science*, 352(6289):1091–1094, 2016.

[67] D. Gross, V. Nesme, H. Vogts, and R. F. Werner. Index theory of one dimensional quantum walks and cellular automata. *Communications in Mathematical Physics*, 310(2):419–454, March 2012.

[68] Raoul Bott. The stable homotopy of the classical groups. *Annals of Mathematics*, 70(2):313–337, 1959.

[69] Gregory H. Wannier. The structure of electronic excitation levels in insulating crystals. *Phys. Rev.*, 52:191–197, August 1937.

[70] Gregory H. Wannier. Dynamics of band electrons in electric and magnetic fields. *Rev. Mod. Phys.*, 34:645–655, October 1962.

[71] Nicola Marzari, Arash A. Mostofi, Jonathan R. Yates, Ivo Souza, and David Vanderbilt. Maximally localized Wannier functions: Theory and applications. *Rev. Mod. Phys.*, 84:1419–1475, October 2012.

[72] Nicola Marzari and David Vanderbilt. Maximally localized generalized Wannier functions for composite energy bands. *Phys. Rev. B*, 56:12847–12865, November 1997.

[73] Arash A. Mostofi, Jonathan R. Yates, Young-Su Lee, Ivo Souza, David Vanderbilt, and Nicola Marzari. wannier90: A tool for obtaining maximally-localised Wannier functions. *Computer Physics Communications*, 178(9):685 – 699, 2008.

[74] Clyde Edmiston and Klaus Ruedenberg. Localized atomic and molecular orbitals. *Rev. Mod. Phys.*, 35:457–464, July 1963.

[75] W. von Niessen. Density Localization of Atomic and Molecular Orbitals. I. *The Journal of Chemical Physics*, 56(9):4290–4297, May 1972.

[76] János Pipek and Paul G. Mezey. A fast intrinsic localization procedure applicable for ab initio and semiempirical linear combination of atomic orbital wave functions. *The Journal of Chemical Physics*, 90(9):4916–4926, May 1989.

[77] W. Kohn. Analytic properties of Bloch waves and Wannier functions. *Phys. Rev.*, 115:809–821, August 1959.

[78] Jacques Des Cloizeaux. Analytical properties of n-dimensional energy bands and Wannier functions. *Phys. Rev.*, 135:A698–A707, August 1964.

[79] G. Nenciu. Existence of the exponentially localised Wannier functions. *Communications in Mathematical Physics*, 91(1):81–85, March 1983.

[80] Lixin He and David Vanderbilt. Exponential decay properties of Wannier functions and related quantities. *Phys. Rev. Lett.*, 86:5341–5344, June 2001.

[81] Jacques Des Cloizeaux. Energy bands and projection operators in a crystal: Analytic and asymptotic properties. *Phys. Rev.*, 135:A685–A697, August 1964.

[82] D J Thouless. Wannier functions for magnetic sub-bands. *Journal of Physics C: Solid State Physics*, 17(12):L325–L327, April 1984.

[83] I. Dana and J. Zak. Adams representation and localization in a magnetic field. *Phys. Rev. B*, 28:811–820, July 1983.

[84] J. Zak. Identities for Landau Level Orbitals. *Europhysics Letters (EPL)*, 17(5):443–448, February 1992. Publisher: IOP Publishing.

[85] T. Thonhauser and David Vanderbilt. Insulator/Chern-insulator transition in the Haldane model. *Phys. Rev. B*, 74:235111, December 2006.

[86] Domenico Monaco, Gianluca Panati, Adriano Pisante, and Stefan Teufel. Optimal decay of Wannier functions in Chern and quantum Hall insulators. *Communications in Mathematical Physics*, 359(1):61–100, April 2018.

[87] A Malkin and Man' Ko. Coherent states of a charged particle in a magnetic field. *JETP*, 28:527–532, 1969.

[88] V. Bargmann. On a Hilbert space of analytic functions and an associated integral transform part I. *Communications on Pure and Applied Mathematics*, 14(3):187–214, 1961.

[89] I. E. Segal. Mathematical problems of relativistic physics. *ZAMM - Journal of Applied Mathematics and Mechanics / Zeitschrift für Angewandte Mathematik und Mechanik*, 43(12):572–572, 1963.

[90] A. M. Perelomov. On the completeness of a system of coherent states. *Theoretical and Mathematical Physics*, 6(2):156–164, February 1971.

[91] Dragomir M. Davidović and Dušan Arsenović. Coherent states on von Neumann lattice and some of their applications. *Acta Physica Hungarica A) Heavy Ion Physics*, 26(1-2):79–86, November 2006.

[92] E. I. Rashba, L. E. Zhukov, and A. L. Efros. Orthogonal localized wave functions of an electron in a magnetic field. *Physical Review B*, 55(8):5306–5312, February 1997.

[93] Patrick A. Lee and T. V. Ramakrishnan. Disordered electronic systems. *Reviews of Modern Physics*, 57(2):287–337, April 1985.

[94] B Kramer and A MacKinnon. Localization: theory and experiment. *Reports on Progress in Physics*, 56(12):1469–1564, December 1993.

[95] P. W. Anderson. Absence of diffusion in certain random lattices. *Physical Review*, 109(5):1492–1505, March 1958.

[96] D J Thouless. Anderson's theory of localized states. *Journal of Physics C: Solid State Physics*, 3(7):1559–1566, July 1970.

[97] R Abou-Chacra, P W Anderson, and D J Thouless. A selfconsistent theory of localization. *J. Phys. C: Solid State Phys.*, 6:20, 1973.

[98] E. Abrahams, P. W. Anderson, D. C. Licciardello, and T. V. Ramakrishnan. Scaling theory of localization: Absence of quantum diffusion in two dimensions. *Physical Review Letters*, 42(10):673–676, March 1979.

[99] D. E. Khmelnitskii. Quantization of Hall conductivity. *ZhETF Pisma Redaktsiiu*, 38, November 1983.

[100] D.E. Khmelnitskii. Quantum Hall effect and additional oscillations of conductivity in weak magnetic fields. *Physics Letters A*, 106(4):182–183, December 1984.

[101] A. M. M. Pruisken. Universal singularities in the integral quantum Hall effect. *Physical Review Letters*, 61(11):1297–1300, September 1988.

[102] S. L. Sondhi, S. M. Girvin, J. P. Carini, and D. Shahar. Continuous quantum phase transitions. *Reviews of Modern Physics*, 69(1):315–333, January 1997.

[103] H. P. Wei, D. C. Tsui, M. A. Paalanen, and A. M. M. Pruisken. Experiments on delocalization and university in the integral quantum Hall effect. *Phys. Rev. Lett.*, 61:1294–1296, Sep 1988.

[104] G. V. Mil'nikov and I. M. Sokolov. Semiclassical localization in a magnetic field. *Journal of Experimental and Theoretical Physics Letters*, 48:536, November 1988.

[105] J T Chalker and P D Coddington. Percolation, quantum tunnelling and the integer Hall effect. *Journal of Physics C: Solid State Physics*, 21(14):2665–2679, May 1988.

[106] B. Huckestein, B. Kramer, and L. Schweitzer. Characterization of the electronic states near the centres of the Landau bands under quantum Hall conditions. *Surface Science*, 263(1):125–128, February 1992.

[107] Y. Huo and R. N. Bhatt. Current carrying states in the lowest Landau level. *Physical Review Letters*, 68(9):1375–1378, March 1992.

[108] M. M. Fogler, A. Yu. Dobin, and B. I. Shklovskii. Localization length at the resistivity minima of the quantum Hall effect. *Phys. Rev. B*, 57:4614–4627, Feb 1998.

[109] Keith Slevin and Tomi Ohtsuki. Critical exponent for the quantum Hall transition. *Physical Review B*, 80(4):041304, July 2009.

[110] Wanli Li, C. L. Vicente, J. S. Xia, W. Pan, D. C. Tsui, L. N. Pfeiffer, and K. W. West. Scaling in plateau-to-plateau transition: A direct connection of quantum Hall systems with the Anderson localization model. *Physical Review Letters*, 102(21):216801, May 2009.

[111] Qiong Zhu, Peng Wu, R. N. Bhatt, and Xin Wan. Localization-length exponent in two models of quantum Hall plateau transitions. *Physical Review B*, 99(2):024205, January 2019.

[112] Michael E. Fisher and Michael N. Barber. Scaling theory for finite-size effects in the critical region. *Physical Review Letters*, 28(23):1516–1519, June 1972.

[113] V Privman. *Finite Size Scaling and Numerical Simulation of Statistical Systems*. World Scientific, January 1990.

[114] M. E. J. Newman and G. T. Barkema. *Monte Carlo methods in statistical physics*. Clarendon Press, February 1999.

[115] Somendra M Bhattacharjee and Flavio Seno. A measure of data collapse for scaling. *Journal of Physics A: Mathematical and General*, 34(33):6375–6380, August 2001.

[116] J. A. Nelder and R. Mead. A simplex method for function minimization. *The Computer Journal*, 7(4):308–313, January 1965.

[117] Naoki Kawashima and Nobuyasu Ito. Critical behavior of the three-dimensional J model in a magnetic field. *Journal of the Physical Society of Japan*, 62(2):435–438, February 1993.

[118] Jérôme Houdayer and Alexander K. Hartmann. Low-temperature behavior of two-dimensional gaussian ising spin glasses. *Phys. Rev. B*, 70:014418, Jul 2004.

[119] Sandro Wenzel, Elmar Bittner, Wolfhard Janke, and Adriaan M.J. Schakel. Percolation of vortices in the 3D Abelian lattice Higgs model. *Nuclear Physics B*, 793(1-2):344–361, April 2008.

[120] Per-Olov Löwdin. On the nonorthogonality problem. In *Advances in Quantum Chemistry*, volume 5, pages 185–199. Elsevier, 1970.

[121] B. C. Carlson and Joseph M. Keller. Orthogonalization procedures and the localization of Wannier functions. *Phys. Rev.*, 105:102–103, January 1957.

[122] I. Mayer. On Löwdin's method of symmetric orthogonalization. *International Journal of Quantum Chemistry*, 90(1):63–65, 2002.

[123] Achilleas Lazarides, Arnab Das, and Roderich Moessner. Equilibrium states of generic quantum systems subject to periodic driving. *Phys. Rev. E*, 90:012110, July 2014.

[124] Luca D'Alessio and Marcos Rigol. Long-time behavior of isolated periodically driven interacting lattice systems. *Phys. Rev. X*, 4:041048, December 2014.

[125] Pedro Ponte, Anushya Chandran, Z. Papić, and Dmitry A. Abanin. Periodically driven ergodic and many-body localized quantum systems. *Annals of Physics*, 353:196 – 204, 2015.

[126] Pedro Ponte, Z. Papić, Fran çois Huveneers, and Dmitry A. Abanin. Many-body localization in periodically driven systems. *Phys. Rev. Lett.*, 114:140401, April 2015.

[127] Achilleas Lazarides, Arnab Das, and Roderich Moessner. Fate of many-body localization under periodic driving. *Phys. Rev. Lett.*, 115:030402, July 2015.

[128] Dmitry A. Abanin, Wojciech De Roeck, and François Huveneers. Theory of many-body localization in periodically driven systems. *Annals of Physics*, 372:1 – 11, 2016.

[129] Liangsheng Zhang, Vedika Khemani, and David A. Huse. A Floquet model for the many-body localization transition. *Phys. Rev. B*, 94:224202, December 2016.

[130] Rahul Nandkishore and David A. Huse. Many-body localization and thermalization in quantum statistical mechanics. *Annual Review of Condensed Matter Physics*, 6(1):15–38, 2015.

[131] Dmitry A. Abanin, Wojciech De Roeck, and Fran çois Huveneers. Exponentially slow heating in periodically driven many-body systems. *Phys. Rev. Lett.*, 115:256803, December 2015.

[132] Tomotaka Kuwahara, Takashi Mori, and Keiji Saito. Floquet–Magnus theory and generic transient dynamics in periodically driven many-body quantum systems. *Annals of Physics*, 367:96 – 124, 2016.

[133] Dmitry Abanin, Wojciech De Roeck, Wen Wei Ho, and François Huveneers. A rigorous theory of many-body prethermalization for periodically driven and closed quantum systems. *Communications in Mathematical Physics*, 354(3):809–827, September 2017.

[134] Hoi Chun Po, Lukasz Fidkowski, Takahiro Morimoto, Andrew C. Potter, and Ashvin Vishwanath. Chiral Floquet phases of many-body localized bosons. *Phys. Rev. X*, 6:041070, December 2016.

[135] Elliott H. Lieb and Derek W. Robinson. The finite group velocity of quantum spin systems. *Communications in Mathematical Physics*, 28(3):251–257, September 1972.

[136] Fenner Harper and Rahul Roy. Floquet topological order in interacting systems of bosons and fermions. *Phys. Rev. Lett.*, 118:115301, March 2017.

[137] Dominic Reiss, Fenner Harper, and Rahul Roy. Interacting Floquet topological phases in three dimensions. *Phys. Rev. B*, 98:045127, July 2018.

[138] Blake R. Duschatko, Philipp T. Dumitrescu, and Andrew C. Potter. Tracking the quantized information transfer at the edge of a chiral Floquet phase. *Phys. Rev. B*, 98:054309, August 2018.

[139] Hoi Chun Po, Lukasz Fidkowski, Ashvin Vishwanath, and Andrew C. Potter. Radical chiral Floquet phases in a periodically driven Kitaev model and beyond. *Physical Review B*, 96(24), December 2017.

[140] Lukasz Fidkowski, Hoi Chun Po, Andrew C. Potter, and Ashvin Vishwanath. Interacting invariants for Floquet phases of fermions in two dimensions. *Phys. Rev. B*, 99:085115, February 2019.

[141] J Ignacio Cirac, David Perez-Garcia, Norbert Schuch, and Frank Verstraete. Matrix product unitaries: structure, symmetries, and topological invariants. *Journal of Statistical Mechanics: Theory and Experiment*, 2017(8):083105, August 2017.

[142] Bertrand I. Halperin. Possible states for a three-dimensional electron gas in a strong magnetic field. *Japanese Journal of Applied Physics*, 26(S3-3):1913, January 1987.

[143] Liang Fu and C. L. Kane. Topological insulators with inversion symmetry. *Phys. Rev. B*, 76:045302, July 2007.

[144] Rahul Roy. Characterization of three-dimensional topological insulators by two-dimensional invariants. *New Journal of Physics*, 12(6):065009, June 2010.

[145] Xie Chen, Zheng-Cheng Gu, Zheng-Xin Liu, and Xiao-Gang Wen. Symmetry protected topological orders and the group cohomology of their symmetry group. *Phys. Rev. B*, 87:155114, April 2013.

[146] G. Pick. Geometrisches zur Zahlenlehre. Sonderabdr. Naturw.-medizin. Verein f. Böhmen “Lotos” Nr. 8, 9 S. 8°, 1899.